

Electronic Thesis and Dissertation Repository

12-6-2012 12:00 AM

Wind field measurements around photovoltaic panel arrays mounted on large flat-roofs

R Nicolas Pratt, *The University of Western Ontario*

Supervisor: Dr. Gregory Kopp, *The University of Western Ontario*

A thesis submitted in partial fulfillment of the requirements for the Master of Engineering Science degree in Civil and Environmental Engineering

© R Nicolas Pratt 2012

Follow this and additional works at: <https://ir.lib.uwo.ca/etd>



Part of the [Civil Engineering Commons](#)

Recommended Citation

Pratt, R Nicolas, "Wind field measurements around photovoltaic panel arrays mounted on large flat-roofs" (2012). *Electronic Thesis and Dissertation Repository*. 986.
<https://ir.lib.uwo.ca/etd/986>

This Dissertation/Thesis is brought to you for free and open access by Scholarship@Western. It has been accepted for inclusion in Electronic Thesis and Dissertation Repository by an authorized administrator of Scholarship@Western. For more information, please contact wlsadmin@uwo.ca.

WIND FIELD MEASUREMENTS AROUND PHOTOVOLTAIC PANEL
ARRAYS MOUNTED ON LARGE FLAT-ROOFS

(Spine title: Wind field around PV arrays mounted on large flat-roofs)

(Thesis format: Monograph)

by

Robert Nicolas Pratt

Graduate Program in Civil and Environmental Engineering

A thesis submitted in partial fulfillment
of the requirements for the degree of
Masters of Engineering Science

The School of Graduate and Postdoctoral Studies

The University of Western Ontario

London, Ontario, Canada

© Robert Nicolas Pratt 2012

THE UNIVERSITY OF WESTERN ONTARIO
School of Graduate and Postdoctoral Studies

CERTIFICATE OF EXAMINATION

Examiners:

Supervisor:

.....
Dr. G. Bitsuamlak

.....
Dr. Gregory Kopp

.....
Dr. T. Newson

.....
Dr. C. Zhang

The thesis by

Robert Nicolas Pratt

entitled:

Wind field measurements around photovoltaic panel arrays mounted on large flat-roofs

is accepted in partial fulfillment of the
requirements for the degree of
Masters of Engineering Science

.....
Date

.....
Chair of the Thesis Examination Board

Abstract

An investigation of the wind field around roof-mounted PV arrays has been undertaken, utilizing synchronized TR-PIV and pressure measurements, in order to better understand the mechanisms which result in the aerodynamic loads, most importantly uplift, which act on such arrays. The mean flow is not significantly altered above the array as compared to a bare roof, while Reynolds normal and shear stresses are markedly reduced. Increasing the tilt angle of the array results in a progression from uplifts driven by vortex induced suction, which cause peak uplifts on a bare roof, towards uplifts which are driven primarily by local flow around the panels. For small tilt angle arrays this local flow is associated with large-scale building generated vortices, while for larger tilt angle arrays the instantaneous reattachment of the separated shear layer establishes the local flow.

Keywords: Wind loads; solar arrays; low-rise buildings; building aerodynamics; turbulent flows; PIV

Acknowledgments

First and foremost I would like to thank my supervisor, Dr. Gregory Kopp. It has been a pleasure to work with Greg over the past two years and I have appreciated his thoughtful input to my research. In addition to Greg's invaluable support, he allowed me the latitude to take my research in those directions which I found both fitting and interesting. I also wanted to thank Greg for giving me the opportunity to travel to Shanghai to present my work at the 7th International Colloquium on Bluff Body Aerodynamics & Applications.

I would also like to thank my fellow students at the wind tunnel lab: Zach Taylor (now Dr. Taylor) and Adam Kirchhefer who were invaluable resources for all matters PIV, and Mohammad Abrar Alam Khan, Chowdhury Mohammad Jubayer, and Jeong Hee Oh for the many interesting discussions over the past two years. I am also grateful for the support of the technicians at the wind tunnel, in particular Gerry Dafoe. Adrian Costache provided valuable assistance resolving issues regarding to the synchronization of the pressure and PIV measurements.

I must give a special thank you to my better half, Morgan Rose, whose patience and love keeps me grounded. Finally, I would like to thank my mother and father, Bernadette Pratt and Gerhard Pratt, for their continual support no matter where my interests take me.

Contents

| | |
|---|-------------|
| Certificate of Examination | ii |
| Abstract | iii |
| Acknowledgments | iv |
| List of Figures | viii |
| List of Tables | xv |
| List of Appendices | xvi |
| 1 Introduction | 1 |
| 1.1 Literature review | 3 |
| 1.1.1 Surface mounted prisms | 3 |
| 1.1.2 Separating-reattaching flows | 4 |
| 1.1.3 Prior work on roof mounted PV arrays | 7 |
| 1.1.4 Prior work on roof mounted PV arrays conducted at the UWO | 9 |
| 2 Experimental setup | 12 |
| 2.1 Introduction | 12 |
| 2.2 Wind Tunnel Facility | 13 |
| 2.3 Model Details | 13 |
| 2.4 Terrain Simulation | 14 |
| 2.5 Measurement System | 16 |

| | | |
|----------|--|-----------|
| 2.5.1 | Surface Pressure Measurements | 16 |
| 2.5.2 | Particle Image Velocimetry Measurements | 20 |
| 2.5.3 | Pressure and Velocity Data Synchronization | 23 |
| 2.6 | Pressure area averaging | 23 |
| 3 | General flow field descriptions | 24 |
| 3.1 | Low-rise building | 24 |
| 3.1.1 | Flow field over the roof | 24 |
| 3.1.1.1 | Mean velocity | 24 |
| 3.1.1.2 | Reynolds stresses | 25 |
| 3.1.2 | Roof pressure field | 29 |
| 3.1.2.1 | Mean pressure field | 29 |
| 3.1.2.2 | Fluctuating pressure field | 32 |
| 3.2 | PV Array | 33 |
| 3.2.1 | PV Arrays: Flow field | 33 |
| 3.2.1.1 | Mean velocity | 33 |
| 3.2.1.2 | Reynolds stresses | 34 |
| 3.2.2 | PV Arrays: Pressure field | 39 |
| 3.2.2.1 | Mean pressure field | 39 |
| 3.2.2.2 | Fluctuating pressure field | 40 |
| 4 | Peak uplift events | 47 |
| 4.1 | Peak pressures along the centreline | 47 |
| 4.2 | Peak uplift flow field analysis | 49 |
| 4.2.1 | Roof of low-rise building | 52 |
| 4.2.2 | 2° Tilt angle array: South wind | 53 |
| 4.2.3 | 2° Tilt angle array: North wind | 57 |
| 4.2.4 | 20° Tilt angle array: South wind | 60 |

| | | |
|----------|--|-----------|
| 4.2.5 | 20° Tilt angle array: North wind | 62 |
| 4.3 | Discussion on the peak uplift mechanisms | 65 |
| 5 | Conclusions | 71 |
| 5.1 | Future Work | 74 |
| | Bibliography | 75 |
| A | Comparison of pressure results with published data | 79 |
| B | Combination pressure plots | 84 |
| C | Fraction of local maximum velocity contour plots for peak ensemble averaged velocity fields | 87 |
| | Curriculum Vitae | 97 |

List of Figures

| | | |
|-----|---|----|
| 1.1 | Schematic representation of the flow around a surface-mounted cube. Reproduced from Martinuzzi and Tropea [6]. | 5 |
| 1.2 | Schematic representation of the corner or 'delta wing' vortex. Reproduced from Banks <i>et al.</i> [8]. | 5 |
| 1.3 | Critical wind directions for the worst area-averaged uplifts on PV arrays for various tributary areas, 0° is due north. Reproduced from Kopp <i>et al.</i> [16]. . . . | 11 |
| 2.1 | Coordinate system definition: (a) section view through centre of building; (b) plan view of the building. | 15 |
| 2.2 | Mean streamwise velocity and turbulence intensity profiles. Symbols: □, Iu; ■, V_h/V_{10m} . Data points are experimental measurements, while solid lines are the ESDU profiles for $z_0 = 0.03m$. Reproduced from Kopp <i>et al.</i> [16]. | 17 |
| 2.3 | Spectra of velocity fluctuations. Experimental data are solid lines while dashed lines are the ESDU target spectra for $z_0 = 0.03m$. Reproduced from Kopp <i>et al.</i> [16]. | 18 |
| 2.4 | Location of the pressure taps on the PV array and the roof of the building: upper surface taps are indicated with by the symbol, ○, while lower surface taps are indicated with the symbol, +. Taps on the roof surface are indicated with the symbol, *. | 20 |
| 2.5 | Photograph of experimental setup showing positioning of the two fields of view and the laser sheet. | 22 |

| | | |
|------|--|----|
| 3.1 | Mean streamwise velocity profiles for a north/south wind. Streamlines are shown as dashed lines for reference. | 25 |
| 3.2 | Mean vertical velocity profiles for a north/south wind. Streamlines are shown as dashed lines for reference. | 26 |
| 3.3 | Streamwise Reynolds normal stress, $\overline{u'u'}$, profiles for a north/south wind. Streamlines are shown by the dashed lines for reference. | 27 |
| 3.4 | Vertical Reynolds normal stress, $\overline{w'w'}$, profiles for a north/south wind. Streamlines are shown by the dashed lines for reference. | 27 |
| 3.5 | Reynolds shear stress, $\overline{-u'w'}$, profiles for a north/south wind. Streamlines are shown by the dashed lines for reference. | 28 |
| 3.6 | Maximum Reynolds stresses. Symbols: \circ , $\overline{u'u'}$ (present results); \square , $\overline{w'w'}$ (present results); \triangle , $\overline{-u'w'}$ (present results); \bullet , Castro and Haque $\overline{u'u'}$; \blacksquare , Castro and Haque $\overline{w'w'}$ [30]. | 30 |
| 3.7 | Bare roof mean pressure coefficients for a north/south wind. Symbols: \circ , $y/H = 0.078$; \times , $y/H = -0.078$ | 31 |
| 3.8 | Bare roof $\overline{C_p^*}$ distribution for north/south wind (\circ). Normal/splitter plate results from Roshko and Lau [32] are shown for reference (\square). | 32 |
| 3.9 | Bare roof RMS pressure coefficients for a north/south wind. Symbols: \circ , $y/H = 0.078$; \times , $y/H = -0.078$ | 33 |
| 3.10 | Streamlines of the mean velocity for 2° panel tilt angle. | 35 |
| 3.11 | Streamlines of the mean velocity for 20° panel tilt angle. | 36 |
| 3.12 | Mean velocity profiles. Symbols: $+$, bare roof; \square , 2° north; \circ , 2° south; ∇ , 20° north; \triangle , 20° south. | 37 |
| 3.13 | Reynolds normal and shear stress profiles. Symbols: $+$, bare roof; \square , 2° north; \circ , 2° south; ∇ , 20° north; \triangle , 20° south. | 38 |
| 3.14 | Mean pressure coefficients, 2° panel tilt angle. Symbols: \circ , Net $\overline{C_p}$; \square , Upper surface $\overline{C_p}$; \times , Lower surface $\overline{C_p}$ | 41 |

| | | |
|------|---|----|
| 3.15 | Mean pressure coefficients, 20° panel tilt angle. Symbols: ○, Net $\overline{C_p}$; □, Upper surface $\overline{C_p}$; ×, Lower surface $\overline{C_p}$ | 42 |
| 3.16 | RMS pressure coefficients, 2° panel tilt angle. Symbols: ○, Net $\widetilde{C_p}$; □, Upper surface $\widetilde{C_p}$; ×, Lower surface $\widetilde{C_p}$ | 45 |
| 3.17 | RMS pressure coefficients, 20° panel tilt angle. Symbols: ○, Net $\widetilde{C_p}$; □, Upper surface $\widetilde{C_p}$; ×, Lower surface $\widetilde{C_p}$ | 46 |
| 4.1 | Centreline peak uplift net pressure coefficients. Symbols: +, bare roof; □, 2° north; ○, 2° south; ▽, 20° north; △, 20° south. | 50 |
| 4.2 | Centreline peak factors. Symbols: +, bare roof; □, 2° north; ○, 2° south; ▽, 20° north; △, 20° south. | 51 |
| 4.3 | Schematic illustrating identification of peak uplift events and construction of peak ensemble averages. Upper figure is net pressure coefficient time history, lower figure is peak ensemble velocity field. | 52 |
| 4.4 | Ensemble averaged streamlines for peak uplifts on imaginary panels on the roof of the low-rise building for north/south winds. | 54 |
| 4.5 | Ensemble averaged pressure distributions for peak uplifts on imaginary panels on the roof of the low-rise building for north/south winds. Symbols: □, Point $C_{p,ensm}$; ○, panel net $C_{p,ensm}$; ×, mean point $\overline{C_p}$ | 55 |
| 4.6 | Ensemble averaged streamlines for peak uplifts on panels on 2° tilt angle array under a south wind. | 56 |
| 4.7 | Ensemble averaged fluctuating velocity field for peak uplifts on panels on 2° tilt angle array under a south wind. | 57 |
| 4.8 | Ensemble averaged pressure distributions for peak uplifts on 2° tilt angle array under a south wind. Symbols: ○, Net $C_{p,ensm}$; □, upper surface $C_{p,ensm}$; ×, lower surface $C_{p,ensm}$ | 58 |
| 4.9 | Ensemble averaged streamlines for peak uplifts on panels on 2° tilt angle array under a north wind. | 59 |

| | |
|--|----|
| 4.10 Ensemble averaged fluctuating velocity field for peak uplifts on panels on 2° tilt angle array under a north wind. | 60 |
| 4.11 Ensemble averaged pressure distributions for peak uplifts on 2° tilt angle array under a north wind. Symbols: ○, Net $C_{p,ensm}$; □, upper surface $C_{p,ensm}$; ×, lower surface $C_{p,ensm}$ | 61 |
| 4.12 Ensemble averaged streamlines for peak uplifts on panels on 20° tilt angle array under a south wind. | 63 |
| 4.13 Ensemble averaged fluctuating velocity field for peak uplifts on panels on 20° tilt angle array under a south wind. | 63 |
| 4.14 Ensemble averaged pressure distributions for peak uplifts on 20° tilt angle array under a south wind. Symbols: ○, Net $C_{p,ensm}$; □, upper surface $C_{p,ensm}$; ×, lower surface $C_{p,ensm}$ | 64 |
| 4.15 Ensemble averaged streamlines for peak uplifts on panels on 20° tilt angle array under a north wind. | 66 |
| 4.16 Ensemble averaged fluctuating velocity field for peak uplifts on panels on 20° tilt angle array under a north wind. | 66 |
| 4.17 Ensemble averaged pressure distributions for peak uplifts on 20° tilt angle array under a north wind. Symbols: ○, Net $C_{p,ensm}$; □, upper surface $C_{p,ensm}$; ×, lower surface $C_{p,ensm}$ | 67 |
| 4.18 Peak uplift mechanisms for panels within the separation bubble. The peak panels are highlighted in red. Solid lines indicate flows observed flow features; dashed lines indicated hypothesized flow features. | 69 |
| A.1 Roof centreline mean pressure coefficients for a north/south wind. Symbols: ○, present results; □, 1:12 roof slope, 12.12m (full-scale) building, from Ho <i>et al.</i> [24]. | 80 |

| | | |
|-----|---|----|
| A.2 | Roof centreline RMS pressure coefficients for a north/south wind. Symbols: \circ , present results; \square , 1:12 roof slope, 12.12m (full-scale) building, from Ho <i>et al.</i> [24]. | 80 |
| A.3 | Mean centreline pressure coefficients on the upper surfaces of the panels with a 2° tilt angle for a south wind. Symbols: \circ , present results; \square , Kopp <i>et al.</i> [16]. | 81 |
| A.4 | RMS centreline pressure coefficients on the upper surfaces of the panels with a 2° tilt angle for a south wind. Symbols: \circ , present results; \square , Kopp <i>et al.</i> [16]. . | 81 |
| A.5 | Mean centreline pressure coefficients on the upper surfaces of the panels with a 20° tilt angle for a north wind. Symbols: \circ , present results; \square , Kopp <i>et al.</i> [16]. | 82 |
| A.6 | RMS centreline pressure coefficients on the upper surfaces of the panels with a 20° tilt angle for a north wind. Symbols: \circ , present results; \square , Kopp <i>et al.</i> [16]. | 82 |
| A.7 | Mean centreline pressure coefficients on the upper surfaces of the panels with a 20° tilt angle for a south wind. Symbols: \circ , present results; \square , Kopp <i>et al.</i> [16]. | 83 |
| A.8 | RMS centreline pressure coefficients on the upper surfaces of the panels with a 20° tilt angle for a south wind. Symbols: \circ , present results; \square , Kopp <i>et al.</i> [16]. | 83 |
| B.1 | Combination plot of mean net pressure coefficients. Symbols: $+$, bare roof; \square , 2° north; \circ , 2° south; ∇ , 20° north; \triangle , 20° south. | 85 |
| B.2 | Combination plot of mean point pressure coefficients. Note for PV array data are upper surface point pressures only. Symbols: $+$, bare roof; \square , 2° north; \circ , 2° south; ∇ , 20° north; \triangle , 20° south. | 85 |
| B.3 | Combination plot of RMS net pressure coefficients. Symbols: $+$, bare roof; \square , 2° north; \circ , 2° south; ∇ , 20° north; \triangle , 20° south. | 86 |
| B.4 | Combination plot of RMS point pressure coefficients. Note for PV array data are upper surface point pressures only. Symbols: $+$, bare roof; \square , 2° north; \circ , 2° south; ∇ , 20° north; \triangle , 20° south. | 86 |

| | | |
|-----|--|----|
| C.1 | Fraction of local maximum streamwise velocity contour plots of peak ensemble averaged velocity fields for uplifts on imaginary panels on bare roof under a north/south wind. | 88 |
| C.2 | Fraction of local maximum vertical velocity contour plots of peak ensemble averaged velocity fields for uplifts on imaginary panels on bare roof under a north/south wind. | 88 |
| C.3 | Fraction of local maximum streamwise velocity contour plots of peak ensemble averaged velocity fields for uplifts on panels of 2° tilt angle array under a south wind. | 89 |
| C.4 | Fraction of local maximum vertical velocity contour plots of peak ensemble averaged velocity fields for uplifts on panels of 2° tilt angle array under a south wind. | 90 |
| C.5 | Fraction of local maximum streamwise velocity contour plots of peak ensemble averaged velocity fields for uplifts on panels of 2° tilt angle array under a north wind. | 91 |
| C.6 | Fraction of local maximum vertical velocity contour plots of peak ensemble averaged velocity fields for uplifts on panels of 2° tilt angle array under a north wind. | 92 |
| C.7 | Fraction of local maximum streamwise velocity contour plots of peak ensemble averaged velocity fields for uplifts on panels of 20° tilt angle array under a south wind. | 93 |
| C.8 | Fraction of local maximum vertical velocity contour plots of peak ensemble averaged velocity fields for uplifts on panels of 20° tilt angle array under a south wind. | 94 |
| C.9 | Fraction of local maximum streamwise velocity contour plots of peak ensemble averaged velocity fields for uplifts on panels of 20° tilt angle array under a north wind. | 95 |

C.10 Fraction of local maximum vertical velocity contour plots of peak ensemble averaged velocity fields for uplifts on panels of 20° tilt angle array under a north wind. 96

List of Tables

| | |
|---|----|
| 2.1 Geometrical details of the buildings and arrays (in equivalent full-scale dimensions) | 16 |
|---|----|

List of Appendices

| | |
|--|----|
| Appendix A Comparison of pressure results with published data | 79 |
| Appendix B Combination pressure plots | 84 |
| Appendix C Fraction of local maximum velocity contour plots for peak ensemble averaged velocity fields | 87 |

Chapter 1

Introduction

An investigation of the wind field around roof-mounted photovoltaic (PV) arrays has been undertaken, with the goal of understanding the mechanisms which result in the aerodynamic loads, most importantly uplift, which act on such arrays. An aerodynamic study of PV arrays is particularly relevant given the recent increase in installed solar PV capacity both internationally and within Canada itself. The Earth Policy Institute reports a 2480% increase in the total global installed Solar PV capacity between 1999-2009, with 35.5% of this capacity being added in 2009 alone [1]. Within the same time period Canada has seen a 1522% increase in total capacity, with fully 65.4% of the total installed capacity being added in 2009 [2]. In Canada programs, such as the Province of Ontario's FIT (Feed-in Tariff) program, which provides attractive 20 year guaranteed pricing for renewable electricity production, have also further incentivized increases in PV capacity [3]. Despite this rapid increase in installed capacity there are currently no building standards in North America which explicitly cover the wind loading experienced by PV arrays on rooftops [4, 5]. The practice of installing PV arrays on roof tops has become common in both new construction and retrofit projects, particularly in urban and suburban areas where access to undeveloped land is limited and expensive. Rooftops offer the additional benefit of having less shading from surrounding natural and built environments.

Roof mounted PV panels are generally mounted in a light framing system and secured

on flat roofs through two methods: mechanical fastening directly to the building structure or ballasting of the framing system. In retrofit type projects penetrating the roofing system is often undesirable, and ballasting is generally used to secure PV arrays. Since large flat roofs generally do not have the capacity for much additional loading, an understanding of the aerodynamics of loads on PV arrays is important to ensure systems are able to withstand wind loads without being over designed. A thorough understanding of the aerodynamics mechanisms that result in the peak wind loads on PV arrays also opens the opportunity to determine methods to minimize loads whether it be through optimal positioning of panels or through the use of designed features.

As will be shown in Sections 1.1.3 and 1.1.4, the published work available in the literature on the subject has been primarily focused on determining the aerodynamic loads on roof mounted PV arrays. There has been far less discussion on the aerodynamic mechanisms which are responsible for these loads, particularly the mechanisms which are driving the peak loads. Of primary interest are the aerodynamics associated with the peak uplift events which could result in panels being lifted off the roof surface. The flow field which develops over roof mounted PV arrays is complex. The flow field is influenced by the flow separations at the building's edges, resulting in large scale building generated vortices. The panels themselves induce local separations and reattachments along the array. The structure of the incident boundary layer is also important, and the mean flow turbulence of the boundary layer must be accurately simulated in any wind tunnel testing. Finally, all these structures and features of the flow will of course interact with one another.

It is the aim of the present study to begin to describe and understand the aerodynamics of roof mounted PV arrays, particularly the aerodynamic mechanisms which result in peak loads. To achieve these objectives, we have conducted a series of wind tunnel studies using synchronized time-resolved particle image velocimetry (TR-PIV) and pressure measurements. PIV allows us to investigate the flow field in much greater detail than has been possible in the past with pressure measurements alone. Furthermore, utilizing synchronized PIV and pressure

measurements allows us to identify the peak events in the pressure field and then study the flow fields associated with these peaks.

1.1 Literature review

1.1.1 Surface mounted prisms

The aim of this section is to introduce the general aerodynamic features of the flow around a low rise building, known more generally in fundamental fluid dynamics research as the flow around a surface mounted prism in a turbulent boundary layer. Martinuzzi and Tropea [6] provide a good schematic representation, reproduced in Figure 1.1, of the flow around a surface-mounted cube showing the complex series of vortices which form around the cube when the cube's leading face is perpendicular to the mean flow direction. On the front face of the cube, a recirculation region forms at the base of the cube. This recirculation region is part of the larger horseshoe vortex which wraps around the the entire cube and continues to develop downstream of the cube. Recirculation regions, characterized by reversed flow near the surface, are also formed near the leading edges of both the sides and top of the cube; these regions are bounded by separating/reattaching shear layers. Some of the largest suction on the upper surface (i.e. a low-rise building's roof) occur within separation bubble formed at the leading edge, when the leading face is perpendicular to the mean flow [7]. Two vortices form behind the cube and though they appear isolated when viewed from a plane parallel and close to the surface/ground, these two vortices extend upwards to form an arch. The flow which separates for the trailing edges of the cube also reattaches to the floor.

If the cube is rotated relative to the mean flow direction, the flow is further complicated. The main flow feature which occurs over the roof for an oblique wind is the formation of the corner, or so called 'delta wing' vortex, shown in Figure 1.2. The largest mean and peak suction are observed to occur beneath this corner vortex structure [8].

It is important to note that the vortex structures described above are a result of not only

the prism's geometry but also of the structure of the boundary layer flow to which the prism is subjected; for example, Castro and Robins showed that if a surface mounted cube is subjected to a uniform flow, rather than a turbulent boundary layer, the flow which separates from the leading edge of the cube never reattaches to the top and sides resulting in drastically different pressure distributions [7]. Castro and Robins found that the depth of the boundary layer strongly influenced the pressure distribution over their cube; they found that for $\delta/H \approx 0.7-0.9$ (where δ is the boundary layer depth, and H is the height of the cube) the pressure distribution drastically changes from one that resembles the uniform flow case, to one which more closely follows the turbulent boundary layer case described above. As δ/H is further increased the peak roof suction moves closer to the leading edge and the minimum suction near the trailing edge decreases.

It is well known that the large negative peak pressures on a low rise building's roof occur underneath the separating-reattaching shear layer, or within the so-called separation bubble. An early hypothesis suggested that these peaks were related to changes in the size of the separation bubble, characterized by the varying position of reattachment of the separated shear layer on the roof's surface. It was hypothesized that as the reattachment position moved closer to the leading edge the curvature of the shear layer would increase, thus, the velocity around the leading edge would increase hence reducing the pressure within the bubble [9]. However, as will be discussed more fully in Section 1.1.2, investigations of simple two-dimensional separating-reattaching flows show that pressure fluctuations within the separation bubble are associated with the vortices [10].

1.1.2 Separating-reattaching flows

As we have shown in section 1.1.1 the separating-reattaching flow formed at the leading edge of a building's roof is one of the major flow features of interest due to its influence on the flow field, and hence the pressure field, close to a roof's surface. In addition to discussing the flow around surface mounted prisms, it is also informative to examine the flow over various

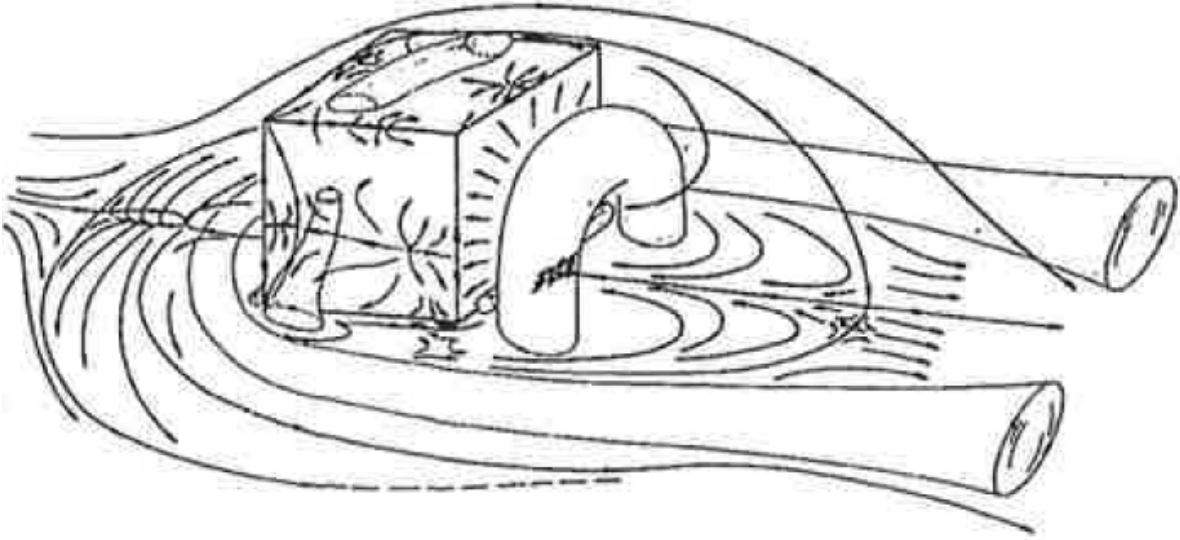


Figure 1.1: Schematic representation of the flow around a surface-mounted cube. Reproduced from Martinuzzi and Tropea [6].

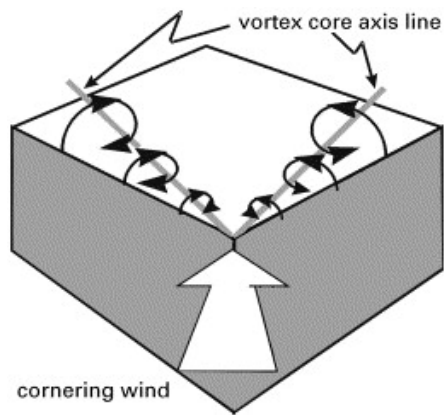


Figure 1.2: Schematic representation of the corner or 'delta wing' vortex. Reproduced from Banks *et al.* [8].

two-dimensional obstacles, such as blunt flat plates or normal plates with rear mounted splitter plates. The leading edge flow in for these two-dimensional obstacles is also characterized by a similar separating-reattaching shear layer. These types of geometries allow us to study simplified separated-reattaching flows.

The comprehensive study of the separation bubble formed on a blunt flat plate by Cherry, Hillier and Latour [11] concluded that three main processes dominate the shear-layer, and hence, the surface pressure fluctuations:

1. A low frequency flapping motion which is dominant near separation, associated with the growth and decay of the separation bubble;
2. A pseudo-periodic shedding of small-scale structures from the separation bubble;
3. An irregular shedding of large-scale vortices.

Work conducted by Saathoff and Melbourne [10] on a blunt flat plate in smooth and turbulent streams provides a summary of the influence of both turbulent intensity and scale on the mean, fluctuating, and peak pressure distributions in the separation bubble . It was found that increased turbulence intensity has the following effects:

1. Reduces the mean reattachment length and reduces the minimum value of the mean pressure;
2. Shifts position of maximum pressure fluctuations upstream within the bubble;
3. Shifts position of the maximum peak suction upstream within the bubble.

Increasing the integral scale of turbulence has the following effects:

1. It has no pronounced influence on the mean pressure distributions;
2. It increases the maximum value of pressure fluctuations;
3. It increases the maximum value of the peak suction.

Another study by Saathoff and Melbourne [12] provides an interesting commentary into the mechanisms that result in peak suctions for the flow over a blunt flat plate in a turbulent flow: Large peak suctions are associated with the growth, convection (from the leading edge downstream), and eventual shedding of a strong vortex within the separation bubble. This phenomenon is believed to be initiated by a perturbation in the free stream flow. Saathoff and Melbourne also observed that a reduction in turbulence scale results in a decrease in the magnitude of the peak suctions. This is due to the fact that with smaller scale turbulence the vortices associated with the peak events are shed before they can fully mature, as the shear layer is subject to a relatively higher frequency perturbations than in larger scale turbulence. In effect, the period of vorticity entrainment during vortex growth is longer in larger scale turbulence leading to stronger vortices. Interestingly, the mechanisms causing the peak suctions in both smooth and turbulent flows are believed to be the same. It is not clear whether these same effects hold when the body is surface-mounted.

Experiments conducted on a two-dimensional square prism in a turbulent flow showed that the probability distribution of the pressures at a point within the separation bubble was strongly negatively skewed. This is in contrast to approximately normal distribution observed within the separation bubble for a normal flat plate [10].

1.1.3 Prior work on roof mounted PV arrays

As mentioned in the introduction, the primary focus of the majority of the published works on the subject of roof mounted PV array wind interaction was on investigations of the aerodynamic loads on these arrays. Questions investigated by these studies have included:

- What are the peak loads experienced by roof mounted arrays?
- Where on the building do peak loads occur?
- Do factors such as roof offsets, panel spacings and distance from the roof influence loads?
- Do roof mounted arrays affect the wind loads on the roof surface?

Some early work was conducted by Radu *et al.* [13] investigating the wind loads on an array of PV panels placed on the roof of a five-story building. Although both sides of the panels were instrumented with pressure taps, only mean pressures were recorded. Shielding effects due to the building and the preceding rows of panels were reported.

The work of Wood *et al.* [14] examined PV arrays mounted on flat-roofed buildings through a wind tunnel pressure study. The panels of the array were mounted parallel to a roof at several panel heights and spacings. It was found that these two factors had minimal effect on measured panel topside, underside and roof pressures. A 1:100 scaled model with full scale dimensions of 12 x 41 x 27 meters (H x W x L) was used. Wood *et al.* reported that peak uplifts on the panels were significantly lower than those experienced by the roof itself without panels installed. While it was not explicitly mentioned, this conclusion certainly suggests that pressure equalization may be playing a role in neutralizing these loads. Indeed, Bienkiewicz and Endo [15] found that for PV arrays with low tilt angles pressure equalization does have a significant effect on the aerodynamic loads experienced by these systems. In multi-layer systems pressure equalization is a mechanism through which internal and exterior surface pressures can be balanced, such that the net load across the surface is reduced. This occurs due to pressure transmission via openings between the two surfaces [16]. Wood *et al.* focused more on total roof loads rather than panel uplift finding that the panels did not significantly alter net roof loads. The aerodynamic mechanisms responsible for the observed loads were not discussed. It is important to note that PV panels will often be mounted at an angle, rather than parallel to a roof, in order to operate at higher efficiencies (when installed far from the equator).

Geurts and van Bentum [17] also presented results from wind tunnel testing of PV arrays mounted on a flat roof. This study utilized a 1:50 scale model with full scale dimensions of 10x30x40 (HxWxL) meters. The arrays in this study were mounted at a 35° tilt angle and both an open and closed support structure were used. The effect of parapets were also investigated. Rows of panels were positioned at specific points of interest (corner and edge zones) rather than having the array cover the entire roof. The largest uplifts on the panels were found to

occur in the corner zone of the roof. Additionally it was found that panels surrounded by other similar panels would experience a reduced wind load due to shielding effects. Again, as with the work of Wood *et al.*, no comment was made on the aerodynamic mechanisms. The results of this study have been incorporated into the Dutch pre-standard NVN 7250 [18].

Wind loads on flat roof-mounted PV arrays as determined using computational fluid dynamics (CFD) methods were compared with wind tunnel results by Bronkhorst *et al.* [19]. The study focused solely on a comparison of mean pressure coefficients and no attempt was made to predict peak loads using CFD. Bronkhorst *et al.* compared several turbulence models including Renormalization Group (RNG) $k-\epsilon$ models and a differential Reynolds Stress model. As will be shown later, peak events are relatively rare and occur at high peak factors and as such would represent a significant challenge to model using CFD methods and extrapolating mean values to peak values would also not be reasonable. While Bronkhorst *et al.* concluded that the general mean pressure distributions compared well to the wind tunnel results, differences between the CFD and wind tunnel results were still on the order of 35%. This indicates that work is still required to adequately predict mean pressures, let alone peak loads, using RNG $k-\epsilon$ models.

1.1.4 Prior work on roof mounted PV arrays conducted at the UWO

The primary basis for the present work is an extensive series of wind tunnel pressure studies conducted out at the University of Western Ontario's (UWO) Boundary Layer Wind Tunnel Laboratory (BLWTL) carried out by Kopp *et al.* [16]. This multi-parameter study aimed to investigate wind loads on PV arrays mounted on large flat roofs and determine the effect of panel tilt angle, inter-panel spacing and roof offset on these loads. Furthermore, the results were compared to the wind loads for similar arrays mounted on the ground in order to determine the effect of the building on the loads. The wind tunnel models were constructed at a scale of 1:30. The PV arrays consisted of 12 rows of panels, each of the rows being made up of 12 PV modules each. The rows were mounted parallel to the northern/southern edges of the building.

Two panel tilt angles were considered: 2° and 20° . All tests were conducted in a simulated open country terrain, as characterized by a roughness length, $z_0 = 0.03m$. Both the upper and lower surface of the panels, as well as the surface of the building's roof, were instrumented with pressure taps.

Kopp *et al.* [16] found that three critical wind directions (those which resulted in the largest panel uplifts) existed for roof mounted systems: Northern (0°), northern-cornering (30° - 60°) winds and southern winds (180°) (bearing in mind that for PV arrays installed in the northern-hemisphere will face south to achieve the highest solar efficiency). The critical wind directions as a function of various tributary areas over which the wind loads were averaged are summarized in Figure 1.3. It was suggested that these loads were the result of a complex interplay between the large-scale building generated vortices, local flow around the panels, and pressure equalization between the upper and lower surface of the panels. From Figure 1.3 we can begin to see how the building affects the aerodynamics. For ground mounted systems the wind direction resulting in peak uplifts is primarily northern; northern-cornering winds are also critical for areas along the eastern edges of the array¹. For a roof mounted system southern winds are also critical for panel areas within the separation bubble that is formed at the leading edge of the building, in addition to northern and northern-cornering winds. For northern cornering winds, the peak loads appear to be due to interaction of the corner vortex with the array. Simply speaking, the spiraling vortical flow impinges the underside of the panels. The peak loads for this wind direction typically occur in the NE corner of the roof. The peak uplifts for southern winds most often occur on the first two southern rows. These rows were located within the separation bubble that forms when the flow separates from the southern edge of the roof. The flow in the separation bubble at the height of the array travels opposite to the freestream velocity, resulting in uplift on the panels. Peak events were characterized by peak factors approaching values of 10, indicating the rarity of these events.

¹Note that symmetry has been used in Kopp *et al.*'s experiments thus the results only refer to wind angles from 0° (north) thru 90° (east) to 180° (south). As such when we refer to the eastern edge, by symmetry this could also refer to the western edge depending upon the cornering wind direction.

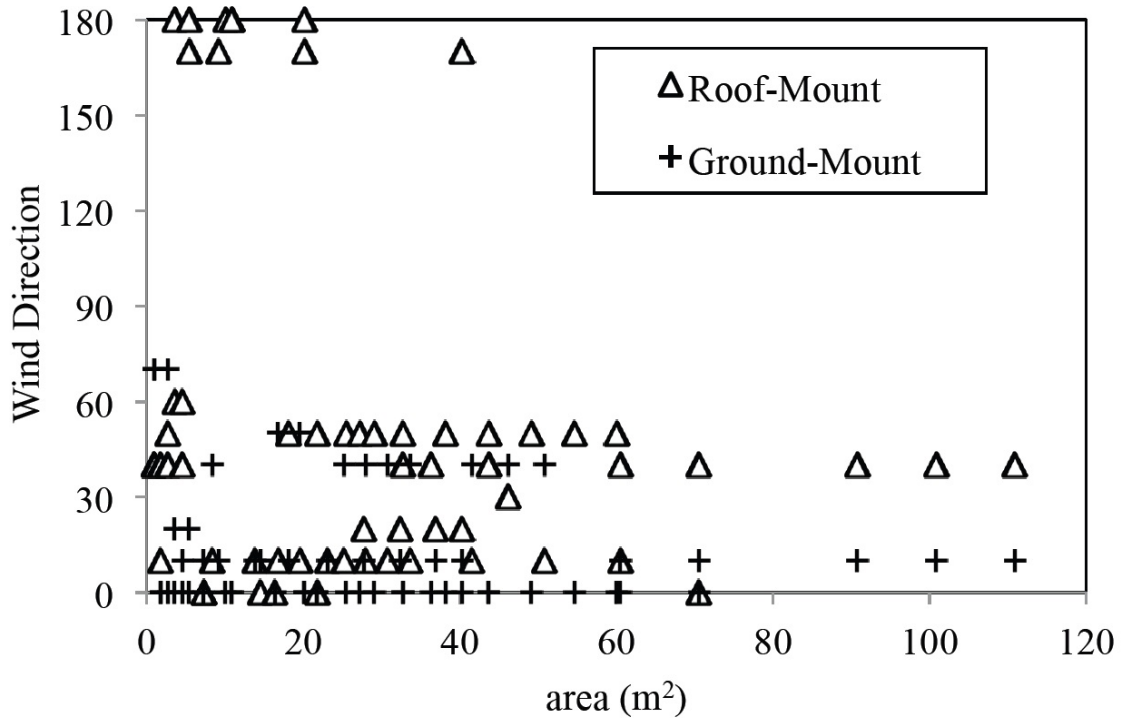


Figure 1.3: Critical wind directions for the worst area-averaged uplifts on PV arrays for various tributary areas, 0° is due north. Reproduced from Kopp *et al.* [16].

While the work of Kopp *et al.* did locate the peak loads on a roof mounted PV array and where on the roof they occur, the mechanisms that resulted in these peak loads are still unclear. The objective of the present work is to examine the flow and mechanisms resulting in the peak uplifts on the panels.

Chapter 2

Experimental setup

2.1 Introduction

To investigate the aerodynamics of roof-mounted PV arrays in greater detail than has previously been possible, a series of experiments were conducted using synchronized TR-PIV (time resolved particle image velocimetry) and pressure measurements. While there have been several studies which have utilized pressure measurements to investigate roof-mounted PV arrays, the use of TR-PIV allows the flow field itself to be analyzed directly in much greater detail than has previously been possible. The primary basis for our study is the work of Kopp *et al.*[16] which indicated that three critical wind directions (those resulting in the highest uplift) exist for roof mounted PV arrays: Southern winds (180°), northern (0°) and northern cornering winds (30° - 60°). These three wind directions were observed to be critical for area-averaged pressure coefficients over various panel areas. This study focussed on the flow-field that develops at the leading edge of the building during southern and northern winds. By focusing initially on the northern and southern winds it is possible to avoid the complications that would be associated with performing PIV for the cornering winds, which would likely necessitate the use of either stereoscopic or dual-plane PIV to resolve the three dimensionality of the flow. Similarly, this experiment will focus on the model north-south centreline to minimize any error associated

with out of plane velocity components; the mean velocity in the cross-stream direction is zero due to symmetry, although turbulence is, of course, always three-dimensional.

2.2 Wind Tunnel Facility

Experiments were conducted in Boundary Layer Wind Tunnel (BLWT) II at the University of Western Ontario's Boundary Layer Wind Tunnel Laboratory (BLWTL). The high-speed test section of BLWT-II has a working cross section 3.4 m wide with a variable height, nominally 2.4 m high at the test section. The length of the upstream fetch to the centre of the turntable is 39 m. The tunnel floor is lined with a series of pneumatically controlled roughness elements which can be raised up to 200 mm above the tunnel floor. Generally, additional turbulence generating elements such as trips and spires are used to achieve the desired boundary layer profiles.

2.3 Model Details

The models used in the present experiments are the same as those used by Kopp *et al.*[16]. The 1:30 length scale of the models was selected so as to balance the constraints of accurately simulating the boundary layer flow while maintaining a large enough model size so as to be able to accurately resolve the flow field [16]. Two tilt angles have been examined in the present study: 2° and 20°. The 2° case represents a flow regime which is largely dominated by pressure equalization effects, while in the 20° case the local flow around the panels becomes increasingly important in dictating loads [16]. A bare roof building was also investigated to provide a base line comparison. Note that in the following discussion of the model details all units are given in (equivalent) full scale units, as is common practice in wind engineering.

The building height, $H = 7.3$ m, was common across all the models and is a typical value for a low rise building. The PV array in the present study covered the entire roof (with appropriate roof edge setbacks and inter panel spacings). The array consisted of 12 rows of 12 modules,

which were mounted on the roof such that the rows run parallel to a roof edge. Solar panels normally tilt towards the south in the northern hemisphere, we use this to establish the N-E-S-W directions. The chord of the modules is 1.00 m, and the length is 1.65 m. Rows were modeled without gaps, hence each row was 20 m long and the total size of the array was 240 m². The roof setback represent a typical minimum distance solar panels would be installed from the roof edge in North America [16]. The spacing between rows of the arrays was selected so as to minimize the total roof area utilized by the array while still minimizing the shading which occurs at lower solar elevation angles. As such, the length of each building was different depending on the roof edge setbacks and inter panel spacings. Full geometrical details are given in Table 2.1.

Experiments were conducted at a wind tunnel reference speed of approximately 15 m/s. The reference speed was measured above the boundary layer at a height of 1.47 m above the tunnel test section floor. The Reynolds number, based on the model height and roof height mean velocity was 1.9×10^5 . As noted by Kopp *et al.*, the full-scale Reynolds number would larger by a factor of the length scale multiplied by the velocity scale [16]. Thus, the experiments were conducted at a Reynolds number approximately two orders of magnitude too low, however, this is still one order of magnitude higher than the minimum allowed in the ASCE # 49-12 [20]. The blockage ratio of the the models was less than 3%.

The coordinate system used herein, described in Figure 2.1, is always referenced to the leading edge of the building and the centreline of the building. Thus, the origin lies at the centre of the leading edge of the roof, the x-axis runs along the roof parallel to the mean wind direction, the z-axis is in the vertical direction, and the y-axis runs laterally across the roof.

2.4 Terrain Simulation

The experiments were conducted in a simulated open country terrain characterized by a roughness length, z_0 , of 0.03 m. The terrain simulation was achieved by matching the wind tunnel

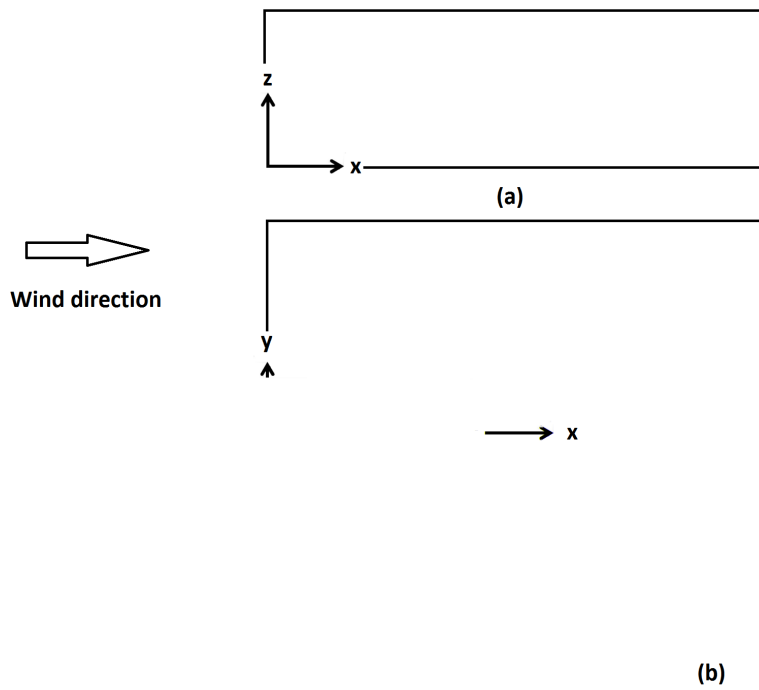


Figure 2.1: Coordinate system definition: (a) section view through centre of building; (b) plan view of the building.

Table 2.1: Geometrical details of the buildings and arrays (in equivalent full-scale dimensions)

| | Bare Roof (m) | 2° Tilt Angle (m) | 20° Tilt Angle (m) |
|--|------------------|----------------------|-----------------------|
| Roof height | 7.3 | 7.3 | 7.3 |
| Building length (N-S) | 15.9 | 15.9 | 23.9 |
| Building width (E-W) | 22.5 | 22.5 | 22.5 |
| Panel inter-row spacing | N/A | 1.12 | 1.68 |
| Panel roof setback from northern edge | N/A | 1.45 | 2.10 |
| Panel roof setback from southern edge | N/A | 1.20 | 1.97 |
| Panel roof setback from east/west edges | N/A | 1.22 | 1.22 |
| Panel roof clearance | N/A | 0.10 | 0.16 |

profiles to the ESDU (Engineering Science Data Unit) mean profiles, ESDU turbulence intensities and ESDU velocity spectra [21, 22, 23]. Kopp *et al.* [16] measured streamwise and vertical velocity profiles using an X-wire probe and compared these to the target profiles. Figure 2.2 shows the comparison of the experimental streamwise velocity and turbulence intensity profiles with the target ESDU profiles. The velocities are normalized at a height of 10 m in equivalent full-scale units. Figure 2.3 shows experimental and ESDU streamwise and vertical velocity spectra at roof height (7.3 m). There was excellent agreement between experimental and target mean and intensity profiles within the range of the building’s height. The agreement between the measured and target spectra were felt to be reasonable given the large scale of the flow simulation [16].

2.5 Measurement System

2.5.1 Surface Pressure Measurements

Surface pressure measurements were obtained using pressure scanners connected to pressure taps via a tubing system. The tubing system, fully described in Ho *et al.*[24], has a flat fre-

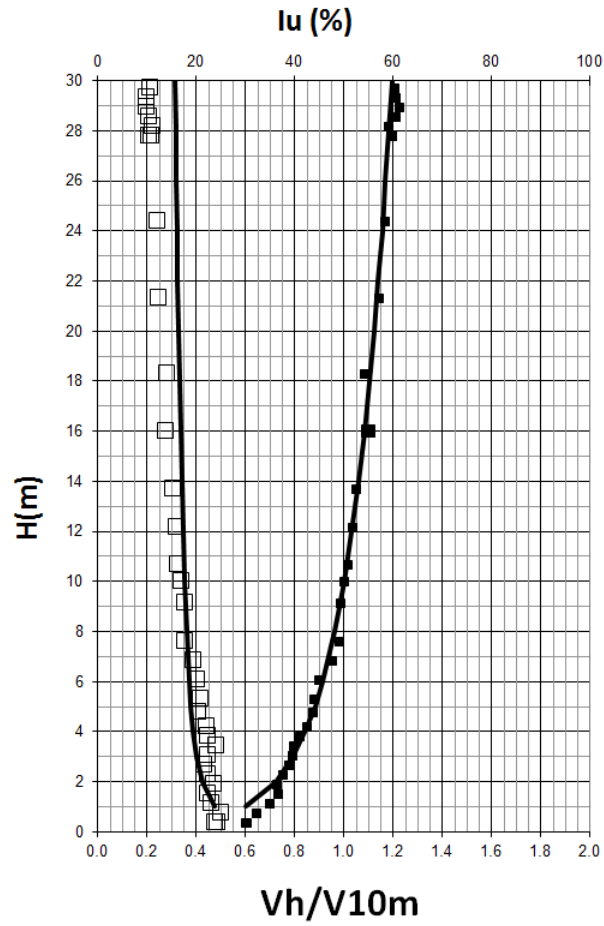
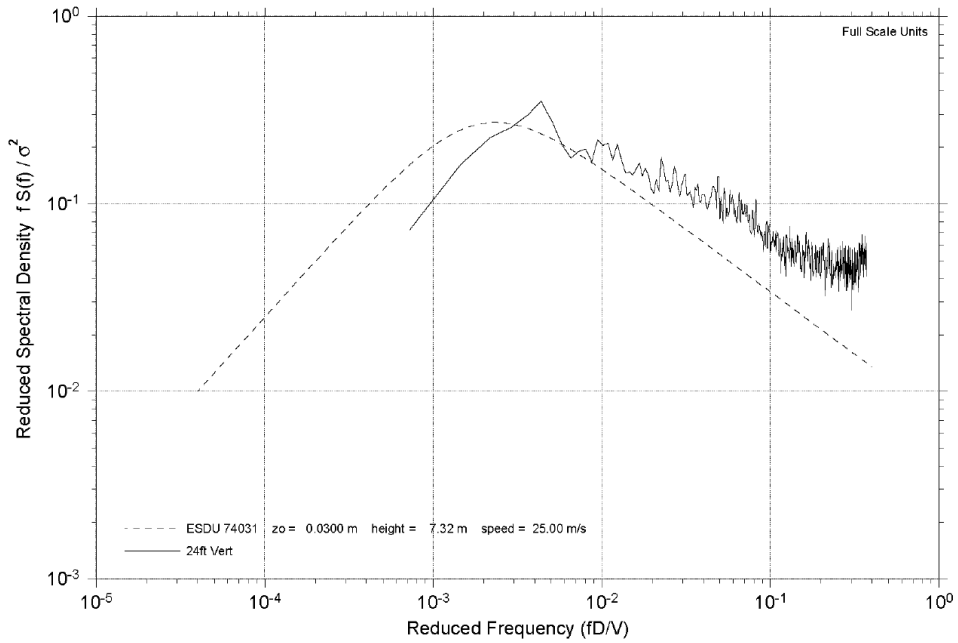
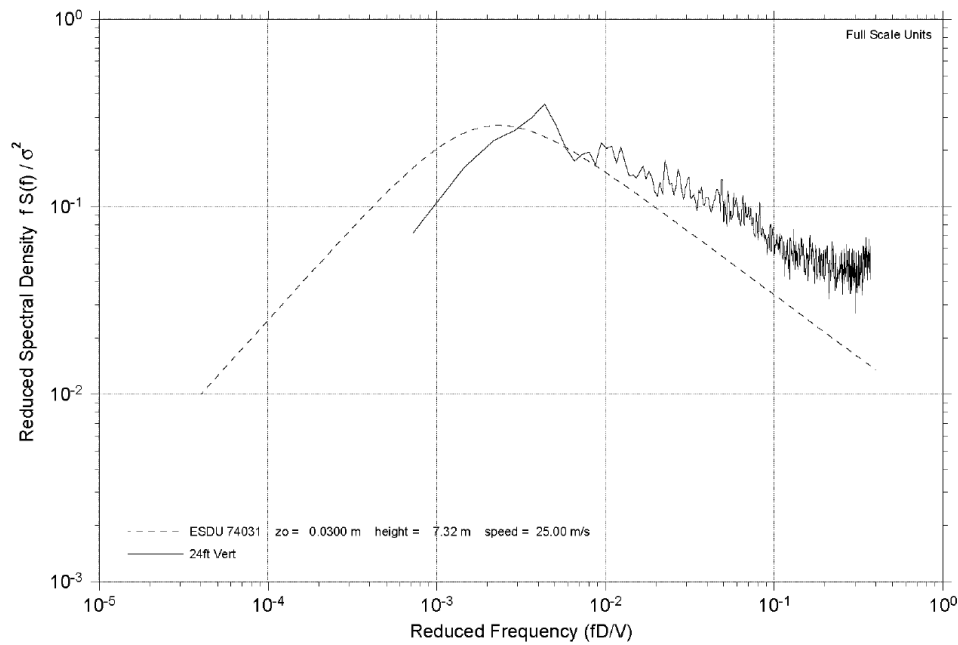


Figure 2.2: Mean streamwise velocity and turbulence intensity profiles. Symbols: \square , I_u ; \blacksquare , V_h/V_{10m} . Data points are experimental measurements, while solid lines are the ESDU profiles for $z_0 = 0.03$ m. Reproduced from Kopp *et al.* [16].



(a) Streamwise velocity fluctuations



(b) Vertical velocity fluctuations

Figure 2.3: Spectra of velocity fluctuations. Experimental data are solid lines while dashed lines are the ESDU target spectra for $z_0 = 0.03$ m. Reproduced from Kopp *et al.* [16].

quency response up to 200 Hz. Pressures were measured on the upper and lower surface of the PV panels along three columns of taps, located along $y = \pm 0.12H$ and $y = -0.24H$, for a total of 144 taps; both the 2° and the 20° tilt angle models had the same pressure tap layout, shown in Figure 2.4. The bare roof building was instrumented with two columns of 96 pressure taps, located at $y = \pm 0.078H$, also shown in Figure 2.4. In general pressures from only a single column of taps corresponding to the position of the plane of the PIV data, will be reported. Since the columns of taps are located at approximately the centreline of the roof, this single set of pressure results will be referred to as the centreline pressures.

Pressures were sampled for 180 seconds at a frequency of 1108 Hz and low pass filtered at 200 Hz. The sampling frequency was set to the system maximum in order fully resolve the PIV camera triggers without aliasing for synchronization purposes, as discussed in Section 2.5.3. Measured pressures were referenced to the dynamic pressure near the top of the wind tunnel and recorded in the form of a pressure coefficients; the upper zone of the tunnel has uniform flow with relatively low turbulence levels. Pressure coefficient are defined by

$$C_{p,ref} = \frac{(p - p_{ref})}{\frac{1}{2}\rho\bar{U}_{ref}^2} \quad (2.1)$$

where p is the pressure, p_{ref} is the pressure at the reference position and \bar{U}_{ref} is the mean velocity at the reference position. These pressure coefficients were then re-referenced to the dynamic pressure at roof height using the following conversion from Ho *et al.* [24],

$$C_{p,H} = (C_{p,ref})(q_{ref}/q_H) \quad (2.2)$$

where q_{ref} and q_H are the dynamic pressures at the measurement reference height and at building height, respectively. The conversion factor q_{ref}/q_H is determined from the mean wind tunnel boundary layer velocity profiles determined from the X-wire probe measurements presented in Section 2.4. It has been found that aerodynamic data which is referenced to the roof height velocity produces the least variability [24]. Quiroga assessed the measurement uncer-

tainty for this system and found that the total uncertainty on the pressure coefficients at roof height was 12.9% [25].

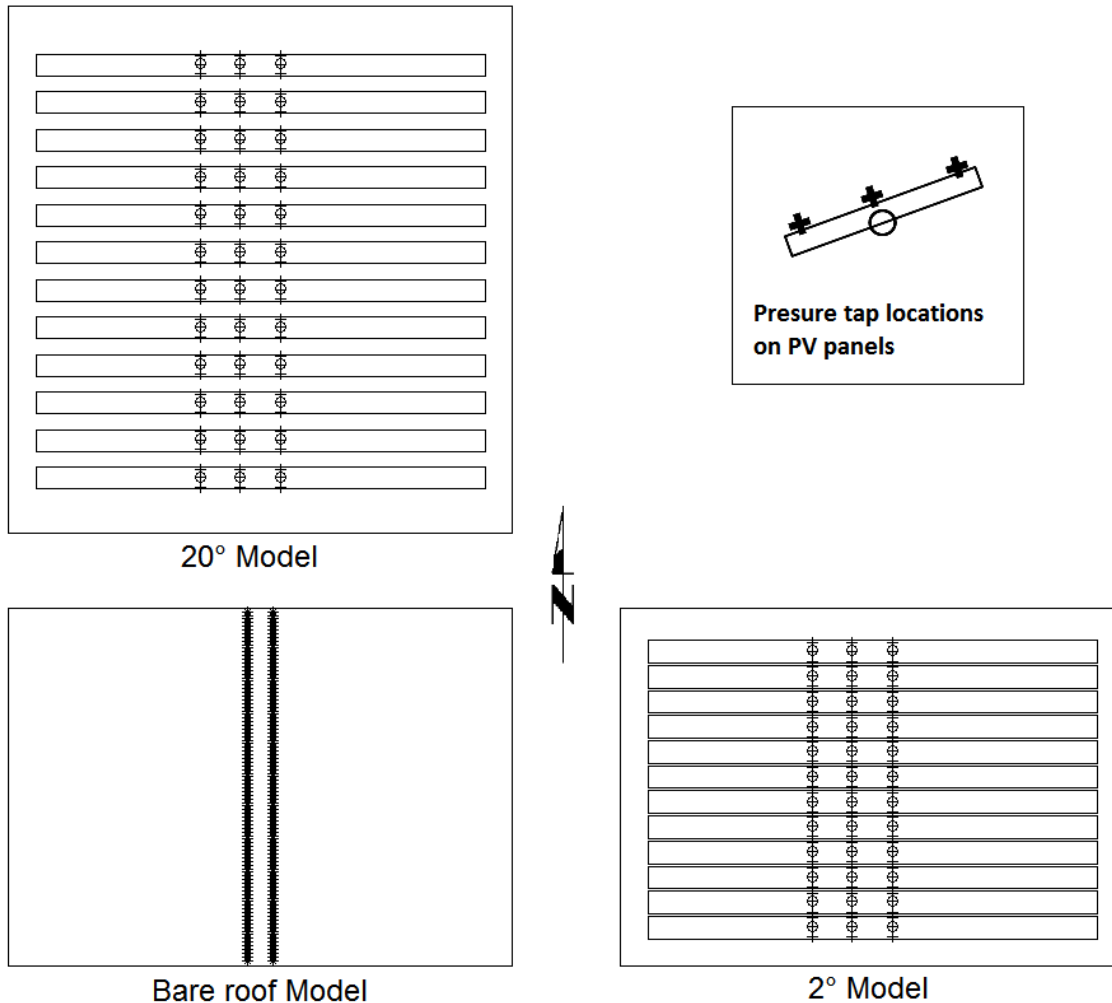


Figure 2.4: Location of the pressure taps on the PV array and the roof of the building: upper surface taps are indicated with by the symbol, ○, while lower surface taps are indicated with the symbol, +. Taps on the roof surface are indicated with the symbol, *.

2.5.2 Particle Image Velocimetry Measurements

In order to investigate the flow field with good spatial and temporal resolution the TR-PIV system developed at UWO's BLWTL was utilized to measure flow field velocities. The TR-

PIV system at UWO is unique in that it has the capability to stream PIV data at both the same frequencies and durations typical of wind engineering wind tunnel pressure experiments. Previous TR-PIV systems have been restricted to approximately 8 seconds of data (based on 1 megapixel images at 500 Hz) due to limitations in random access memory [26]. This is significantly shorter than the 160 seconds required to match the pressure experiments of Kopp *et al* [16]. UWO's TR-PIV system is able to continuously capture 1 megapixel PIV data at 500Hz, on two cameras, for approximately 16 minutes; the system has a total storage capacity of 4 TB (or 2 TB per camera).

The light source is a double-head diode-pumped Q-switched, Nd:YLF laser operating at 1000 Hz. The seeding particles used in this study were created by atomizing olive oil. Images were captured using two Photron FASTCAM-1024PCI CMOS cameras operating in tandem. The cameras have a spatial resolution of 1024x1024 pixels and the system is able to stream individual images to a PC at 1000 Hz, giving a sampling rate of 500 Hz for velocity data. Full details of the TR-PIV system can be found in Taylor *et al.* [27]. The experimental setup, showing the position of the cameras and the laser sheet illuminating the field of view is depicted in Figure 2.5.

The velocity data were computed from PIV image pairs using the FFT cross-correlation method with a 32x32 pixel interrogation windows and 50% overlap. The raw vector fields were post-processed using a global standard deviation filter, followed by local mean and median filters. Erroneous vectors that were identified were replaced with interpolated data. Typically less than 5% of the vectors were rejected and interpolated, after vectors near the edges of the field of view and model surfaces were removed. The commercial TSI software package, INSIGHT 4G, was used to process and post-process the data. Standard cross-correlation algorithms have been shown to have a spatial uncertainty of approximately 0.1 pixels [28].



Figure 2.5: Photograph of experimental setup showing positioning of the two fields of view and the laser sheet.

2.5.3 Pressure and Velocity Data Synchronization

One of the difficulties in the present experiments was the synchronization of the pressure and velocity data, given that the pressure data acquisition system (DAQ) and the PIV system were both designed to operate independently of each other. Synchronization was achieved by connecting the PIV camera triggers to the pressure DAQ analog input. The pressure data was oversampled at a frequency of 1108 Hz so as to be able to resolve the 500 Hz PIV camera triggers without aliasing. The first camera trigger was then used to synchronize the start of the PIV data with the pressure data. The pressure time histories were then trimmed to match the PIV data series. Vector fields during peak events were compared to pressure distributions in order to subjectively assess that the synchronization was correct.

After synchronization the pressure and velocity time series were approximately 160 s long. Assuming a full-scale gust speed of 45 m/s at 10 m (giving a velocity ratio of 1:2.6), the resultant full-scale sampling period is approximately $\frac{1}{2}$ an hour.

2.6 Pressure area averaging

To calculate net pressures acting on each panel area-averaged pressure coefficients are calculated by integrating around the ring of four taps located on each panel (three on the top surface and 1 on the bottom surface). The net area-averaged pressures are defined such that uplifts on panels are negative while downward net pressures are positive. In order to examine how the aerodynamic loads on the PV panels compare to those on a bare roof, area-average pressure coefficients were calculated by creating imaginary panels on the roof surface. Since the bare roof building had the same dimensions as the 2° tilt angle model, the imaginary panels were created by projecting the area of the 2° panels onto the roof's surface. By integrating the pressures across the taps that fall within this projected area, net pressure coefficients for the imaginary panels are obtained.

Chapter 3

General flow field descriptions

3.1 Low-rise building

3.1.1 Flow field over the roof

3.1.1.1 Mean velocity

In order to inform the following discussions of the aerodynamics of roof-mounted PV panels, the flow over the roof of a bare low-rise building was first investigated. Again, the present study focused on the leading edge flows for north and south winds, that is, a wind perpendicular to one of the building's walls, when no array is present. The mean streamwise velocity profiles and vertical velocity profiles are shown in Figures 3.1 and 3.2, respectively. The velocities here (and throughout, unless noted) are normalized by the roof-height mean velocity (\overline{U}_H) while the lengths are normalized by the mean reattachment length, \overline{x}_r . The mean reattachment point, $\overline{x}_r = 1.01H$, where H is the building height, was estimated by locating the point at which the mean flow near the wall changes from reversed flow to forward flow along the streamwise direction. Due to surface reflections accurate velocity measurements could only be made to within $0.01H$ of the roof surface. The accuracy of the determination of the reattachment point is also affected by the resolution of the PIV measurements, as the grid spacing between data

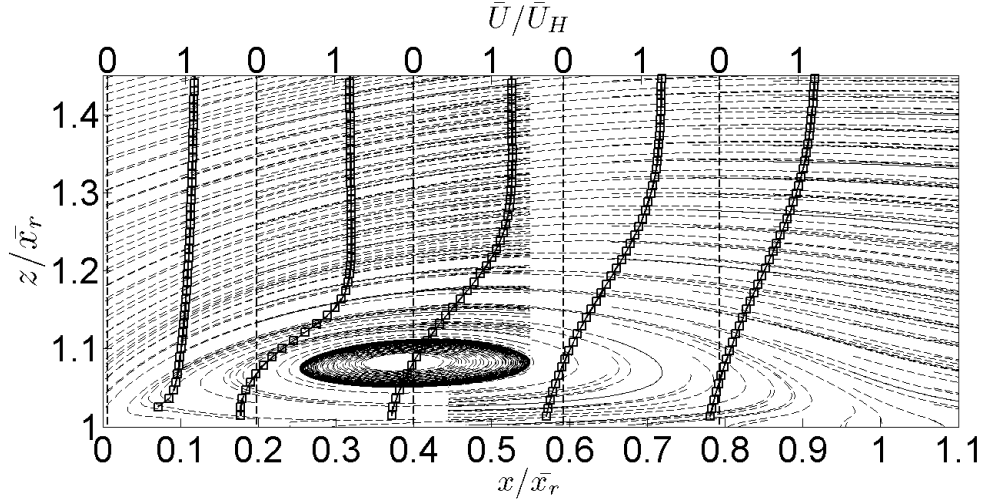


Figure 3.1: Mean streamwise velocity profiles for a north/south wind. Streamlines are shown as dashed lines for reference.

points is $0.0107H$. Kim *et al.* [29], also using PIV, found the same reattachment length for a surface mounted rectangular prism in a turbulent boundary layer characterized by a boundary layer depth of $\delta/H = 16.25$. The streamwise turbulence intensity, $I_u \approx 20\%$, at roof height for Kim *et al.*'s experiment was similar to the present experiments.

As discussed in Section 1.1.1 the main flow feature at the roof's leading edge is the separating-reattaching shear layer which encapsulates a recirculation bubble. At the leading edge the flow accelerates vertically to pass over the building and the separation bubble. Within the separation bubble we observe reversed flow near the roof, due to clockwise circulation within the bubble.

3.1.1.2 Reynolds stresses

The separated shear layer is characterized by strong velocity fluctuations as demonstrated by the Reynolds normal stresses plotted in Figures 3.3 and 3.4. In the separated region the streamwise Reynolds normal stresses, $\overline{u'u'}$ are on the order of 3-6 times larger than the vertical Reynolds normal stresses, $\overline{w'w'}$. Of course the separated shear layer is also associated with elevated Reynolds shear stress, $\overline{u'w'}$, levels, shown in Figure 3.5. It also appears that the

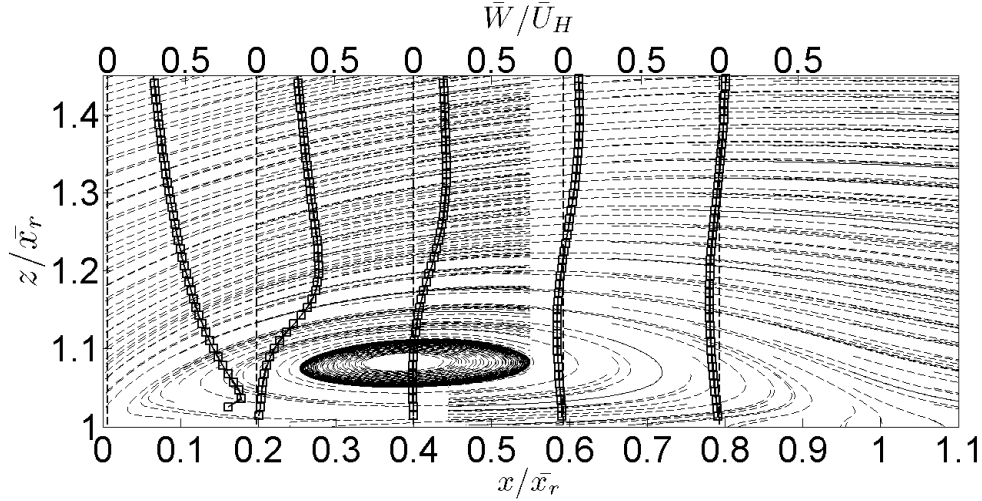


Figure 3.2: Mean vertical velocity profiles for a north/south wind. Streamlines are shown as dashed lines for reference.

Reynolds stresses induced by the separation of the flow at the leading edge of the building are much larger than the background levels present in the turbulent boundary layer.

Figure 3.6a shows the maximum Reynolds normal stresses as the flow develops over the roof, normalized by \bar{U}_H^2 . Again, it is clear that $\overline{u'u'}$ is significantly larger than $\overline{w'w'}$. The $\overline{u'u'}$ normal stress reaches a peak at approximately $x/\bar{x}_r \approx 0.3$ after which the maximum $\overline{u'u'}$ stress falls as reattachment is approached. Conversely, both $\overline{w'w'}$ and $-\overline{u'w'}$ stresses reach peak values at $x/\bar{x}_r \approx 0.5$, after which the maximum stresses for both remain relatively constant. Kopp and Sarathi [30] also observed a similar difference in magnitude between the streamwise and vertical Reynolds normal stresses, at the leading edge, in their investigation of the flow over gable roof houses, however it should be noted that such buildings have significant roof slopes. The Reynolds stresses are also plotted in Figure 3.6b, though normalized by ΔU^2 , where ΔU is the velocity difference across the shear layer ($U_{max} - U_{min}$), at the streamwise position of interest, as was done by Castro and Haque [31]. The results of Castro and Haque are included in Figure 3.6b. Castro and Haque's study investigated the separating-reattaching flow which develops over a two-dimensional normal flat plate combined with a rear mounted splitter plate [31]. There are no detailed published comparison data available for Reynolds stresses in the

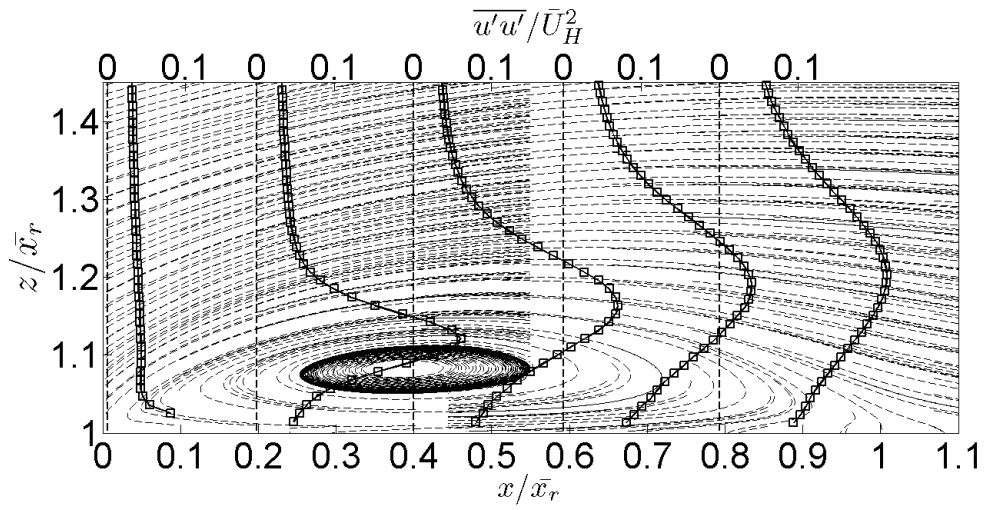


Figure 3.3: Streamwise Reynolds normal stress, $\overline{u'u'}$, profiles for a north/south wind. Streamlines are shown by the dashed lines for reference.

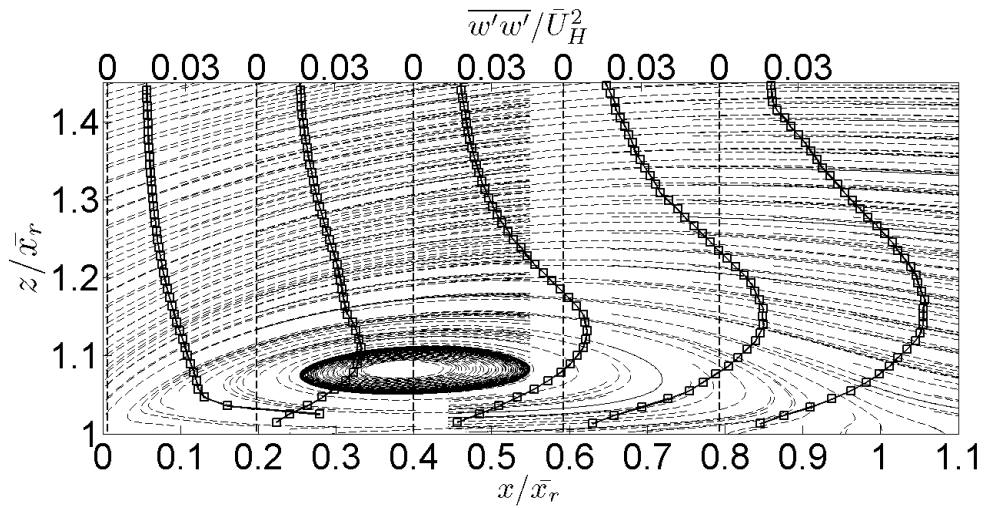


Figure 3.4: Vertical Reynolds normal stress, $\overline{w'w'}$, profiles for a north/south wind. Streamlines are shown by the dashed lines for reference.

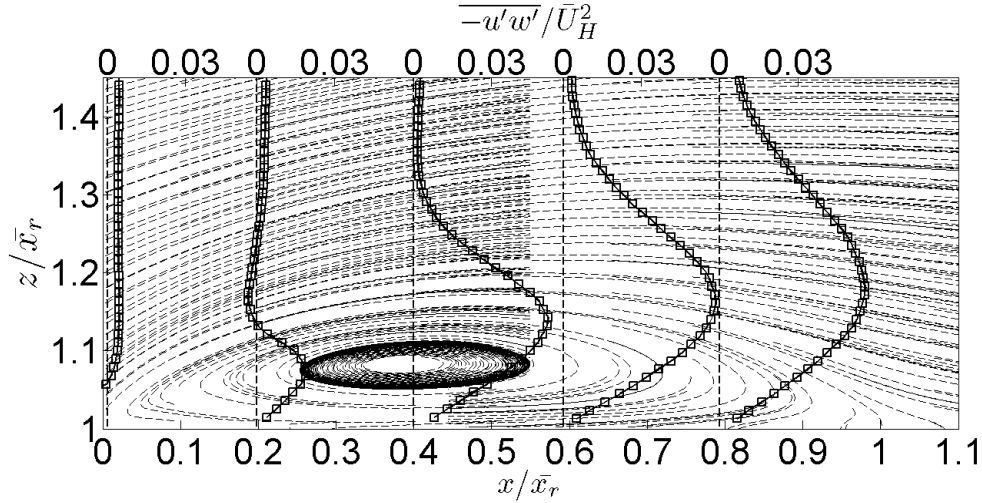


Figure 3.5: Reynolds shear stress, $-\overline{u'w'}$, profiles for a north/south wind. Streamlines are shown by the dashed lines for reference.

separation bubble for a surface mounted object in an atmospheric boundary layer. The normal stresses exhibit the same trend of rising towards reattachment, when normalized by ΔU^2 , as observed by Castro and Haque [31]. However, the current results might not extend far enough past reattachment to display the corresponding drop in normal stresses after reattachment. Furthermore, the initial peak in both $\overline{u'u'}$ and $\overline{w'w'}$ shown in the present results, may not have been captured by Castro and Haque, since their velocity data start at $x/\bar{x}_r \approx 0.13$ [31], and the spatial resolution is lower than that afforded by PIV. The comparison of the Reynolds normal stresses with the results for a normal & splitter plate separating-reattaching shear flow leads to the question as to why the streamwise fluctuations are so much larger than the vertical fluctuations? Particularly, if, as postulated earlier, the shear layer generated Reynolds stresses are much larger than those associated with the turbulent boundary layer itself, in which case we would expect a similar relationship between $\overline{u'u'}$ and $\overline{w'w'}$ as in the the two-dimensional separating-reattaching flow. It should however be remembered that the two-dimensional flow studied by Castro and Haque [31] represents a much more simplistic scenario than the present case of a flow over a low-rise building. This question is not investigated further herein, despite the apparent gap in the published literature. The primary goal of investigating the flow over a

bare roof is to provide a point of comparison for the following investigation of the flow field over roof mounted PV arrays.

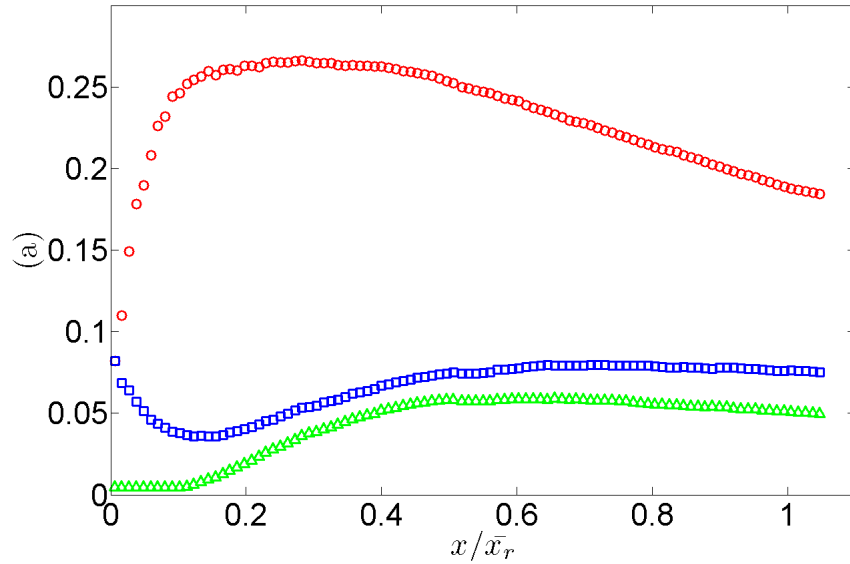
3.1.2 Roof pressure field

3.1.2.1 Mean pressure field

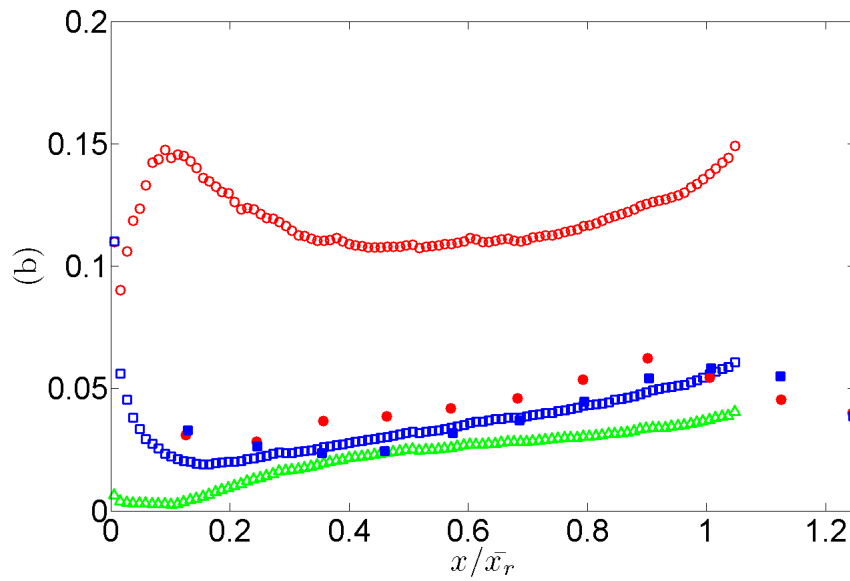
The mean surface pressure coefficients, $\overline{C_p}$, for a north/south wind, are shown in Figure 3.7, normalized by the reattachment length. The mean pressures demonstrate the expected trend for a separating-reattaching flow, that shortly after separation the mean pressure achieves a minima, where $\overline{C_p} \approx -1.6$ followed by a relaxation towards $\overline{C_p} \approx -0.5$. The general trends in the mean surface pressure agree well with results for low-rise buildings, in a similar boundary layer flow, of various heights and a roof slope of 1:12 presented by Ho *et al* [24], however, there is a linear shift in the magnitudes; the present mean pressure coefficients are more negative by approximately 0.2 to 0.3 (refer to Appendix A for a comparison of Ho *et al*'s. results with the present data). This shift is on the high side of the measurement uncertainty, $\pm 12.9\%$, and thus, it suggests a possible leak in the reference pressure tubing for this particular experiment. The geometric differences between the present results and those of Ho *et al*. could also be contributing to the disparity in the mean pressure coefficients. As the goal of the present experiments is to examine flow structures rather than the loads themselves such an error is not expected to affect the final conclusions and no attempt was made to correct the surface pressures. However, it should be emphasized the roof loads should not be used as design loads. From Figure 3.7 it is also clear that the mean surface pressures do not display strong three-dimensionality within the region of $\pm 0.078H$ of the centreline.

For two-dimensional studies of separating-reattaching flows, mean pressure coefficients are often re-normalized by the minimum mean pressure,

$$\overline{C_p^*} = \frac{\overline{C_p} - \overline{C_{pmin}}}{1 - \overline{C_p}}. \quad (3.1)$$



(a) Reynolds stresses normalized by \bar{U}_H^2 .



(b) Reynolds stresses normalized by ΔU^2 .

Figure 3.6: Maximum Reynolds stresses. Symbols: \circ , $\overline{u'u'}$ (present results); \square , $\overline{w'w'}$ (present results); \triangle , $-\overline{u'w'}$ (present results); \bullet , Castro and Haque $\overline{u'u'}$; \blacksquare , Castro and Haque $\overline{w'w'}$ [30].

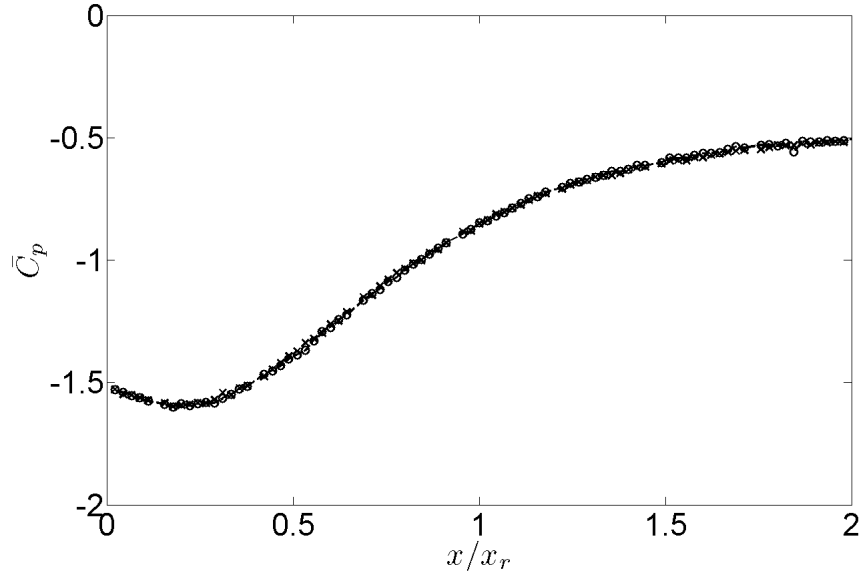


Figure 3.7: Bare roof mean pressure coefficients for a north/south wind. Symbols: \circ , $y/H = 0.078$; \times , $y/H = -0.078$.

If \bar{C}_p^* is then plotted against x/x_r , the pressure distributions collapse to a single curve irrespective of the particular geometry, Reynolds number, or blockage ratio [32]. To see how well these simple geometries compare to a building in a simulated boundary layer flow the present results for the bare roof have been plotted using \bar{C}_p^* in Figure 3.8. The consistency of the \bar{C}_p^* curve is so well defined for two-dimensional separating-reattaching flows that Hudy *et al.* [32] utilized this curve rather than any type of flow visualization to determine the reattachment length. This approach used a universal $\bar{C}_p^* = 0.35$ value at reattachment; this universal value was found to be consistent across numerous studies [32]. For the present experiments $\bar{C}_p^* \approx 0.3$ at reattachment, thus the separation bubble formed at the leading edge of a building of the current size does not exhibit perfect similarity to these more simple geometries, even in the mean sense. Curiously, the value of $\bar{C}_p^* \approx 0.3$ at reattachment agrees fairly well with the results of Roshko and Lau [33] specifically, whose results are for a normal flat plate/splitter plate combination in smooth flow, as shown in Figure 3.8. The \bar{C}_p^* curves for both the present study and the more simple geometries stabilized to a value of $\bar{C}_p^* \approx 0.4$ [32].

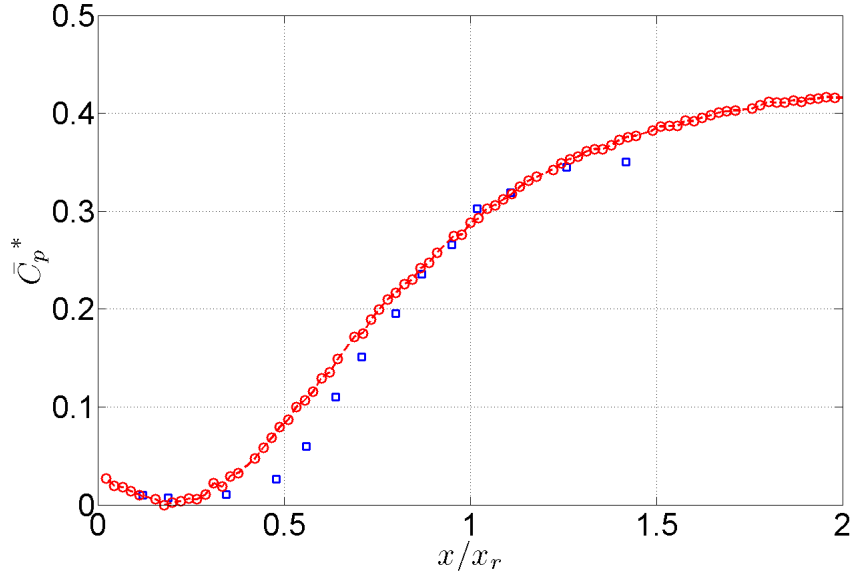


Figure 3.8: Bare roof $\overline{C_p^*}$ distribution for north/south wind (\circ). Normal/splitter plate results from Roshko and Lau [32] are shown for reference (\square).

3.1.2.2 Fluctuating pressure field

Figure 3.9 presents the root-mean-square (RMS) pressure coefficients, \widetilde{C}_p , along the centre-line of the roof for a north/south wind. The peak in \widetilde{C}_p occurs just downstream of the peak in the mean suction. This is in contrast to what is observed for two-dimensional separating-reattaching flows in non-turbulent free-streams, where the peak in the pressure fluctuations occurs just downstream of reattachment [32]. However, as turbulence is added into the freestream, the peak in the pressure fluctuations moves upstream relative to the reattachment point and the \widetilde{C}_p distribution begins to resemble what is observed along the centreline of the roof [10]. Again, the general trends in the RMS surface pressure distribution agree well with the results of Ho *et al.* [24] (see Appendix A), although there is slight change in the slope of the distribution during the relaxation in RMS pressure coefficients following the peak in the fluctuations.

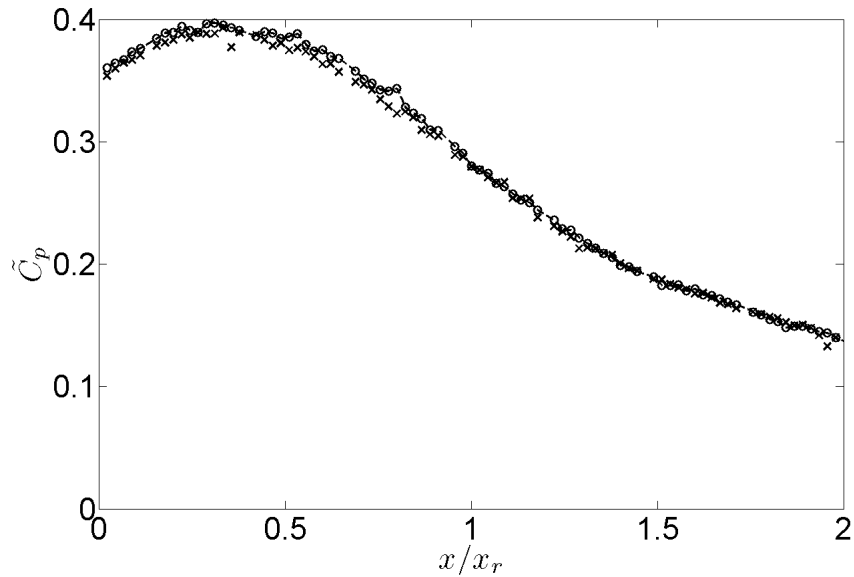


Figure 3.9: Bare roof RMS pressure coefficients for a north/south wind. Symbols: \circ , $y/H = 0.078$; \times , $y/H = -0.078$.

3.2 PV Array

3.2.1 PV Arrays: Flow field

3.2.1.1 Mean velocity

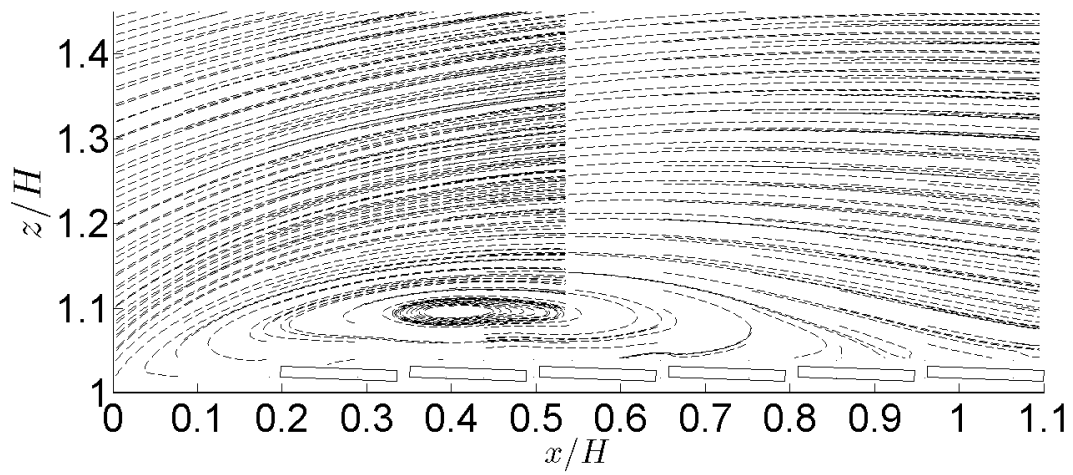
The mean reattachment points, $\bar{x}_r \approx 0.86H$ and $\bar{x}_r \approx 0.85H$, were found for the 2° panel tilt angle system in north and south winds, respectively. That is, the separated shear layer reattached on the 5th panel from the leading edge. Again, the accuracy of this estimate is affected both by the resolution of the PIV data and by the surface reflections. The 2° tilt angle system tended to shorten the separation bubble when compared to the results for the bare roof. For the 20° tilt angle system the presence of the panels perturbs the reattaching shear layer such that the reattachment location is ambiguous. However, from a visual inspection of the streamlines it appears that the separated shear layers have reattached by approximately $x/H \approx 0.8 - 1.0$ for both a north and south wind. Recalling that the mean reattachment for the bare roof occurs at $\bar{x}_r/H = 1.01$ it appears that the scale of the large scale separation bubble is only slightly affected by the presence of the panels on the roof.

The streamlines of the mean velocity for the 20° panel tilt angle and 2° panel tilt angle in both north and south winds are presented in Figures 3.10 - 3.11, respectively. Since the estimate of the reattachment length for the 20° tilt angle system was ambiguous the roof height, H , was seen as a more appropriate normalization for the length scales.

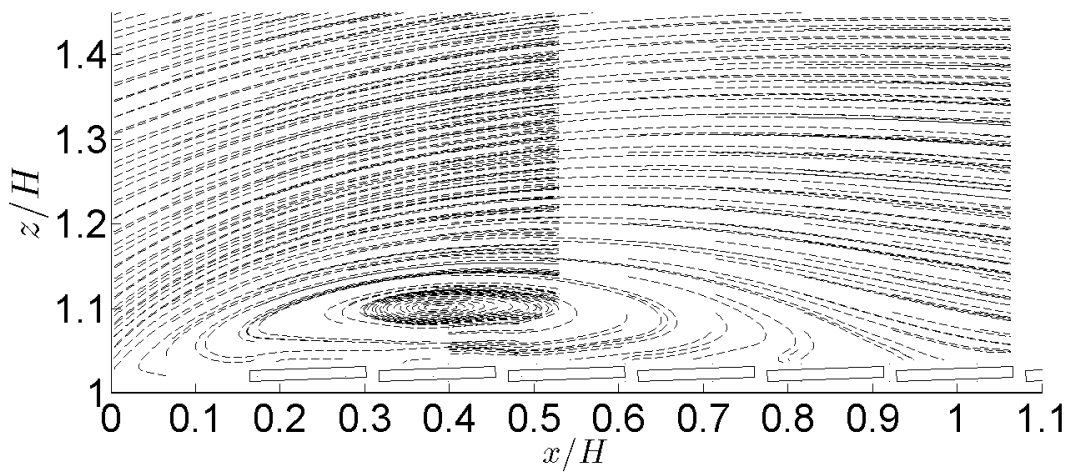
The minimal effect of the panels on the mean flow is further observed by comparing the mean streamwise and vertical velocity profiles with the bare roof profiles, as shown in Figures 3.12a and 3.12b respectively. The mean flow outside the separation bubble is unaffected by the presence of the panels. However, the details of the flow within the bubble are, of course, altered by the panels as they restrict recirculation. For the 20° tilt angle, local recirculation zones form in-between the panels within the larger separation bubble.

3.2.1.2 Reynolds stresses

In contrast to what was observed for the mean velocities, the Reynolds normal and shear stress profiles, shown in Figure 3.13, show that the panels have a significant affect on turbulence around and above the panels. When panels are installed on the roof surface both Reynolds normal (i.e. turbulence levels) and Reynolds shear stresses are markedly reduced when compared to the flow over the bare roof. This was a surprising result since it was originally expected, as surmised by Kopp *et al.* [16], that turbulence levels would be increased by the panels. In fact, not only do the panels decrease turbulence above the roof, but at higher tilt angles this effect is more prominent. What is remarkable is that there is a noticeable decrease in turbulence levels for the 2° tilt angle panels, even though these panels are mounted very close and almost parallel to the roof surface. This suggests that the panels are impeding some mechanism which drives the development of the turbulent structure within the separation bubble. An example of such a mechanism, described for a splitter/normal plate combination, could be the re-entrainment of turbulent fluid at reattachment which provides a positive feedback mechanism to the development of turbulence structure of the separated shear layer [31]. This is not examined further herein.

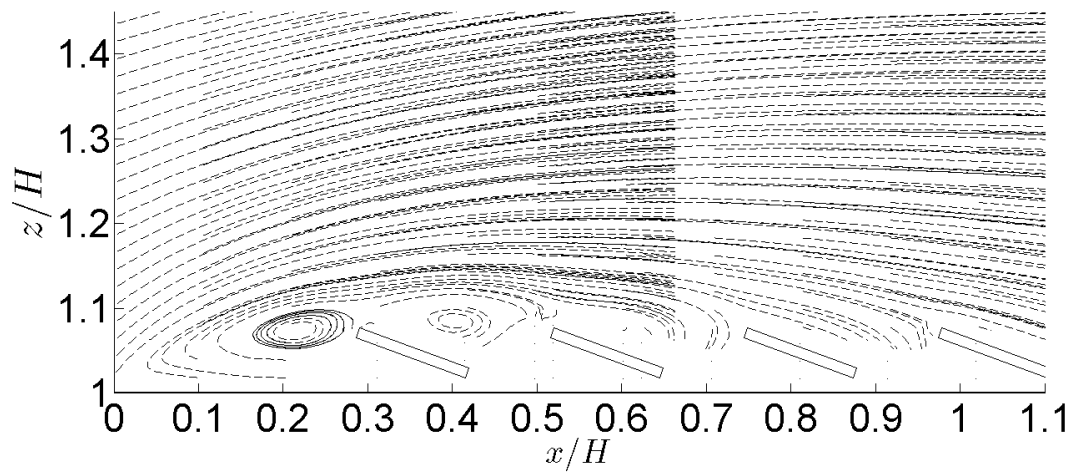


(a) North wind.

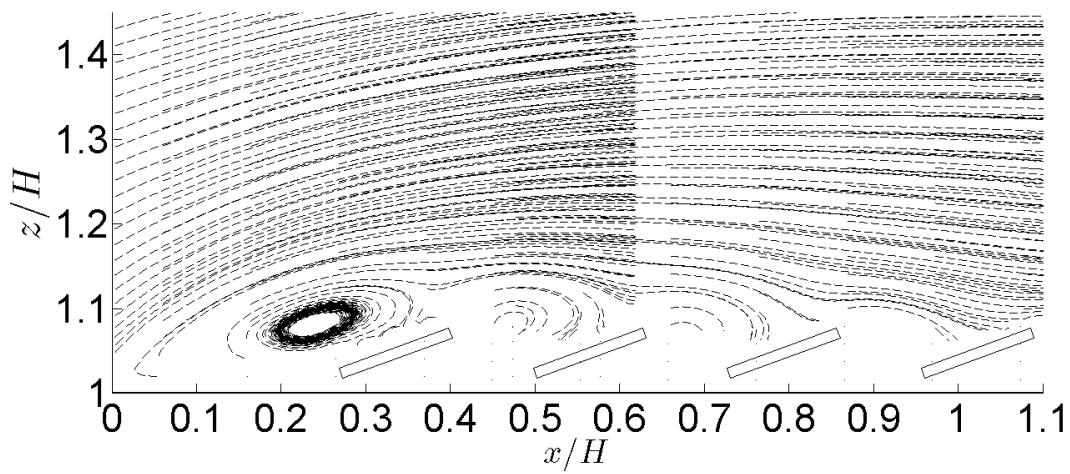


(b) South wind.

Figure 3.10: Streamlines of the mean velocity for 2° panel tilt angle.

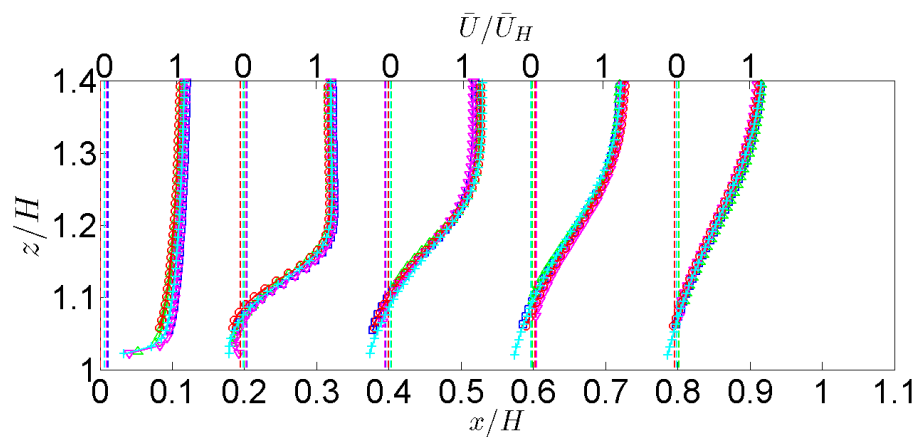


(a) North wind.

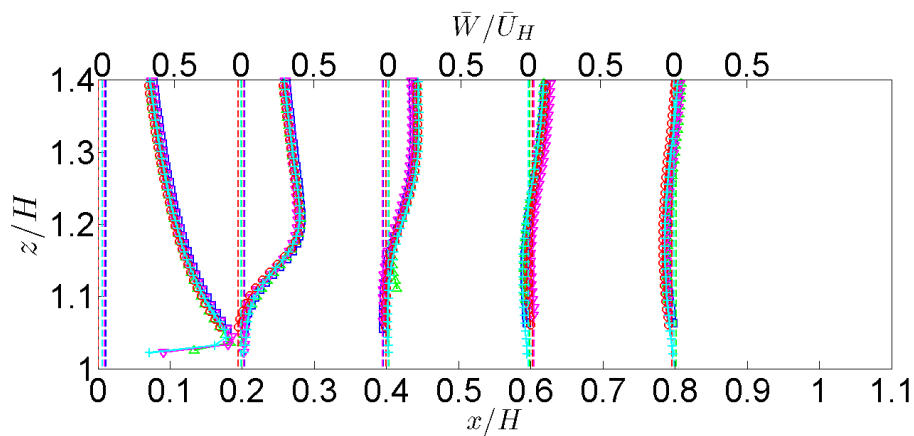


(b) South wind.

Figure 3.11: Streamlines of the mean velocity for 20° panel tilt angle.

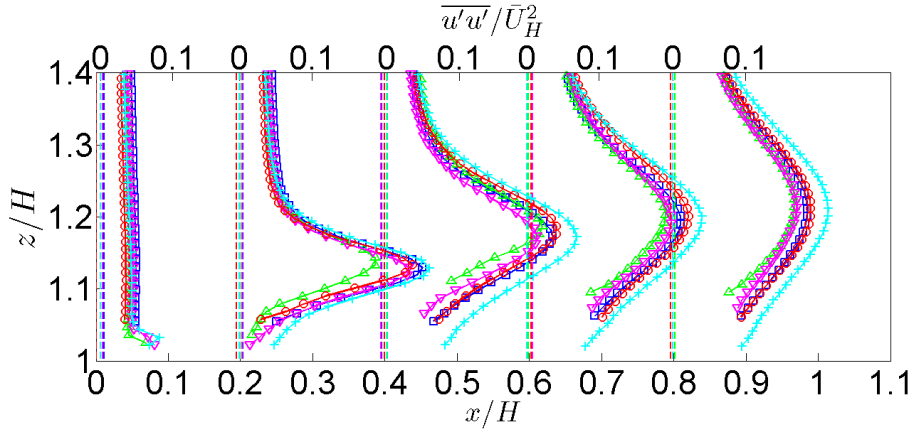


(a) Streamwise velocity

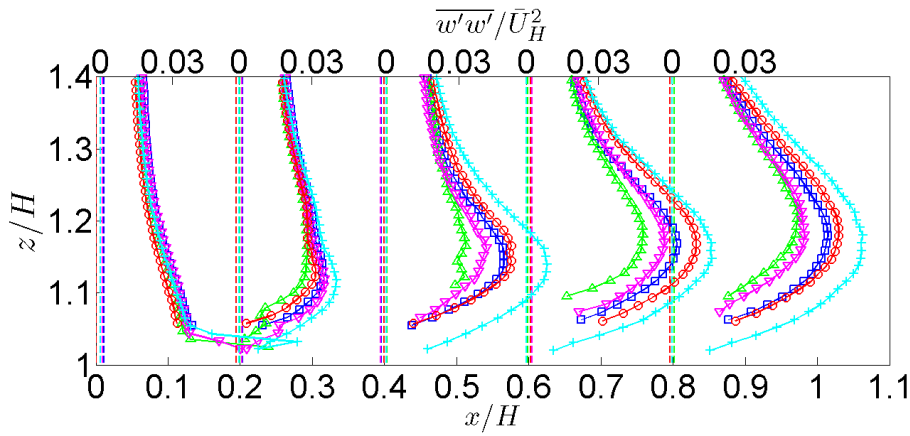


(b) Vertical velocity

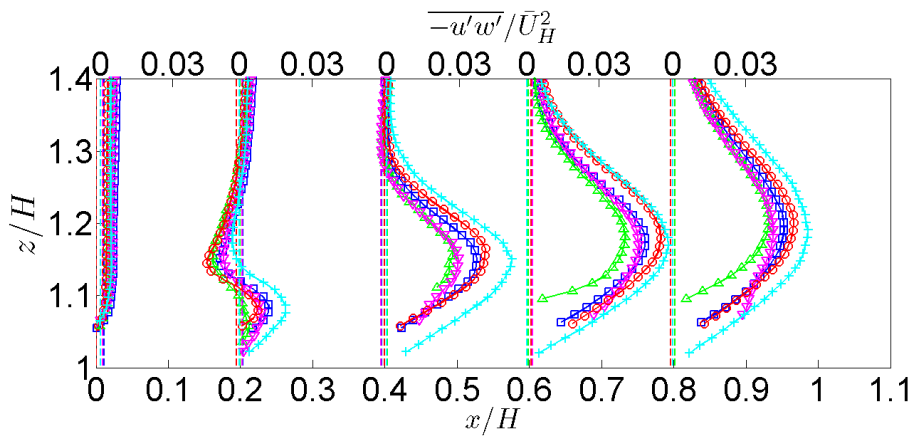
Figure 3.12: Mean velocity profiles. Symbols: +, bare roof; □, 2° north; ○, 2° south; ▽, 20° north; △, 20° south.



(a) Reynolds normal stress, $\overline{u'u'}$.



(b) Reynolds normal stress, $\overline{w'w'}$.



(c) Reynolds shear stress, $-\overline{u'w'}$.

Figure 3.13: Reynolds normal and shear stress profiles. Symbols: +, bare roof; □, 2° north; ○, 2° south; ▽, 20° north; △, 20° south.

3.2.2 PV Arrays: Pressure field

3.2.2.1 Mean pressure field

The mean pressure coefficients along the PV array centreline for both 2° and 20° systems under both north and south winds are presented in Figures 3.14 and 3.15, respectively. Both point pressures on the upper and lower surface of the panels as well as net pressures on each panel are plotted. These results have already been presented by Kopp *et al.* [16], so we review their discussions and add some of our own observations. Note that panels will always be numbered from the leading edge of the building in the subsequent discussions.

One of the most striking features across all four tilt angle/wind direction configurations is that the mean pressure distributions on the upper surfaces of the panels are remarkably similar within the separation bubble. Although there are some differences on the pressures across individual panels, the lowest pressure coefficient on the 1st panel is always approximately $\overline{C_p} \approx -1$ to 1.1, while for all cases the upper surface pressures towards the end of the array tend to stabilize towards $\overline{C_p} \approx -0.2$ to -0.4 . These pressures are similar, though less negative, than what was observed for the roof without any panels observed, where the lowest pressure near the leading edge was $\overline{C_p} \approx -1.6$ while pressures stabilized to $\overline{C_p} \approx -0.5$ to -0.6 . In fact it appears that there is a linear shift of approximately 0.5 when comparing the mean point pressure on the bare roof with the upper point pressures on the various panel arrays; Appendix B contains combination plots of all the data sets. However, since the panels are raised above the roof surface, the relatively large mean suction on the upper surface panels are largely equalized and the net mean loads are much lower than what is experienced by the roof surface itself, as noted by Kopp *et al.* [16]. The current results were found to be in excellent agreement with those presented by Kopp *et al.*[16], as shown in Appendix A.

Focusing first on north winds; for both 2° and 20° systems north winds result in mean down force on the panels within the separation bubble ($x/H \lesssim 1$), with the exception of the first panel for the 2° tilt angle system. Downstream of reattachment, for the 20° panel tilt angle

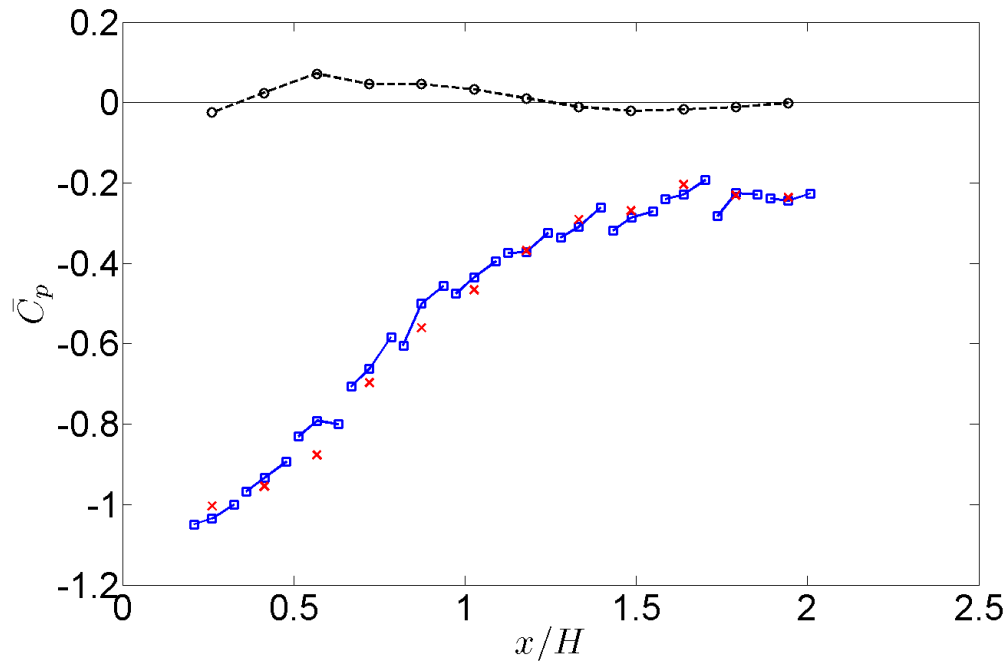
array, we begin to see mean uplifts which grow in magnitude towards the end of the array. If we relate this back to the flow fields presented earlier, we can see that there is reversed flow within the separation bubble near the array which impinges on the upper surface of the panels, resulting in net down-force. Downstream of reattachment, the opposite occurs; the flow tends to separate at the top edge of each panel (characterized by larger suction). This separated flow then impinges the underside of the successive panel, resulting in net uplift.

Conversely for the south winds, the mean uplifts are largest within the separation bubble ($x/H \lesssim 1$). Recall that this wind direction was found to result in some of the largest peak uplifts experienced over the entire array by *Kopp et al.* [16], with these peaks occurring within the separation bubble. As reattachment is approached the net pressures begin to recover and after reattachment mean down forces are observed on the panels. Again, we can relate these pressures to what was observed in the mean flow field: Within the separation bubble there is reversed flow, near the roof surface, which can impinge on the lower surface of the panels causing uplift. Once the flow is reattached, and the flow direction is again forward (relative to the mean flow), local separations occur at the top edge of each panel and the flow then impinges on the upper surface of the next downstream panel resulting in a net down force.

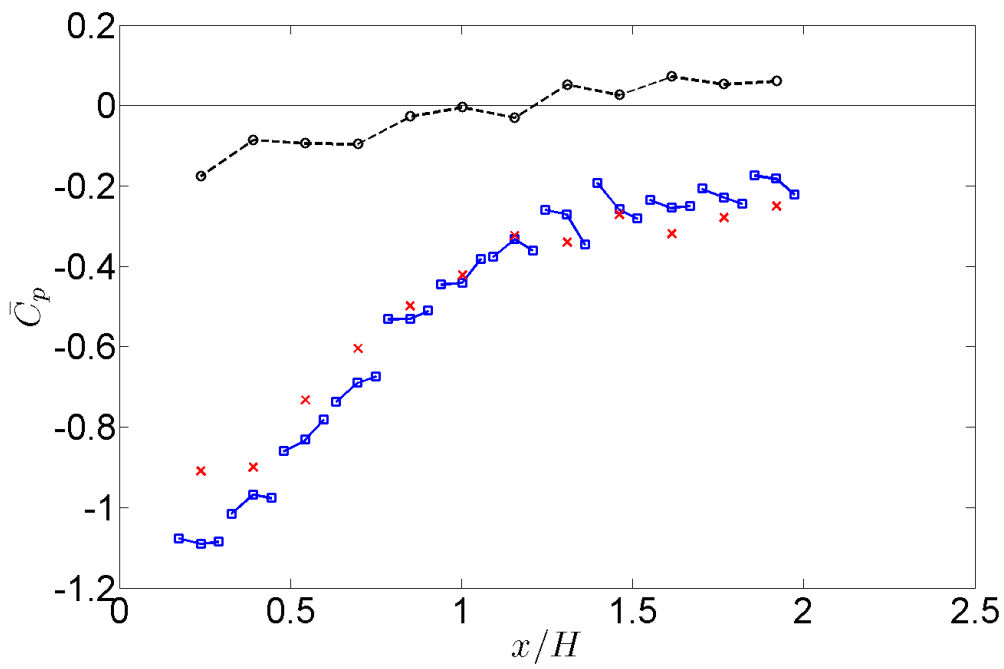
It is evident that the large-scale building generated flow features are clearly defining the zones on the roof in which panels experience mean uplifts or down-forces. However, when comparing the pressures between the 2° and 20° systems it is clear that the details of the local flow around the panels largely control the magnitude of the net loads.

3.2.2.2 Fluctuating pressure field

The RMS pressure coefficients for the four panel tilt/wind direction configurations are presented in Figures 3.16 and 3.17, again panel upper and lower surface point pressures and net pressures are presented. As with the mean point pressure uplifts (i.e. negative pressure coefficients), the largest pressure fluctuations occur in the separation bubble followed by a decrease after reattachment. This decrease continues to the end of the array for the 2° system. However,

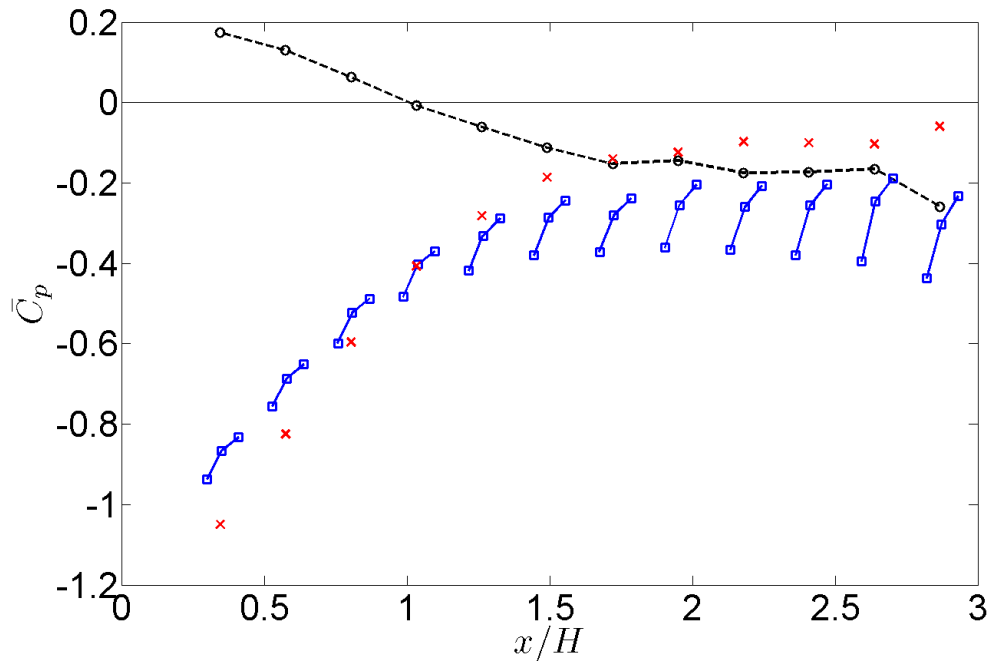


(a) North wind.

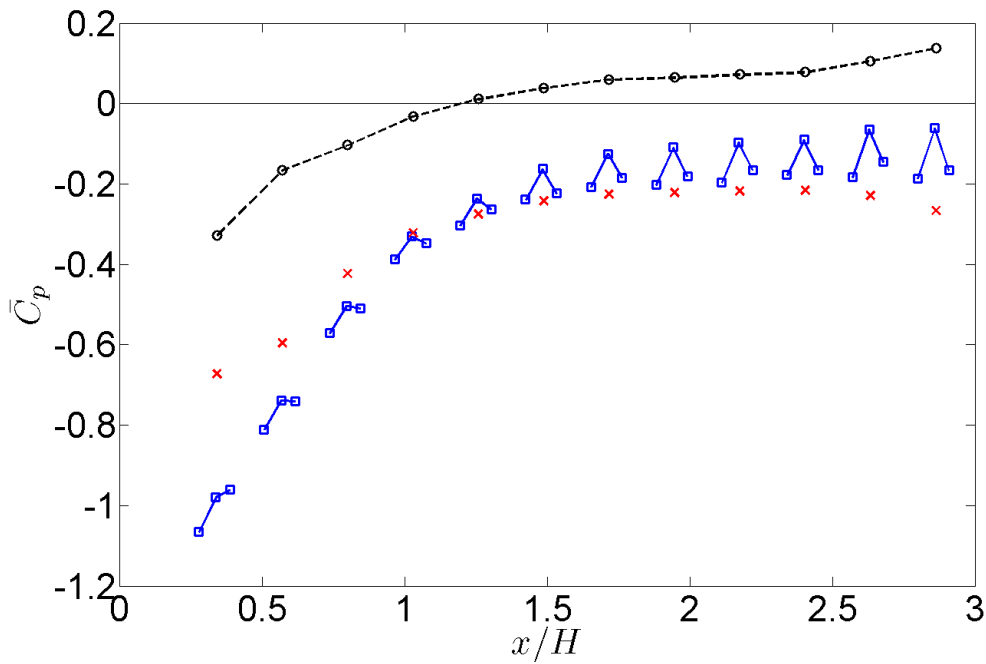


(b) South wind.

Figure 3.14: Mean pressure coefficients, 2° panel tilt angle. Symbols: \circ , Net \bar{C}_p ; \square , Upper surface \bar{C}_p ; \times , Lower surface \bar{C}_p .



(a) North wind.



(b) South wind.

Figure 3.15: Mean pressure coefficients, 20° panel tilt angle. Symbols: \circ , Net $\overline{C_p}$; \square , Upper surface $\overline{C_p}$; \times , Lower surface $\overline{C_p}$.

for the 20° array in a north wind RMS level begin to increase again near the centre of the array, notably on the upper edge of the topside of the panels, caused by local separations at the top of the panels. Kopp *et al.* [16] noted that the stabilization in RMS levels towards the end of the arrays, which is evident to some degree for all configurations, indicating that the flow over the panels is moving towards equilibrium. The current results were found to be in excellent agreement with those presented by Kopp *et al.*[16], as shown in Appendix A.

Kopp *et al.* [16] hypothesized that since the the net roof uplift for building which included a 20° tilt angle PV array were lower versus an equivalent bare roofed building, additional turbulence might de-correlate the overall wind loads. However, already shown in Section 3.2.1.2 the panels actually tend to reduce turbulence levels in the flow. Additionally, if we compare the RMS pressure fields for the panel arrays with the bare roof it is also clear that not only are the fluctuating net pressures generally lower on the PV array, but so are the point pressures. If we consider the point pressures on the upper surface of the array, the fluctuations are lower than those experienced by the bare roof from the leading edge to approximately $x/H \approx 1.5$. So, again, this trend seems to support the fact that the panels are impeding the development of turbulence within the separation bubble, as suggested by our investigation of Reynolds stresses, in Section 3.2.1.2. Furthermore, as the pressure fluctuations rise above the bare roof levels towards the end of the array, it appears that local array generated turbulence also begins to manifest itself in the surface pressure fluctuations. This is most notable for the 20° tilt angle array in a north wind, which would present the bluffest bodies to the reattached flow along the roof (refer to Appendix B for combination plots of all the data sets). While the fluctuations are smaller than for a bare roof, they are still significant and as such peak loads are still quite high [16] as will be discussed further in Chapter 4. For most of the array configurations the surface pressures on the underside of the panels are characterized by lower RMS levels than observed on the panels' topsides. While this is not particularly surprising for the 2° tilt angle system since the panels are so close to the roof's surface, one would expect somewhat similar RMS levels on both sides of the panels for the 20° tilt angle since both sides of the panel are signif-

icantly exposed to the flow. This does seem to be the case for the northern wind direction but not for the southern winds, where RMS levels are notably lower on the panels' lower surfaces.

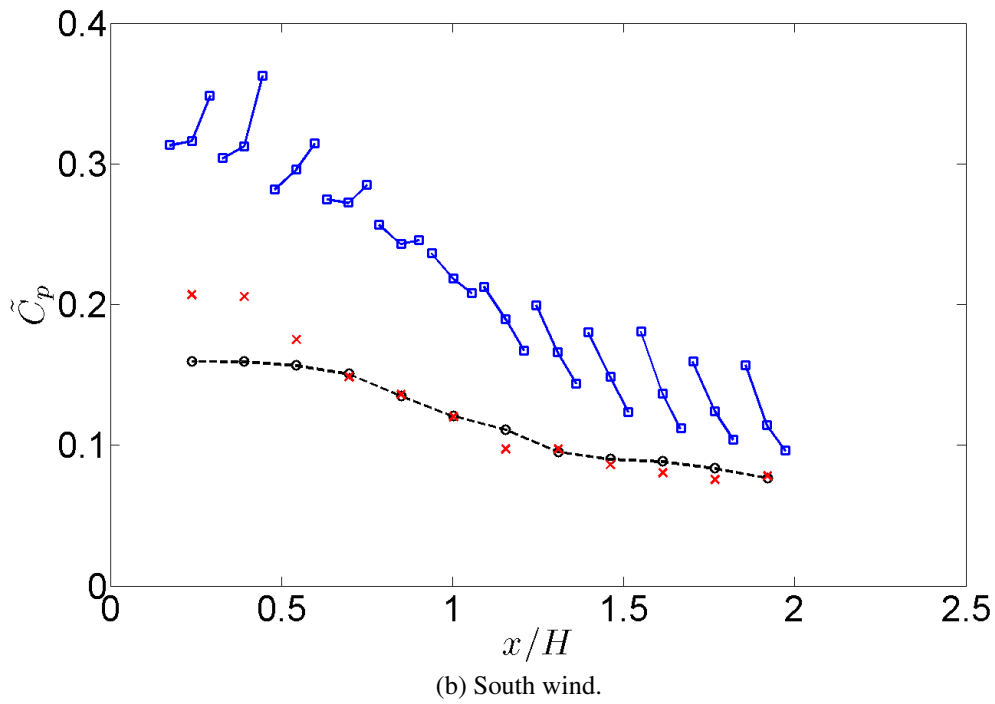
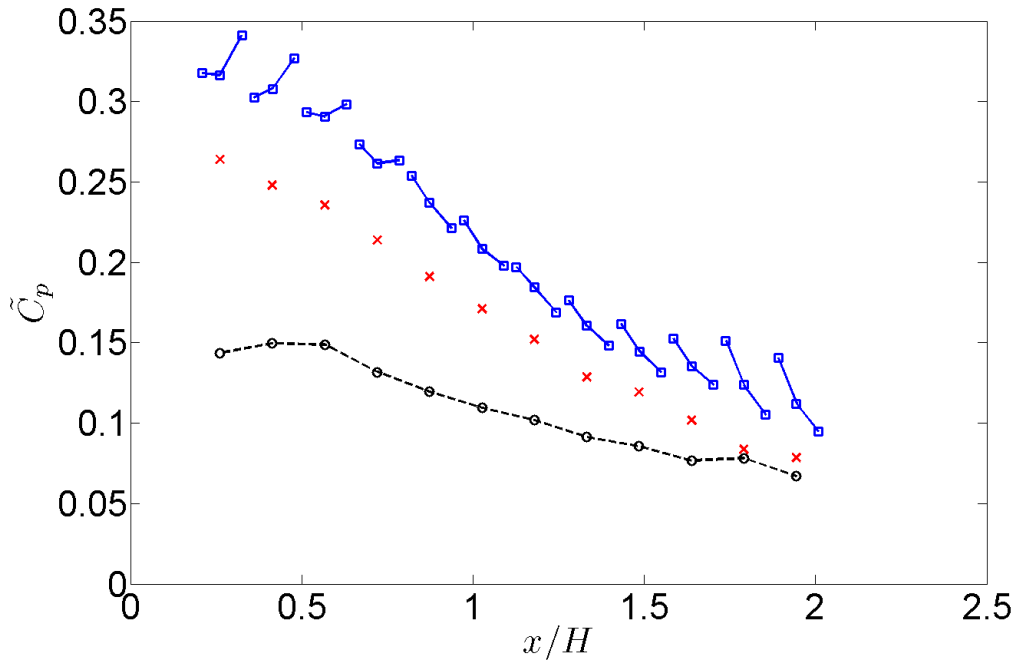
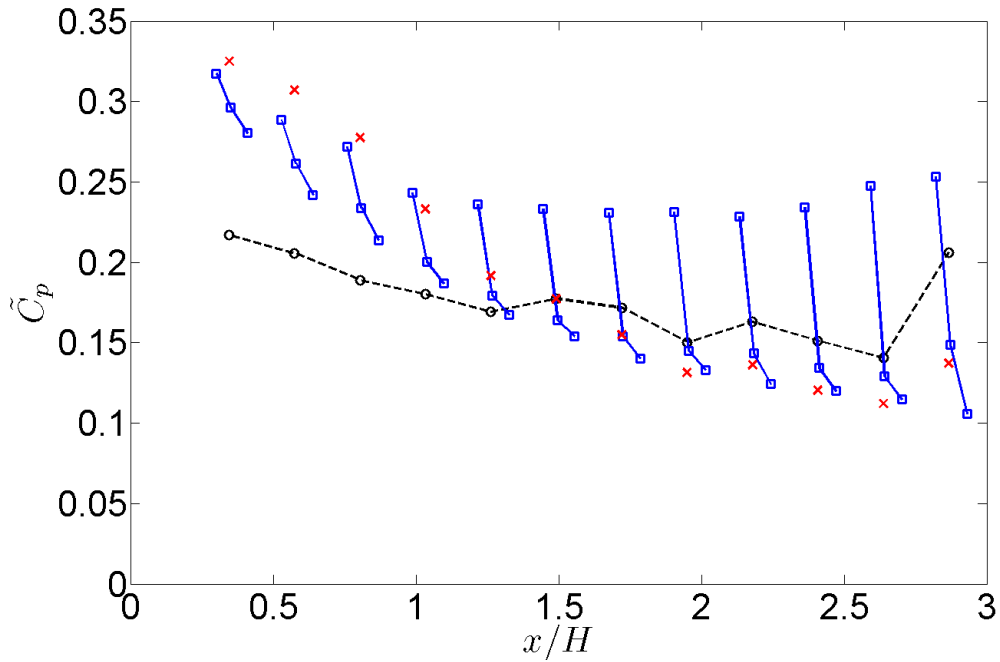
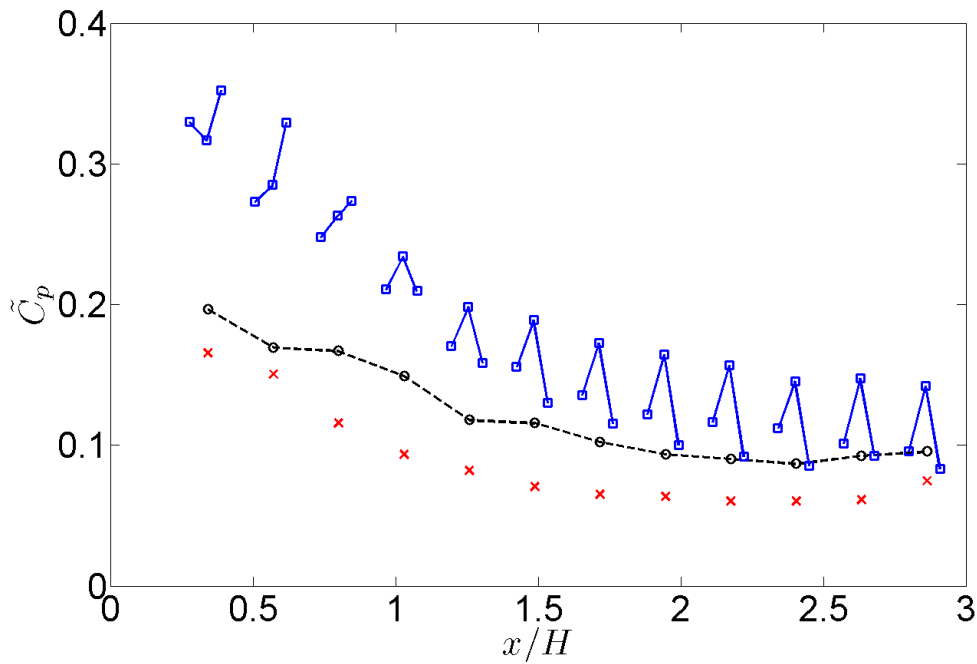


Figure 3.16: RMS pressure coefficients, 2° panel tilt angle. Symbols: \circ , Net \widetilde{C}_p ; \square , Upper surface \widetilde{C}_p ; \times , Lower surface \widetilde{C}_p .



(a) North wind.



(b) South wind.

Figure 3.17: RMS pressure coefficients, 20° panel tilt angle. Symbols: \circ , Net \tilde{C}_p ; \square , Upper surface \tilde{C}_p ; \times , Lower surface \tilde{C}_p .

Chapter 4

Peak uplift events

Peak uplift events are of utmost importance when investigating the wind loads on roof mounted PV arrays as these are the events which could cause system failures. The peak uplift on the panels is a primary design parameter that is required when designing appropriate mounting systems for these arrays. As such it is important to understand the aerodynamic mechanisms which are driving these peak events.

4.1 Peak pressures along the centreline

Figure 4.1a shows the peak uplift net pressure coefficients, \check{C}_p , for the centreline ring of taps around each row of panels, or, in the case of the bare roof, the imaginary projected panel areas as described in Section 2.6. The peaks reported in Figure 4.1a, have been Lieblein-fitted in order to provide more statistically stable quantities than the absolute peak values [24]. Lieblein peaks are calculated by dividing the entire pressure time history into 10 equal segments and determining the peak of each of these segments. The Lieblein BLUE (best linear unbiased estimator) formulation is then used to estimate the mode and dispersion of a Type I extreme value distribution from which the expected peak can be determined [34]¹.

¹It should be noted that these peaks are not the design values since the present results only reflect net uplifts along the centreline of the panels in north and south winds.

The peaks for the bare roof follow the expected trend in that the largest uplifts are experienced at the buildings leading edge within the separation bubble. However, a stabilization in the peaks downstream of reattachment is not observed in contrast to the mean and RMS pressures. Considering the peak loads on the PV panels it is clear that the large peak suction which are experienced near the leading edge by the bare roof are largely equalized across the upper and lower panel surfaces. Comparing the peaks for the 2° and 20° tilt angles under a south wind it is apparent that local flows around the higher tilt angle panels are also influencing the peaks, causing the peaks to be higher for the 20° system.

Downstream of reattachment, the peak uplift net pressure coefficients for the 2° and 20° systems during south winds converge. However, if these two plots were continued with additional panels we would expect them to diverge with lower peak uplifts (less negative net pressure coefficients) on the 20° panels since the reattached flow would begin to result in strong down forces rather than uplifts. Similarly, the convergence of the bare roof and 20° tilt/north wind data are the result of crossover rather than the similarity of aerodynamic mechanisms. This is emphasized in Figure 4.1b where the length-scale has been normalized by panel number rather than by building height. This normalization is also reasonable since, as shown by Kopp *et al.* [16], equilibrium in the aerodynamic loads on the panels is approached once the flow over the panels has stabilized, i.e. a large enough number of panels is required for the loads to reach equilibrium.

The peak factors,

$$g = \frac{|\check{C}_p - \bar{C}_p|}{\overline{C_p}} \quad (4.1)$$

associated with the net pressure coefficients are presented in Figure 4.2a. Again Lieblein-fitted peaks have been used. The peak factor describes the number of standard deviations the peak is from the mean and is an indication of the rarity and relative magnitude of the peaks. Clearly, the peak factors display a significantly higher degree of disorder than the peak values themselves, however we can draw a few conclusions from their analysis.

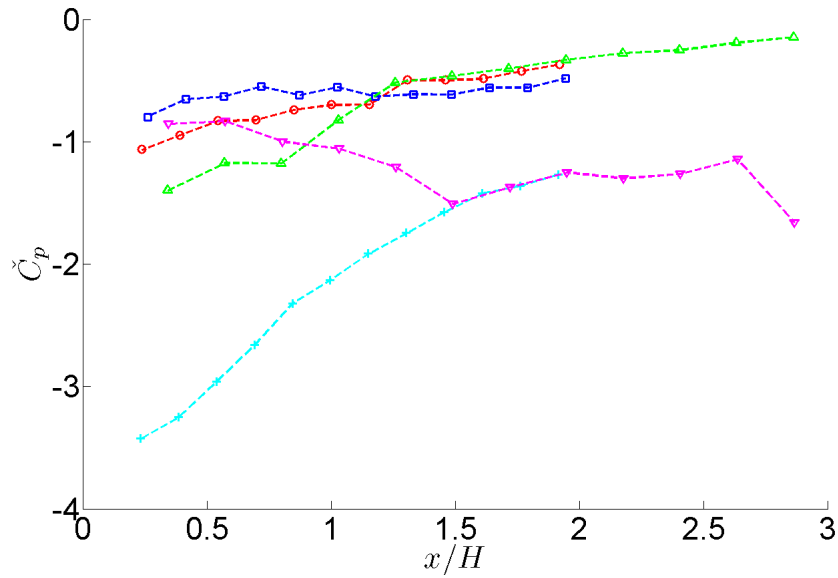
We can consider the peak factors for the bare roof as the base case, representing peaks

which are driven exclusively by the building aerodynamics. The peak factors remain relatively constant at 5 for the entire building, though still higher than what would be expected for Gaussian process; peak factors for a Gaussian process would be $\sim 3.5 - 4.0$. The bare roof peak factors are somewhat similar to the value of 6.2, at $x/D = 0.2$, reported by Saathoff and Melbourne [10] for a two dimensional square prism of dimension D in a turbulent flow. Note that this peak factor is neither Lieblein-fitted nor area averaged, both of which would be expected to decrease the peak factor. The similarity between the square prism and the low-rise building's roof peak factors is quite interesting, since Saathoff and Melbourne's experiment did of course not include any mean shear in the free-stream, suggesting that turbulent intensity might be the more important in driving peak uplifts, rather than the structure of the boundary layer. However, further investigation would be needed to confirm this interpretation.

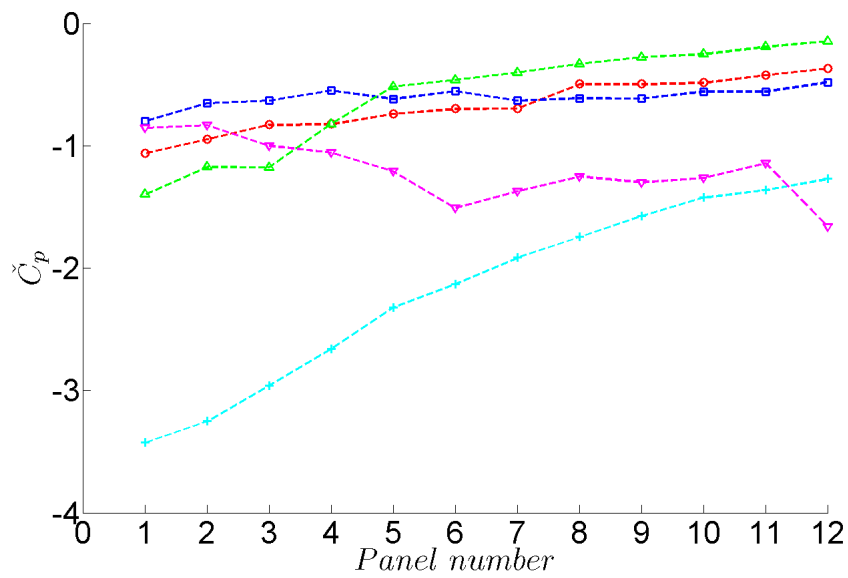
Within the separation bubble, $x \lesssim 1H$, the peak factors for the PV panels are similar to the bare roof, though slightly higher, with the exception of the 20° tilt/south wind case where peak factors reach a maximum around the reattachment point. For both the 2° and 20° tilt angle systems under a north wind the peak factors increase after reattachment, a consequence of the reattached flow impinging on the underside of the panels and driving stronger uplifts.

4.2 Peak uplift flow field analysis

In order to elucidate the aerodynamic mechanisms which are responsible for driving the peak uplift events, the top ten peak uplift events on each of the panels were identified within the pressure time histories. The PIV vector fields associated with these peak events were then examined in depth. To provide a sense of the typical flow structures which are present during peak events, ensemble averages were calculated from these ten peak events, for both

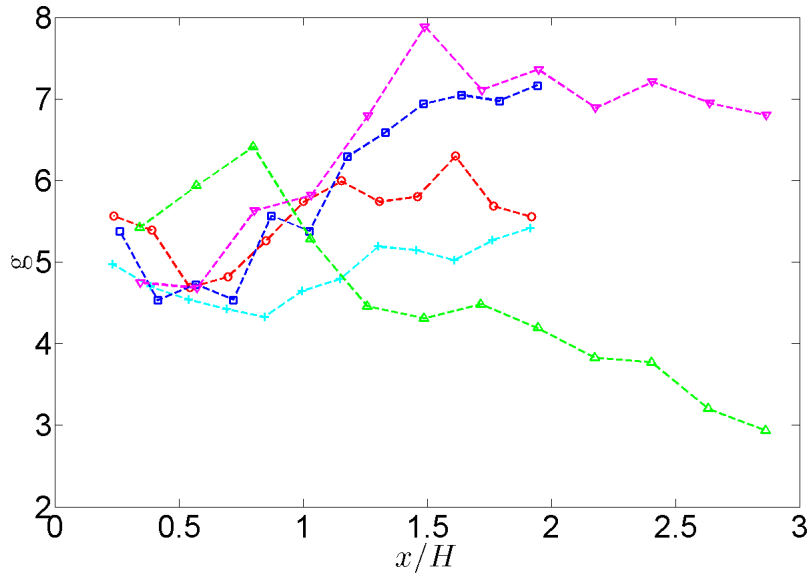


(a) Position normalized by building height.

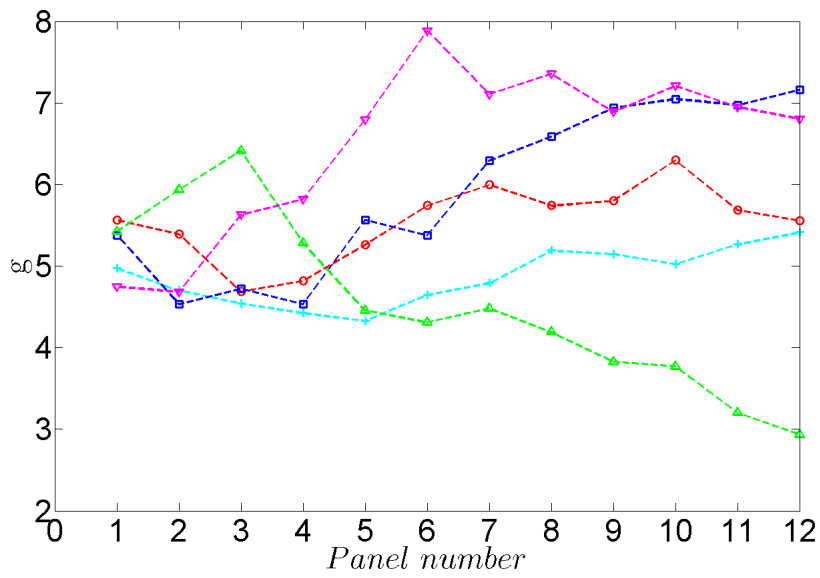


(b) Position normalized by panel number, numbering from leading edge.

Figure 4.1: Centreline peak uplift net pressure coefficients. Symbols: +, bare roof; \square , 2° north; \circ , 2° south; ∇ , 20° north; \triangle , 20° south.



(a) Position normalized by building height.



(b) Position normalized by panel number, numbering from leading edge.

Figure 4.2: Centreline peak factors. Symbols: +, bare roof; □, 2° north; ○, 2° south; ▽, 20° north; △, 20° south.

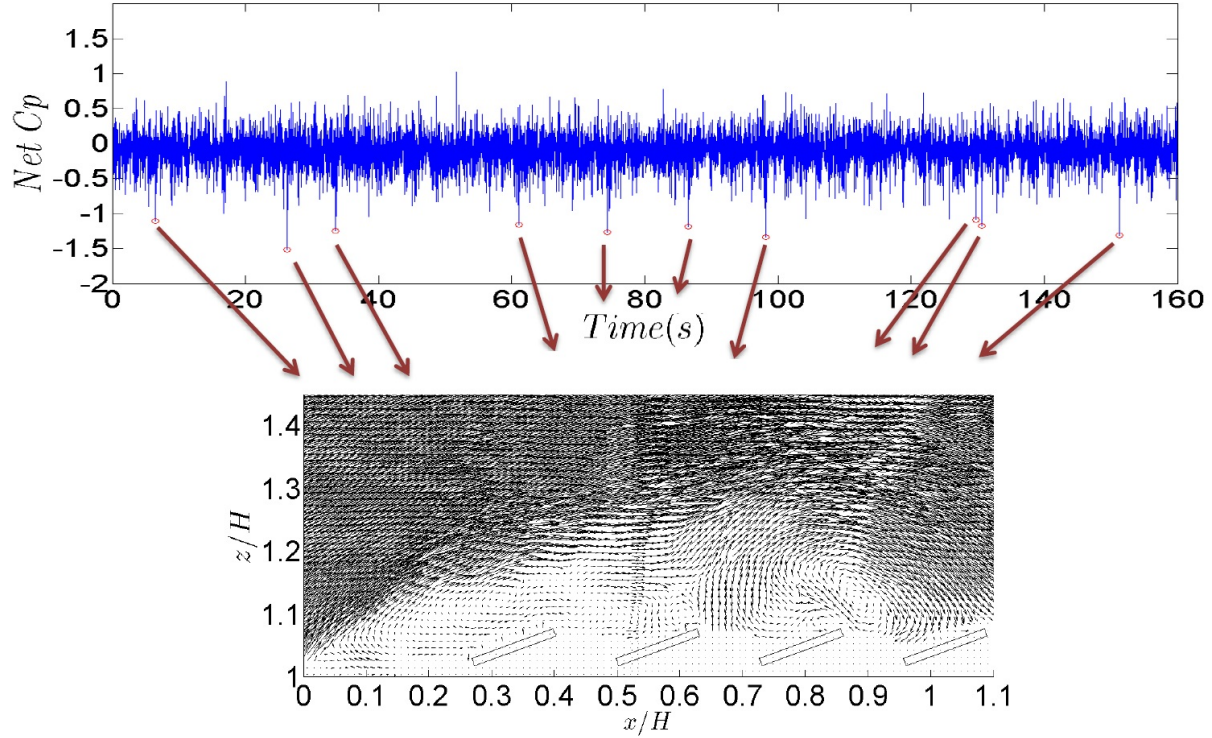


Figure 4.3: Schematic illustrating identification of peak uplift events and construction of peak ensemble averages. Upper figure is net pressure coefficient time history, lower figure is peak ensemble velocity field.

the pressures and velocity field, according to following formula,

$$\eta_{ensm} = \frac{1}{N} \sum_{n=1}^N \eta_{i^{th}peak}, \quad (4.2)$$

where η is either velocity at a point or a pressure coefficient, and $N = 10$. This process is illustrated for the peak ensemble velocity field associated with peak uplifts on the 3rd panel in Figure 4.3.

4.2.1 Roof of low-rise building

The streamlines of the ensemble average velocity fields, conditioned on the peak uplift for the first four imaginary panels on the roof are shown in Figure 4.4. From these figures it is clear

that the peak uplift events on the bare roof are strongly associated with the large-scale building generated vortex. In fact the position of the vortex core during the uplift events on each of the imaginary panels is located almost exactly above the centre of the imaginary panel which is experiencing the peak. For reference, the location of the first four imaginary panels on the building roof are $x/H = 0.23, 0.39, 0.54,$ and 0.69 respectively. It is the low pressure associated with the vortex core passing over the imaginary panels which is driving these uplift events. The peak ensemble average pressure distributions for the the first four imaginary panels are shown in Figure 4.5; the plots also include the mean surface pressure distribution for reference. The pressure signature of the vortex associated with the peak uplifts is a localized region of extremely low pressure. Prior to the location of the minimum pressure there is also a region of uniform low pressure which extends from the peak region to the leading edge of the roof, thus growing in size as the location peak uplift moves downstream. The low pressure region is followed by a rapid relaxation towards the mean pressure. As shown in Figure 4.1a, the strength of the net uplift also decreases the further the imaginary panel is from the leading edge.

4.2.2 2° Tilt angle array: South wind

The streamlines of the ensemble average velocity fields conditioned on the peak uplift for the first four panels of the 2° tilt angle array for a south wind are shown in Figure 4.6. As with the peak ensemble flow fields for the bare roof it is clear that the peak uplift events for the 2° system under a south wind are associated with the large-scale building generated vortex. This vortex is once again concentrated in a region very close to the surface of the panels. While the position of the vortex core for the peak uplift events on the bare roof was located directly above the panel experiencing the peak uplift, the location of the vortex associated with the peak uplifts for the 2° tilt angle/south wind combination was found to be shifted upstream of this panel; we will refer to this as the ‘peak panel’. The location of the vortex cores associated with the peak uplift events on the first four panels are $x/H \approx 0.35, 0.5, 0.65,$ and 0.80 . For

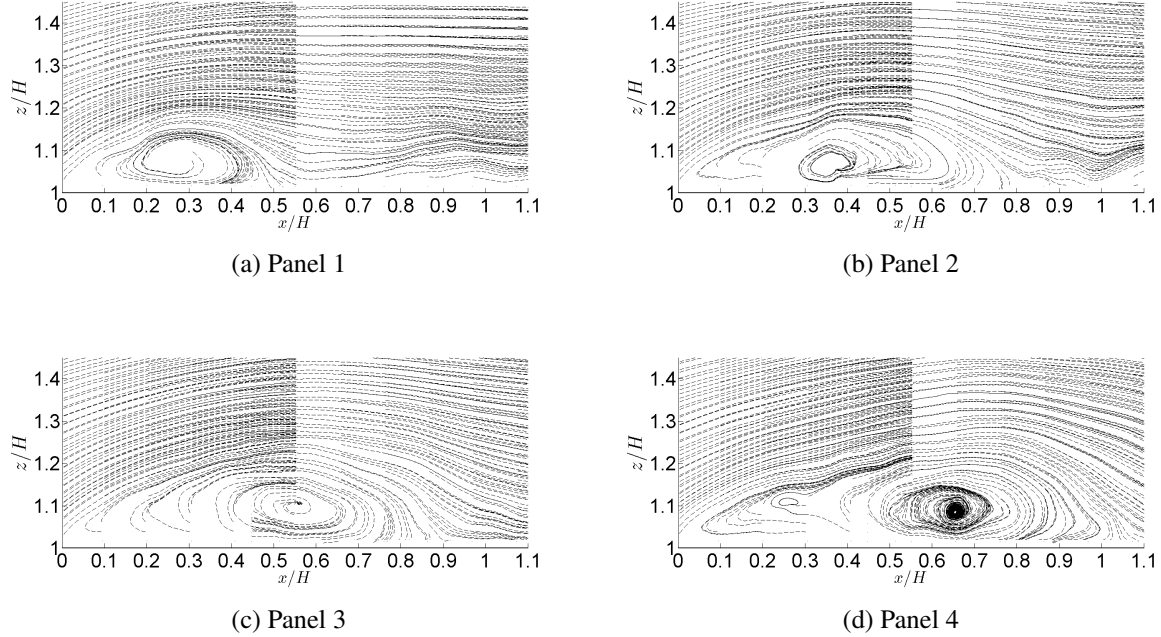


Figure 4.4: Ensemble averaged streamlines for peak uplifts on imaginary panels on the roof of the low-rise building for north/south winds.

reference, the location centre of the first four panels on the building roof are $x/H = 0.24, 0.39, 0.54, \text{ and } 0.70$, respectively. Thus the vortex core is approximately $0.11 x/H$ upstream of the centre of the panel which is experiencing the peak uplift event.

The reason for this shift becomes clear if we more closely examine the velocity field around the panels. Figure 4.7 shows the vector field of the fluctuating component $u'_{i,ensm} = u_{i,ensm} - \overline{U}_i$, of the peak ensemble average velocity fields. From the velocity fields we can see that there is a region of strong downwash due to the clockwise rotation of the vortex usually located around 1-2 panels upstream of the panel experiencing a peak combined with an upwash directly above the peak panel. This local flow around the panel also contributes to the net load in addition to the suction due to the vortex itself, which is likely largely equalized across the panel. Thus the position of the vortex is a factor of not only the vortex core suction but also the associated flow field. An examination of the peak ensemble average pressure fields, shown in Figure 4.8, further illuminates the aerodynamic mechanisms which result in peak uplift events. As was the case for the mean pressures, the large suctions observed for the bare roof are largely equalized

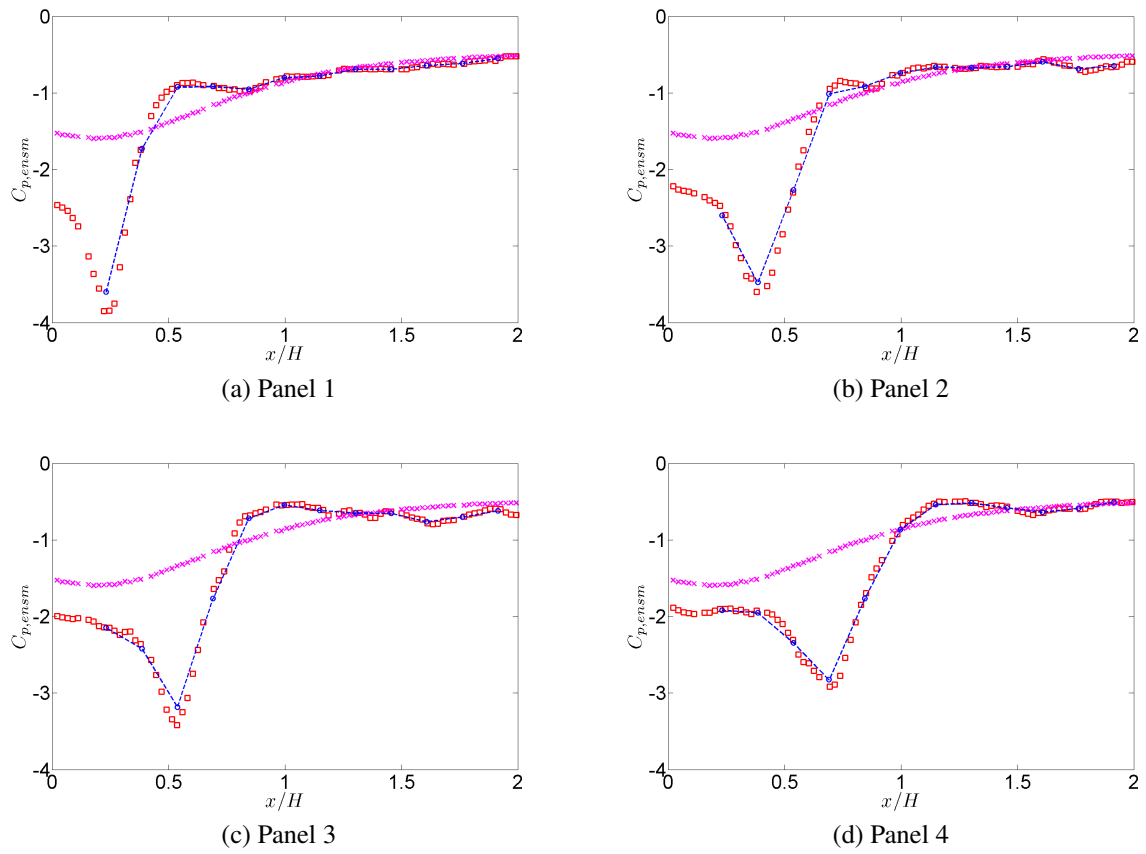


Figure 4.5: Ensemble averaged pressure distributions for peak uplifts on imaginary panels on the roof of the low-rise building for north/south winds. Symbols: \square , Point $C_{p,ensm}$; \circ , panel net $C_{p,ensm}$; \times , mean point $\overline{C_p}$.

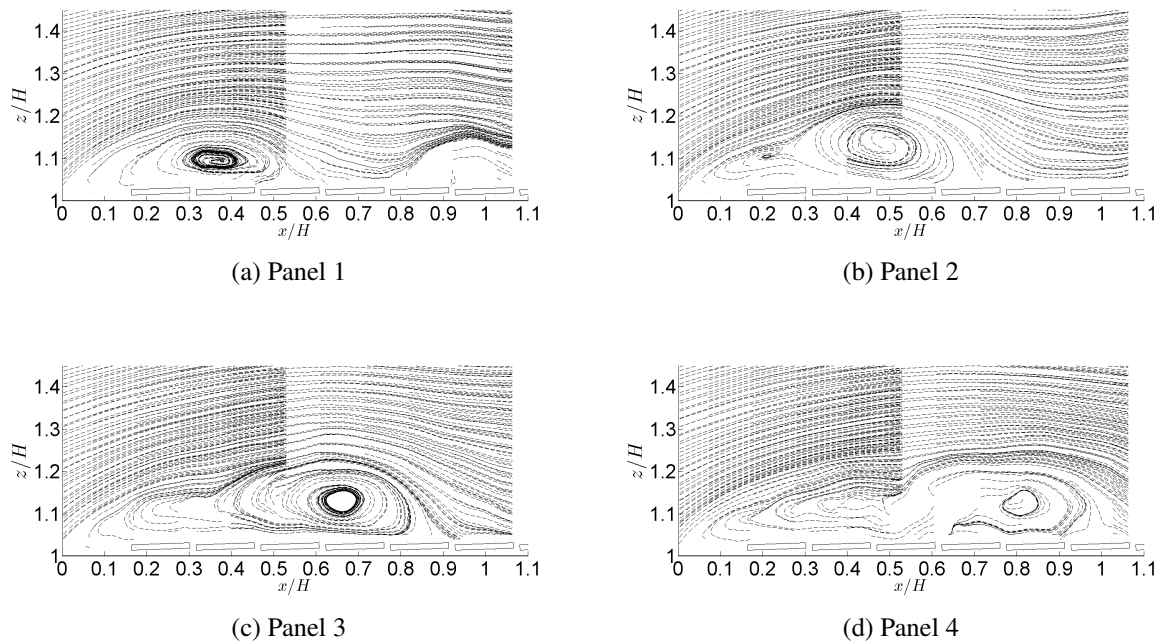


Figure 4.6: Ensemble averaged streamlines for peak uplifts on panels on 2° tilt angle array under a south wind.

across the panel such that the peak net uplifts are significantly smaller than those on the bare roof. However, local pressure gradients across the panel also affect the net loads. The peak uplift pressure fields for the first four panels all show the largest suction at the upper edge of the panel experiencing the peak, suggesting local flow separations. As with the bare roof, prior to the location of the peak uplift there is also a region of relatively uniform low pressure which extends from the peak panel to the leading edge of the roof, thus growing in size as the location peak uplift moves downstream. The low pressure region is followed by a region of uniform and relatively low suction. Furthermore, in this uniform pressure region, the pressures across the upper and lower surfaces of the panels are very similar, resulting in essentially zero net loads.

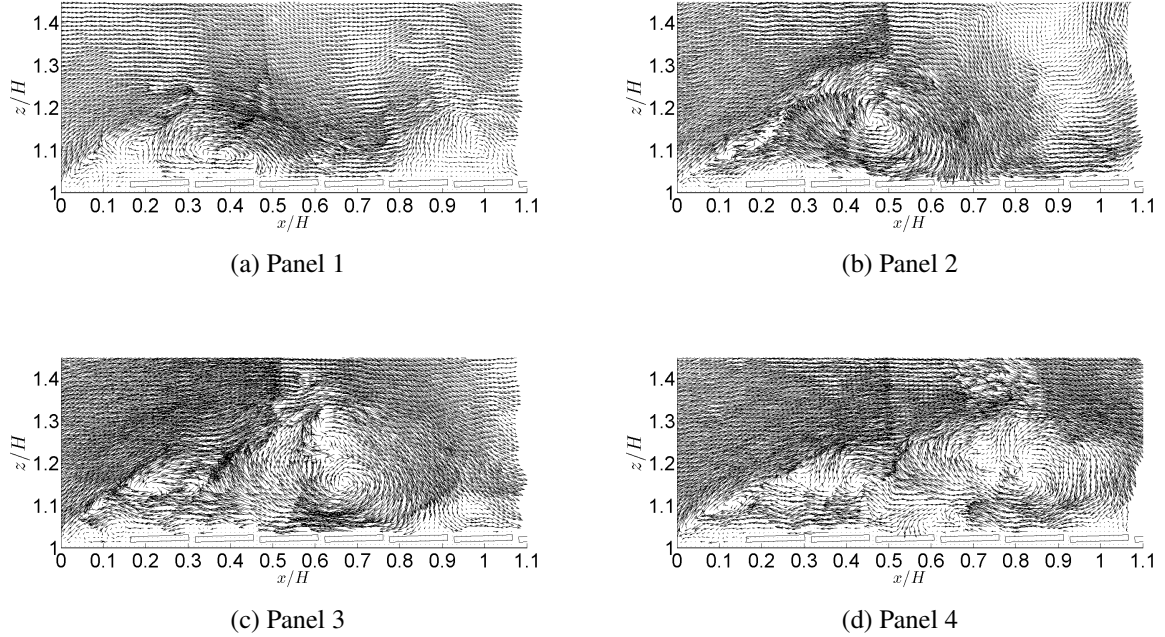


Figure 4.7: Ensemble averaged fluctuating velocity field for peak uplifts on panels on 2° tilt angle array under a south wind.

4.2.3 2° Tilt angle array: North wind

The streamlines of the ensemble average velocity fields conditioned on the peak uplift for the first four panels of the 2° tilt angle array under a south wind are shown in Figure 4.9. While this wind direction does not result in the largest uplifts for panels located within the separation bubble, the results do provide an interesting comparison to the south wind uplift mechanisms. What we observe is that, once again, there is a large scale vortex located very close to the array and slightly upstream of the peak panel. The location of the vortex cores associated with the peak uplift events on the first four panels are $x/H \approx 0.35, 0.55, 0.75,$ and 0.80 . For reference, the location of the centre of the first four panels on the building roof are $x/H = 0.26, 0.41, 0.57,$ and 0.72 , respectively. Thus, the vortex core is approximately $0.12 x/H$ upstream of the centre of the panel which is experiencing the peak uplift event. Despite the change in the orientation of the panels, the location of the vortex core relative to the peak panel is very similar to what was observed for the south wind. If we refer to the fluctuating vector plots shown in Figure

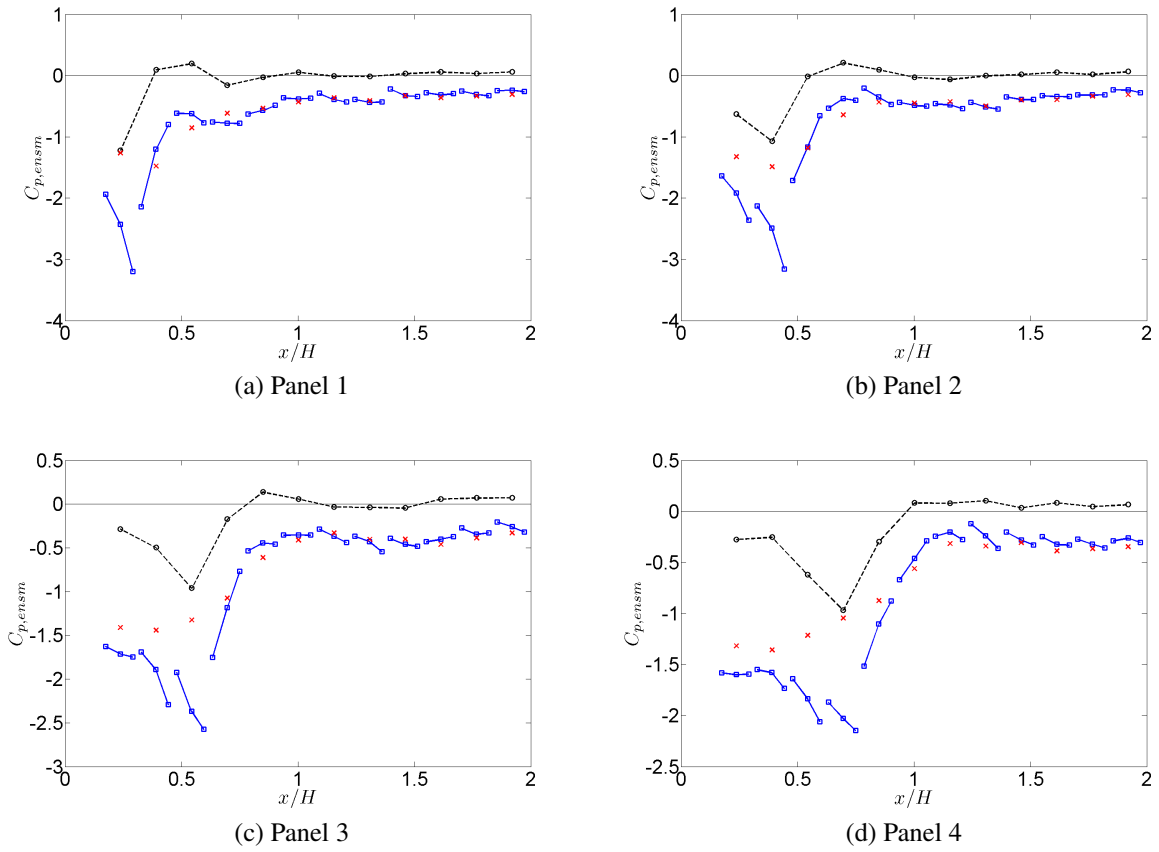


Figure 4.8: Ensemble averaged pressure distributions for peak uplifts on 2° tilt angle array under a south wind. Symbols: \circ , Net $C_{p,ensm}$; \square , upper surface $C_{p,ensm}$; \times , lower surface $C_{p,ensm}$.

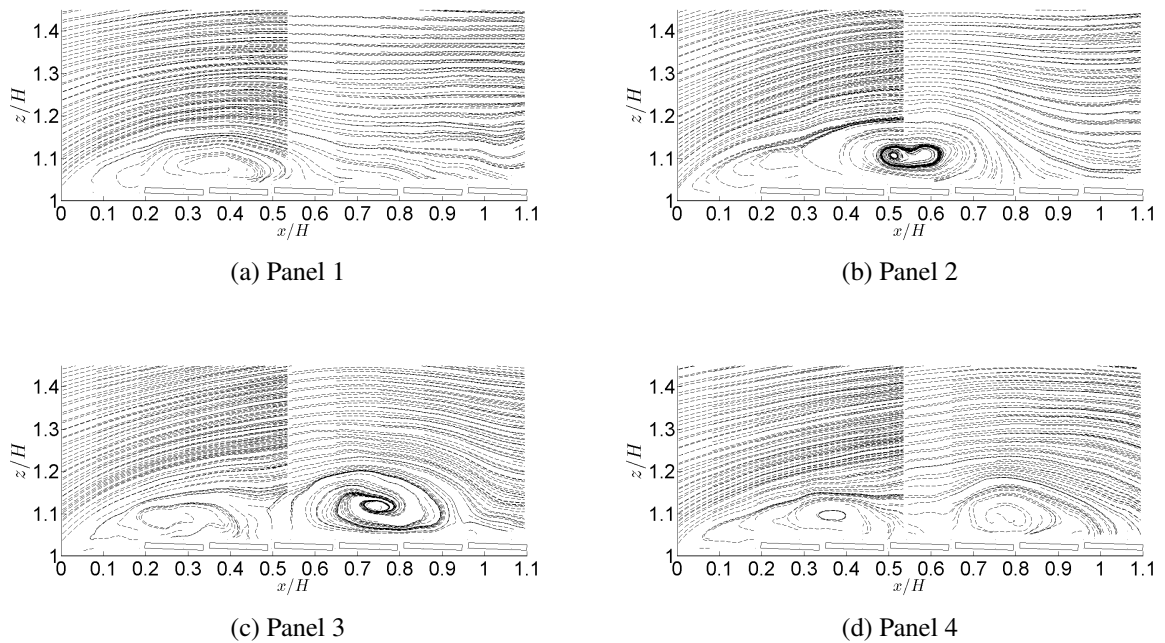


Figure 4.9: Ensemble averaged streamlines for peak uplifts on panels on 2° tilt angle array under a north wind.

4.10, we can again see the local flow around the panels induced by the circulation of the vortex. In a manner similar to that described for the south wind we would expect the downwash and upwash related to the circulation of the vortex to affect the net peak loads. If we turn to the peak ensemble averaged pressure fields, shown in Figure 4.11, the similarity between the south and north wind directions is quite evident. While slight differences in the magnitude of the upper and lower surface pressures result in slightly larger net uplifts for the south wind, the general pressure distributions across not only the peak panel but all panels are remarkably similar. We can thus conclude that, while the local flow around the panels for the lower tilt angle system does have an influence on the magnitude of the peak uplifts on the array, the primary cause of the peak uplifts is the occurrence of a large scale building generated vortex close to and slightly upstream of the peak panel. Although this mechanism is similar to that observed for the bare roof, the net uplifts on the panels are significantly less than those experienced by the bare roof due to pressure equalization between the upper and lower surfaces of the panels.

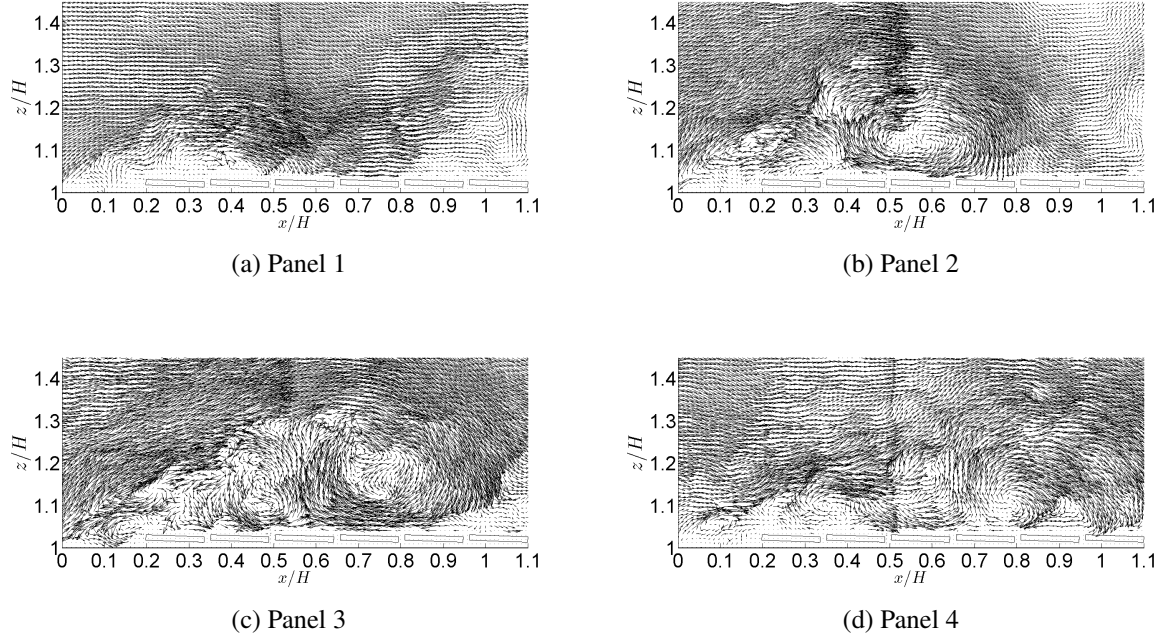


Figure 4.10: Ensemble averaged fluctuating velocity field for peak uplifts on panels on 2° tilt angle array under a north wind.

4.2.4 20° Tilt angle array: South wind

If we now examine the streamlines of the ensemble average velocity fields conditioned on the peak uplift for the first three panels of the 20° tilt angle array under a south wind shown in Figure 4.12, we can see that the strong vortex structures that we observed dominating the peak uplift flow fields for both the bare roof and 2° system are no longer as clearly defined. Note that the fourth panel peak uplift events were not presented since the majority of the important aerodynamic features are outside of the PIV field of view. The panels within the separation bubble restrict the size of the large-scale vortex by breaking it into several smaller recirculation regions, as we observed in the mean flow field. While the importance of the large-scale building generated vortices in driving the peak uplifts is diminished, the significance of the local flow around the panels becomes much more prominent. This is evident from the from the vector plots of the fluctuating component of the peak ensemble averaged velocities, shown in Figure 4.13. The importance of the vertical flow around the panel experiencing the peak, which was

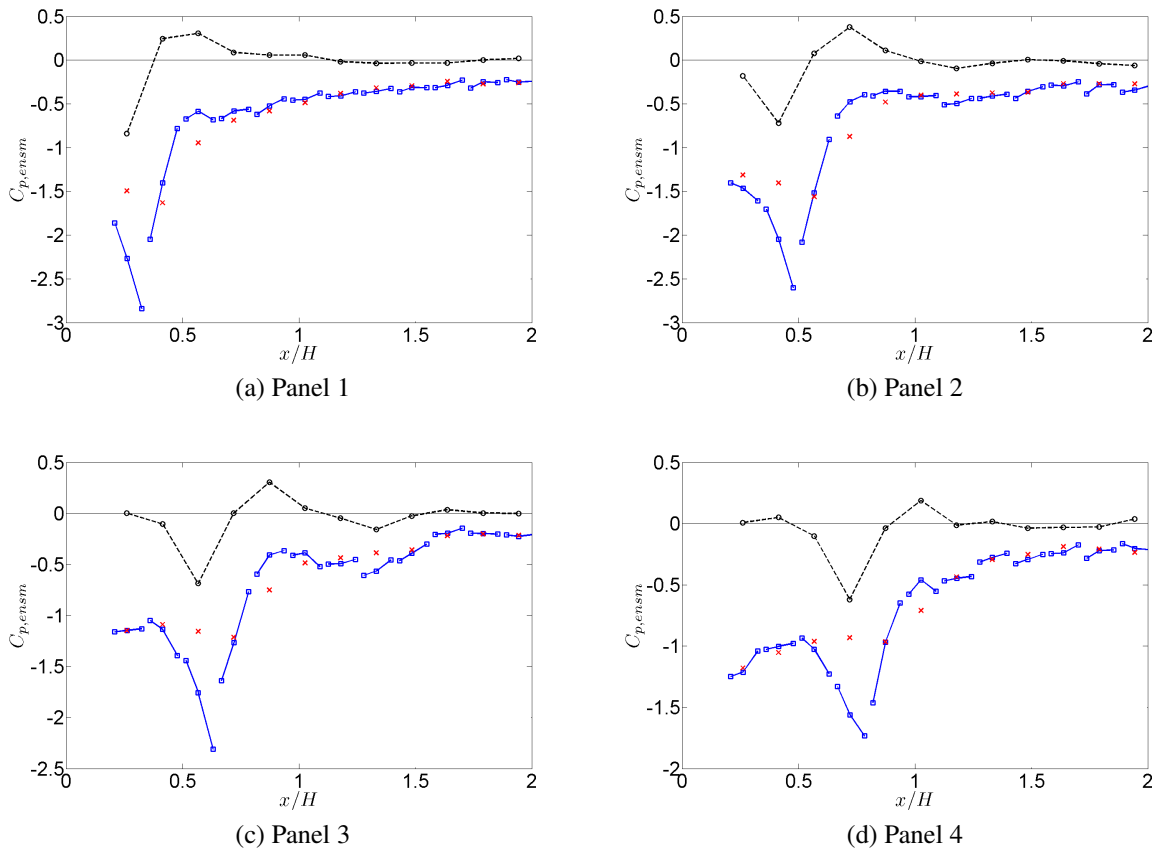


Figure 4.11: Ensemble averaged pressure distributions for peak uplifts on 2° tilt angle array under a north wind. Symbols: \circ , Net $C_{p,ensm}$; \square , upper surface $C_{p,ensm}$; \times , lower surface $C_{p,ensm}$.

somewhat evident for the 2° system, is now much more pronounced. In fact it appears that the strongest flow feature is a large downwash one panel upstream of the panel experiencing the peak. This downwash is then deflected up past the upper edge of the peak panel resulting in a strong local separation at this edge. The strength and size of this downwash region and the accompanying updraft over the upper edge of the peak panel can be clearly visualized by referring to the fraction of local maximum velocity contour plots provided in Appendix C. If we compare the location of this downwash to the streamline plots it is clear that the downwash is the result of the local reattachment of the separated shear layer. Thus, for the larger tilt angles rather than a building generated vortex driving the peak uplifts, it is the instantaneous nature of the separating-reattaching shear layer which becomes the dominant flow feature. Once again, referring to the peak ensemble average pressure fields, shown in Figure 4.17, we gain further insight into the peak uplift mechanisms. While the general trends observed for the bare roof and 2° system are maintained, that is a localized region of very low pressure, preceded by a region of uniform low pressure and superseded by rapid relaxation in suction. However, what distinguishes the pressure field from the 2° tilt angle results are the very large suctions at the upper edge of the peak panel, much larger than those observed for the 2° system under a south wind. This suction is believed to be the signature of local separations at the upper edge of the panels, which were observed in the vector fields. The pressure on the underside of the peak panel is also less negative than for the 2° tilt/south wind, flow configuration, further increasing the net suction, and indicating more significant flow on the underside of the panels.

4.2.5 20° Tilt angle array: North wind

Again, while a north wind does not result in peak uplifts within the separation bubble, we will still discuss the peak uplift aerodynamic mechanisms since they provide an interesting contrast to what was observed in the case of a south wind. Examining first the streamlines of the ensemble averaged velocity conditioned on the peak uplift shown in Figure 4.15, it is immediately clear that peaks for a north wind are driven by a different mechanism than for a

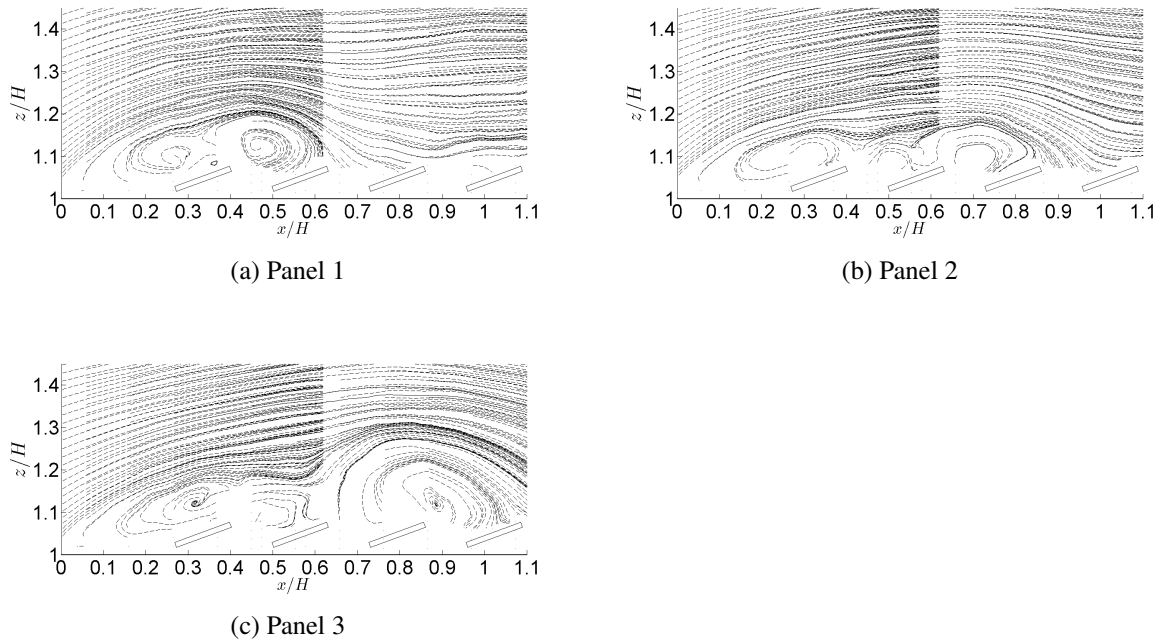


Figure 4.12: Ensemble averaged streamlines for peak uplifts on panels on 20° tilt angle array under a south wind.

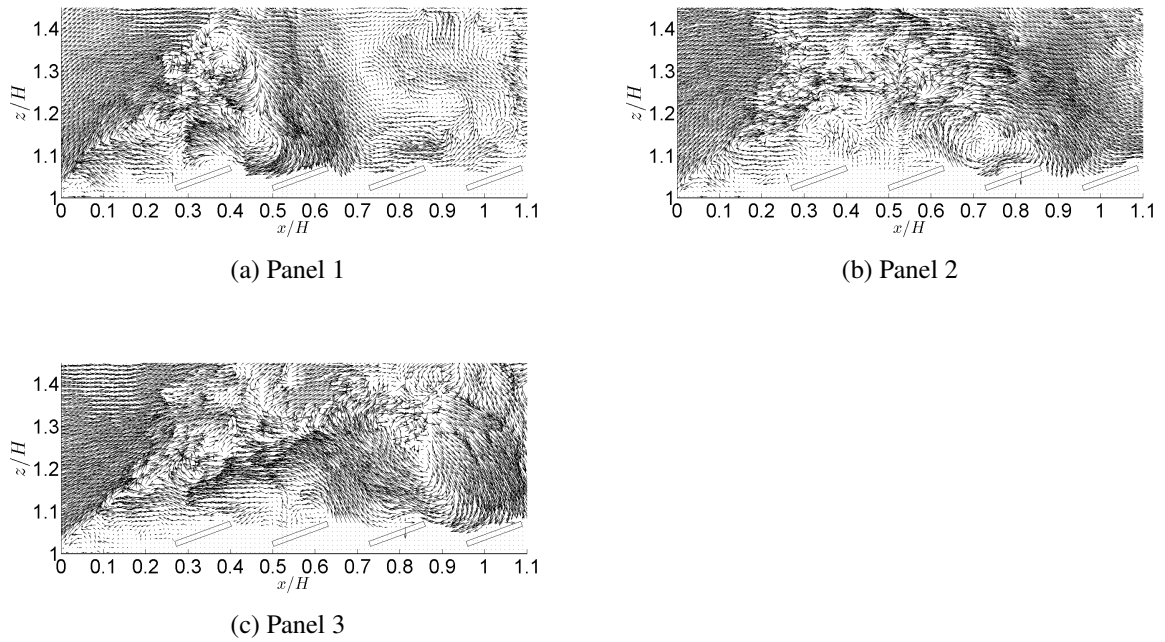
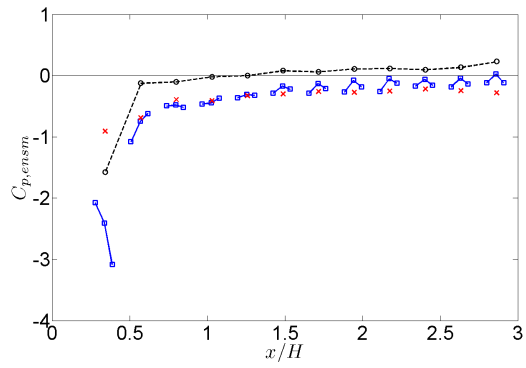
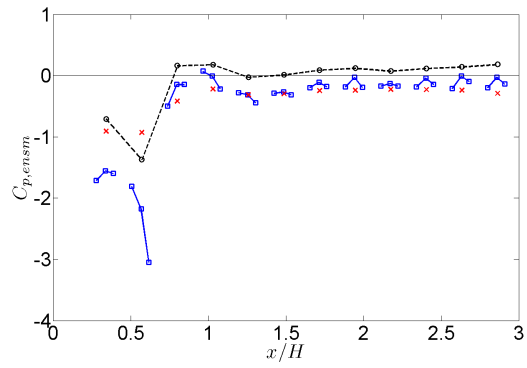


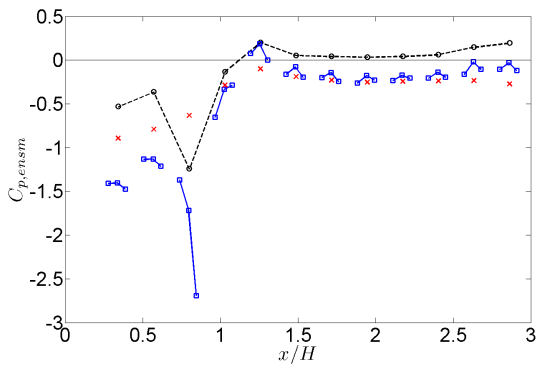
Figure 4.13: Ensemble averaged fluctuating velocity field for peak uplifts on panels on 20° tilt angle array under a south wind.



(a) Panel 1



(b) Panel 2



(c) Panel 3

Figure 4.14: Ensemble averaged pressure distributions for peak uplifts on 20° tilt angle array under a south wind. Symbols: \circ , Net $C_{p,ensm}$; \square , upper surface $C_{p,ensm}$; \times , lower surface $C_{p,ensm}$.

south wind. The structure of the leading edge flow during peak uplift is characterized by a thin separation bubble with no obvious large scale vortex structures. What we do observe, better shown by the fluctuating component of the peak ensemble averaged velocities, shown in Figure 4.16, is localized streamwise gusts around the panels which are experiencing the peak uplifts. This gust is, again, associated with the instantaneous reattachment of the separated shear layer. However, in contrast to the south wind direction for the 20° system, the peak uplift is driven by a large streamwise gust as opposed to a vertical gust. The fraction of local maximum velocity contour plots shown in Appendix C, clearly highlight the difference in the nature of streamwise gusts associated with the peak uplifts between the 20°/north wind case and other tilt angle/wind direction configurations. The 20° north wind peak uplift events are associated with streamwise gusts located very close to the surface of the roof and around the panel experiencing the peak; streamwise gusts are also present during the peaks events for the other configurations, though these gusts are generally much higher above the roof surface. The peak ensemble averaged pressure distributions for the 20° north wind peak uplifts shown in Figure 4.17 do not maintain any of the trends we observed for the previous configurations. The peak pressure distributions on the upper surface of the of the peak panels are characterized by extremely large spatial gradients, with the largest suction occurring at the panels upper edge. This large suction at the upper edge again suggests strong local flow separations. There is also a large difference between the upper and lower surface pressures which further increases the net uplifts, as the underside suction are generally quite small; in fact the underside pressure for the fourth panel peak uplift is positive.

4.3 Discussion on the peak uplift mechanisms

We have examined the aerodynamic mechanisms that are associated with the peak uplift events near the leading edge, on a low-rise building's roof and a roof-mounted PV array with two different tilt angles. The mechanisms resulting in peak uplifts on the bare roof are clearly

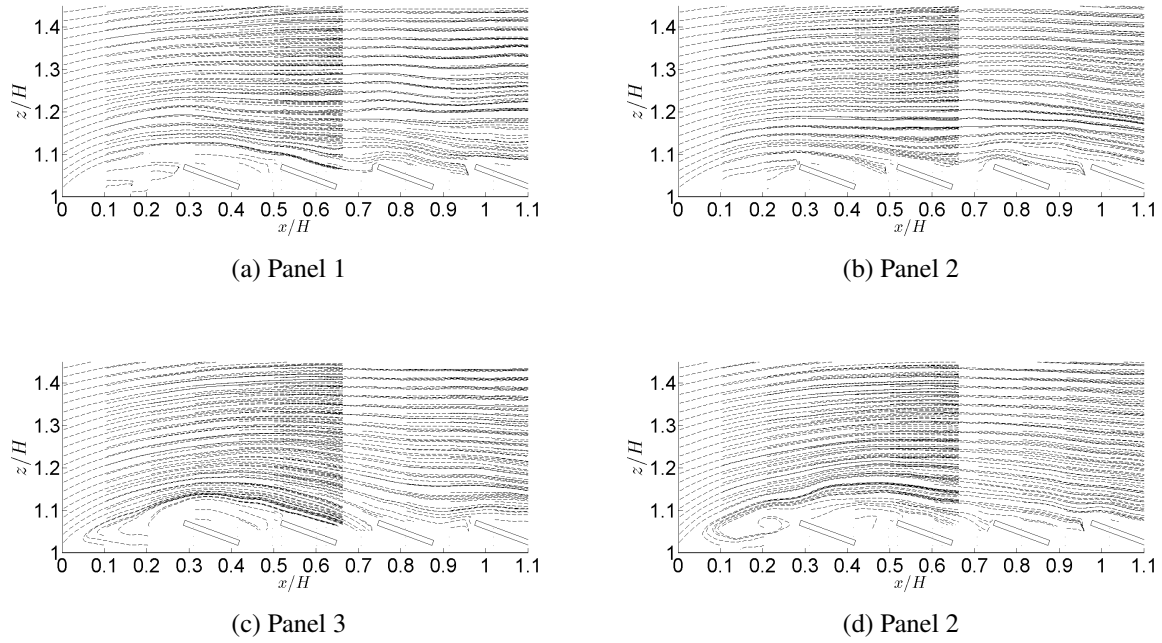


Figure 4.15: Ensemble averaged streamlines for peak uplifts on panels on 20° tilt angle array under a north wind.

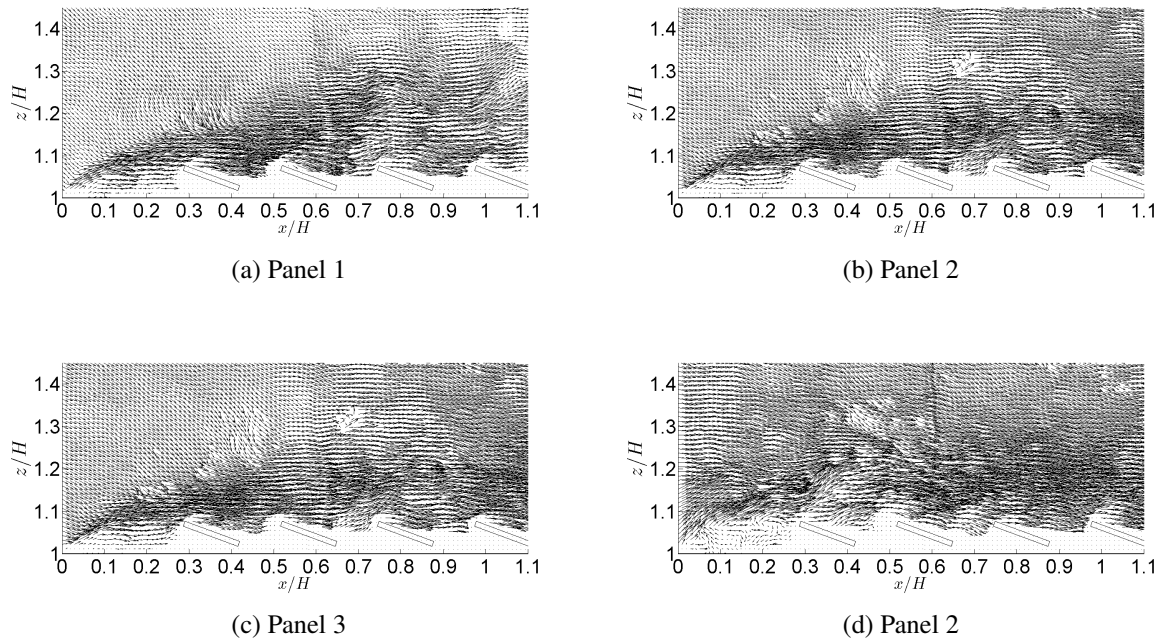


Figure 4.16: Ensemble averaged fluctuating velocity field for peak uplifts on panels on 20° tilt angle array under a north wind.

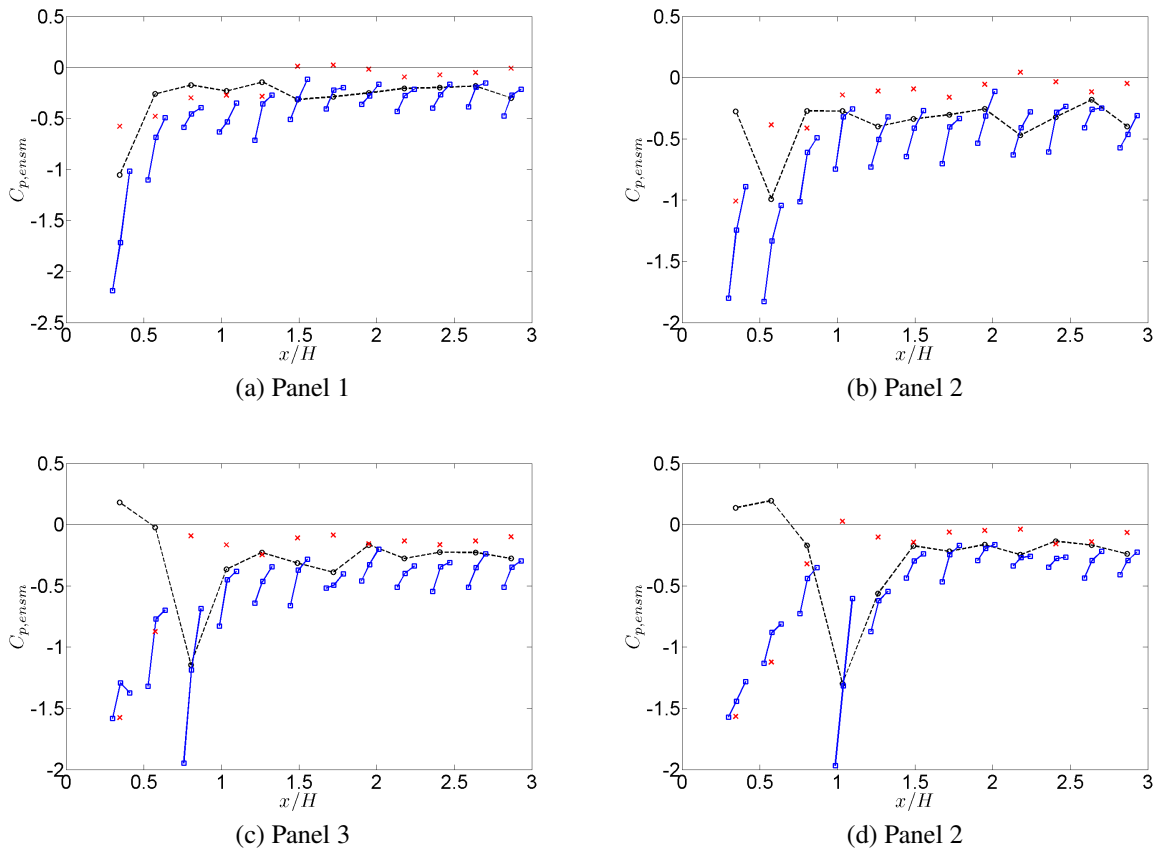


Figure 4.17: Ensemble averaged pressure distributions for peak uplifts on 20° tilt angle array under a north wind. Symbols: \circ , Net $C_{p,ensm}$; \square , upper surface $C_{p,ensm}$; \times , lower surface $C_{p,ensm}$.

dominated by a large-scale building generated vortex. The low pressure associated with the vortex core results in the peak uplifts on the roof, and hence the vortex core is always located directly above the area of the roof which is experiencing the peak, shown schematically in Figure 4.18a. For panels with a low tilt angle (2°) the peak uplift flow fields, for both north and south winds, are found to bear a strong resemblance to the bare roof peaks. Again the flow field is dominated by a large-scale building generated vortex. However, rather than suction associated with the vortex itself driving the uplift, the flow field induced by the vortex causes local flow around the peak panel which results in pressure gradients both across the upper surface of the peak panel and between the upper and lower surface of the panel. These pressure gradients result in net uplifts, which, while not as strong as those experienced by the bare roof, are still significant. For the 20° tilt angle panels during a south wind, the large-scale vortex structure is not well defined while the importance of the local flow around the peak panel becomes more important. The flow field which drives this local flow is established by the instantaneous reattachment of the separated shear layer 1 to 2 panels downstream of the peak panel. This impinging flow is then directed around the peak panel resulting in a strong local separation at the upper edge of the peak panel as well as significant flow around the underside of the panel (indicated by the underside pressure). We observed that the bare roof, the 2° array and the 20° array in a south wind all displayed similar trends in the point pressure distributions. However, pressure equalization reduces the net pressures for the PV panels when compared to the bare roof, while the pressure gradients across the panels results in net uplifts. So from the bare roof, through to the 2° array and to the 20° array in a south wind we see a clear progression from vortex dominated uplifts towards local flow driven uplifts. The local flows for the smaller tilt angle are established by the vortex induced flow field, while for the larger tilt angle, the instantaneous reattachment of the separated shear layer sets up the local flow. The local flow for both the 2° system and 20° /south wind case results in a “drag mechanism” acting on the peak panel, though clearly the strength of this mechanism increases for the higher tilt angle. These drag mechanisms are depicted schematically in Figures 4.18b and 4.18c, for the 2° and

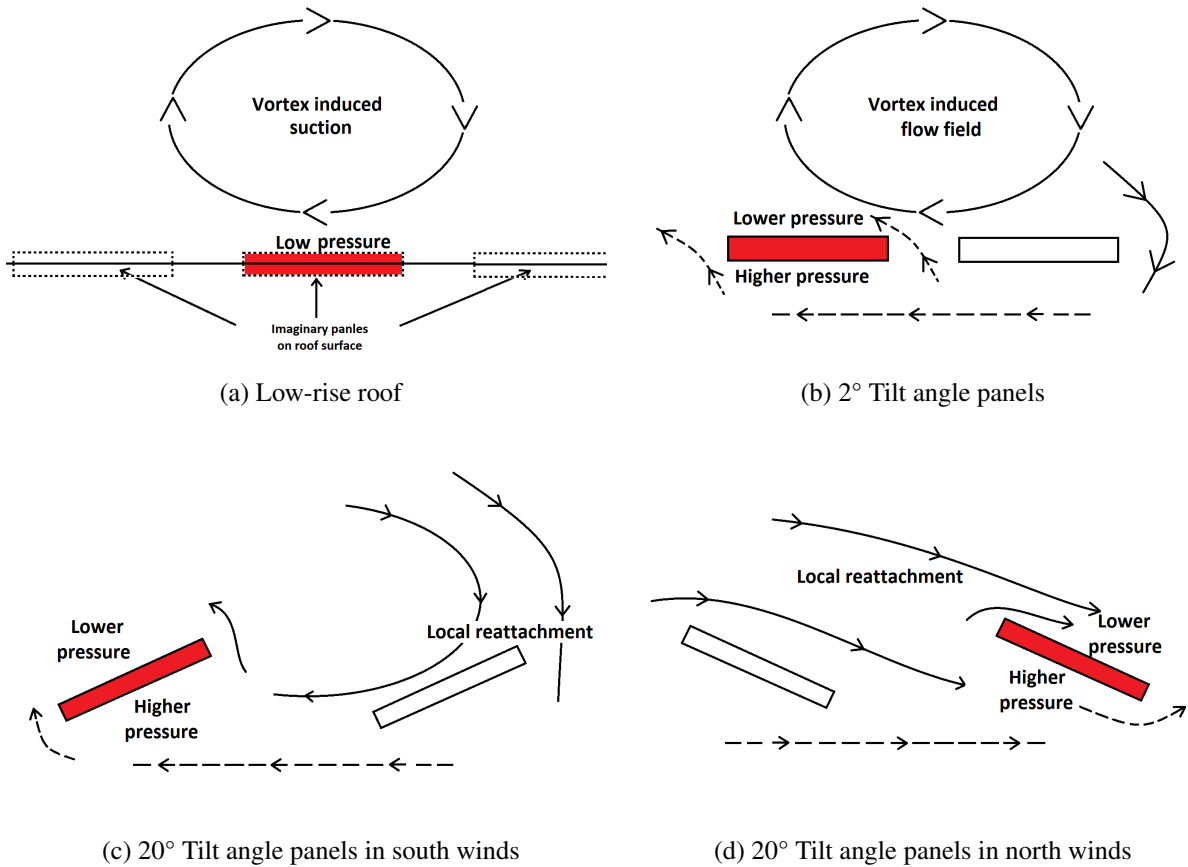


Figure 4.18: Peak uplift mechanisms for panels within the separation bubble. The peak panels are highlighted in red. Solid lines indicate flows observed flow features; dashed lines indicated hypothesized flow features.

20°/south wind configurations respectively. The aerodynamic mechanisms associated with the peak uplifts for the 20°/north wind case bear little resemblance to the previously discussed cases. In this case peak uplifts were the result of a streamwise gust associated with the local reattachment of the separated shear layer, and a very thin separation bubble. However, again this local flow field results in a drag mechanism on peak panel, described in Figure 4.18d.

An implication of the conclusion that the peak uplifts on the panels are largely a result of a drag mechanism, is that the pressure resolution on the underside of the panels may not be adequate to fully capture the details of the surface pressures. As described in Figure 4.18, the underside of the panel during peak uplifts faces the local impinging flow, which causes the drag on the panel. Fage and Johansen [35] showed that, for a 2-dimensional flat plate, the mean

pressure distributions on the front face at various angles of attack exhibit significant gradients, while the pressure distributions on the rear surface are generally more uniform. In the design of the PV array models more pressure taps were allocated to the panel topsides [16] as prior work on roof pavers showed less significant pressure gradients on the paver undersides [36]. While it is not expected that the conclusions regarding the peak uplift mechanisms would differ with better pressure resolution, improved resolution would certainly provide more insight into the flow underneath the panels. This merits further investigation.

Chapter 5

Conclusions

A detailed investigation of the wind field around PV arrays mounted on large flat-roofs has been undertaken. The published work on the subject of PV array-wind interaction is primarily focused on the aerodynamic loads, with much less attention payed to the mechanisms which drive these loads. As such, the goal of this study is to elucidate the aerodynamics of such systems, particularly the aerodynamic mechanisms which result in peak uplifts. To achieve this objective a series of experiments where conducted using synchronized TR-PIV and pressure measurements. The present work is focused on the leading edge flow for north and south winds; two panel tilt angles were examined: 2° and 20° .

The mean flow is not significantly altered above the array, as compared to the flow over an equivalent building without any panels installed on the roof. The 2° array tends to shorten the mean reattachment length slightly, as compared to the bare roof. The mean reattachment of the separated shear layer on the 20° array is significantly perturbed by local separations and reattachments over the array. However, reattachment occurs at approximately the same location as the bare roof, for both north and south winds. Furthermore, the mean velocity profiles, in both the streamwise and vertical directions, above the arrays are unaffected by the presence of the panels. What all this suggests is that for north and south winds the mean separated and reattached zones on the buildings are relatively consistent with or without an array installed on

the roof. These zones have important implications for the wind loads as some of the largest loads on the array occur on panels which are within the separation bubble, during south winds. The similarity in the mean flow is also manifested in the point pressures. The pressures on the upper-sides on the panels, in all wind direction and tilt angle configurations, are remarkably similar. Furthermore, the upper-side pressures follow the same trend as the point pressures on the bare roof surface, though the magnitudes are slightly less negative. As, shown by several prior studies ([15], [16], [14]), these large suction are largely equalized across the panel's upper and lower surfaces and thus the mean pressures on the array are much less than those on the equivalent bare roof.

In contrast to the mean flow, the array has a significant affect on the turbulence above and around the panels, as characterized by the Reynolds stresses. When panels are installed on the roof, both Reynolds normal (i.e., turbulence levels) and Reynolds shear stresses are markedly reduced when compared to the flow over the bare roof. This is a surprising result since it was originally expected, as surmised by Kopp *et al.* [16], that turbulence levels would be increased by the panels. This suggests that the panels are impeding some mechanism which drives the development of the turbulent structure within the separation bubble. This was not investigated further as it was outside of the scope of the present study, however, it is certainly a potential subject which would warrant further study. The pressure fluctuations on the panels' upper-sides are also lower than those on the bare roof, within the separation bubble. However, we do observe that the pressure fluctuations rise above the bare roof levels towards the end of the array. Thus, array generated turbulence begins to manifest itself in the surface pressure fluctuations, towards the end of the array.

The primary focus of the present study was the investigation of the aerodynamic mechanisms which result in the peak uplifts. The mechanisms resulting for peak uplifts on a bare roof are clearly dominated by a large-scale building generated vortex, and it is the low pressure associated with this vortex the drives the uplift directly. For a low tilt angle (2°) array the peak uplifts on the panels are again associated with large-scale building generated vortices. How-

ever, rather than only the vortex driving the uplift directly, the flow field induced by the vortex causes local flow around the panels which also contributes to the uplift. This local flow causes a drag mechanism around the peak panel. The peak uplift mechanisms for the 2° tilt angle array under both north and south winds are the same, however, different wind directions cause slightly different pressure gradients across the peak panel, resulting in slightly higher uplifts for the south wind direction. For the 20° tilt angle panels during a south wind, large-scale vortex structures are no longer well defined. However, the importance of the local flow around the peak panel becomes more prominent. The local flow field which results in peak uplifts is established by the instantaneous reattachment of the separated shear layer 1 to 2 panels downstream of the peak panel. This impinging flow is then directed around the peak panel, resulting in drag around the panel, yielding uplift. When the 20° tilt angle array is in a north wind, the flow field resulting in the peak uplifts is markedly different for the other configurations. In this case streamwise gusts, as opposed to vertical gusts, result in the peak uplifts. These gusts are driven by the local reattachment of the separated shear layer, and are associated with a thin separation bubble. This local flow field, again, results in a drag mechanism on the peak panel.

As the tilt angle of the PV array is increased we observed a progression from the importance of the vortex driven suction, which cause peak uplifts on the bare roof, towards local flow driven uplifts. For small tilt angle (2°) arrays the local flow is established by large-scale building generated vortices, while for the larger tilt angle (20°) arrays the instantaneous reattachment of the separated shear layer sets up the local flow. For the larger tilt angles, south wind peak uplifts are driven by large vertical gusts, while peaks for northern winds are the result of streamwise gusts. The local flow field which causes the peak events, whether it is driven by a vortex or reattachment, is established by the large-scale building generated flow features. The interaction of these large-scale features with the panels, in the form of drag, results in the peak uplifts.

5.1 Future Work

The present study focused on the flows over a roof-mounted PV arrays at the building's leading edge in north and south winds. Thus, a clear progression of this work would be to investigate the other critical wind directions which result in peak uplifts. North winds result in large uplifts on panels near the trailing edge of the building. The trailing edge flow would also be interesting to investigate as we observed the growing importance of array generated turbulence in the panels' surface pressures in this region. Northern-corning winds are the other critical wind direction, this wind direction results in a complex cornering vortex which then interacts with the array. This wind direction also results in largest uplifts on bare-roofs.

This study also highlighted some gaps in the literature regarding the flow over a low-rise buildings, or, surface-mounted prisms. Particularly the lack of detailed flow field measurements within the separation bubble. Finally, as already discussed, the observed reduction in turbulence within the separation bubble when a PV array is installed on the roof also raised some interesting questions regarding the development of turbulence within the separation bubble.

Bibliography

- [1] Earth Policy Institute. World solar photovoltaic production, January 2011.
- [2] CanmetENERGY Innovation and Energy Technology Sector Department of Natural Resources Canada. National survey report of photovoltaic power applications in Canada, June 2010.
- [3] Ontario Power Authority, Toronto, Canada. *Feed-in tariff program - Program overview*, 1.3.1 edition, December 2011.
- [4] American Society of Civil Engineers, Reston, Virginia. *ASCE 7-10, Minimum Design Loads for Buildings and Other Structures*, 2010.
- [5] National Research Council of Canada, Ottawa, Canada. *National Building Code of Canada*, 2005.
- [6] R. Martinuzzi and C. Tropea. The flow around surface-mounted, prismatic obstacles placed in a fully developed channel flow. *Journal of Fluids Engineering*, 115:85–92, 1993.
- [7] I.P. Castro and A.G. Robins. The flow around a surface-mounted cube in uniform and turbulent streams. *Journal of Fluid Mechanics*, 79:307–335, 1977.
- [8] D. Banks, R.N. Meroney, P.P. Sarkar, Z. Zhao, and F. Wu. Flow visualization of conical vortices on flat roofs with simultaneous surface pressure measurement. *Journal of Wind Engineering and Industrial Aerodynamics*, 84:65–85, 2000.

- [9] W.H. Melbourne. Cross-wind response of structures to wind action. In *4th International Conference on Wind Effects on Buildings and Structures*, pages 343–358, Heathrow, 1987.
- [10] P.J. Saathoff and W.H. Melbourne. The generation of peak pressures in separated / reattaching flows. *Journal of Wind Engineering and Industrial Aerodynamics*, 32:121–134, 1989.
- [11] N.J. Cherry, R. Hillier, and Latour M.P. Unsteady measurements in a separated and reattaching flow. *Journal of Fluid Mechanics*, 144:13–46, 1984.
- [12] P.J. Saathoff and W.H. Melbourne. Effect of free-stream turbulence on surface pressure fluctuations in a separation bubble. *Journal of Fluid Mechanics*, 337:1–24, 1997.
- [13] A. Radu, E. Axinte, and C. Theohari. Steady wind pressures on solar collectors on flat-roofed buildings. *Journal of Wind Engineering and Industrial Aerodynamics*, 23:249–258, 1986.
- [14] G.S Wood, R.O. Denoon, and K.C.S Kwok. Wind loads on industrial solar panel arrays and supporting roof structure. *Wind and Structures*, 4(6):481–494, 2001.
- [15] B. Bienkiewicz and M. Endo. Wind considerations for loose-laid and photovoltaic roofing systems. In *Proceedings of Structures Congress*, pages 2578–2587. ASCE, 2009.
- [16] G.A. Kopp, S. Farquhar, and M. Morrison. Aerodynamic mechanisms for wind loads on tilted, roof-mounted, solar arrays. *Journal of Wind Engineering and Industrial Aerodynamics*, 111:40–52, 2012.
- [17] C.P.W. Geurts and C.A. van Bentum. Wind loads on active roofs. Technical report, TNO Report 2006-D-R0203, Delft, Netherlands, 2006.
- [18] Nederlands Normalisatie-instituut. *NVN 7250: Solar energy systems-integration in roofs and facades - building aspects.*, July 2003.

- [19] A. Bronkhorst, J. Franke, C.P.W. Geurts, C.A. van Bentum, and F. Grepinet. Wind tunnel and CFD modelling of wind pressures on solar energy systems on flat roofs. In *The 5th International Symposium on Computational Wind Engineering (CWE2010)*, Chapel Hill, North Carolina, USA, 2010.
- [20] American Society of Civil Engineers, Reston, Virginia. *ASCE No. 49-12, Wind tunnel testing for buildings and other structures*, 2012.
- [21] Engineering Data Science Unit. Strong winds in the atmosphere boundary layer. part 1: Mean-hourly wind speeds, data item 82026. Technical report, 1982.
- [22] Engineering Data Science Unit. Strong winds in the atmosphere boundary layer. part 2: Discrete gust speeds, data item 83045. Technical report, 1983.
- [23] Engineering Data Science Unit. Characteristics of atmospheric turbulence near the ground, data item 74031. Technical report, 1974.
- [24] T.C.E. Ho, D. Surry, D. Morrish, and G.A. Kopp. The UWO contribution to the NIST aerodynamic database for wind loads on low buildings: Part 1. archiving format and basic aerodynamic data. *Journal of Wind Engineering and Industrial Aerodynamics*, 93:1–30, 2005.
- [25] P.S. Quiroga Diaz. Uncertainty analysis of surface pressure measurements on low-rise buildings. Master’s thesis, The University of Western Ontario, April 2006.
- [26] D.R. Troolin, E.K. Longmire, and W.T. Lai. Time resolved PIV analysis of flow over a NACA 0015 airfoil with gurney flap. *Experiments in Fluids*, 41(2):241–254, 2006.
- [27] Z.J. Taylor, R. Gurka, G.A. Kopp, and A. Liberzon. Long-duration time resolved PIV to study unsteady aerodynamics. *IEEE Transactions on instrumentation and measurement*, 59(12):3262–3269, 2010.

- [28] H. Huang, D. Dabiri, and M. Gharib. On errors of digital particle image velocimetry. *Measurement Science and Technology*, 8(12):1427–1440, 1997.
- [29] K.C. Kim, H.S. Ji, and S.H. Seong. Flow structure around a 3-d rectangular prism in a turbulent boundary layer. *Journal of Wind Engineering and Industrial Aerodynamics*, 91:653–669, 2003.
- [30] G.A. Kopp and P. Sarathi. Simultaneous pressure and velocity measurements on galbe roof houses. Technical Report BLWTL-2-2010, Alan G. Devenport Wind Engineering Group, Boundary Layer Wind Tunnel Laboratory, University of Western Ontario, 2010.
- [31] I.P. Castro and A. Haque. The structure of a trubulent shear layer bounding a separation region. *Journal of Fluid Mechanics*, 179:439–468, 1987.
- [32] L.M. Hudy, A.M. Naguib, and W.M. Humphreys. Wall-pressure-array measurements beneath a separating/reattaching flow region. *Physics of Fluids*, 15(3):706–717, 2003.
- [33] A. Roshko and J.C. Lau. Some observations on transition and reattachment of a free shear layer in incompressible flow. In *Proceedings of the 1965 Heat Transfer and Fluid Mechanics Institute*, 1965.
- [34] J. Lieblein. Efficient methods of extreme-value methodology, report no. nbsir 74-602. Technical report, National Bureau of Standards, Washington, DC, 1974.
- [35] A. Fage and F.C. Johansen. On the flow of air behind an inclined flat plate of infinite span. *Proceedings of the Royal Society of London. Series A, Containing Papers of a Mathematical and Physical Character*, 116(773):170–197, 1927.
- [36] B. Bienkiewicz and Y. Sun. Wind loading and resistance of loose-laid roof paver systems. *Journal of Wind Engineering and Industrial Aerodynamics*, 72:401–410, 1992.

Appendix A

Comparison of pressure results with published data

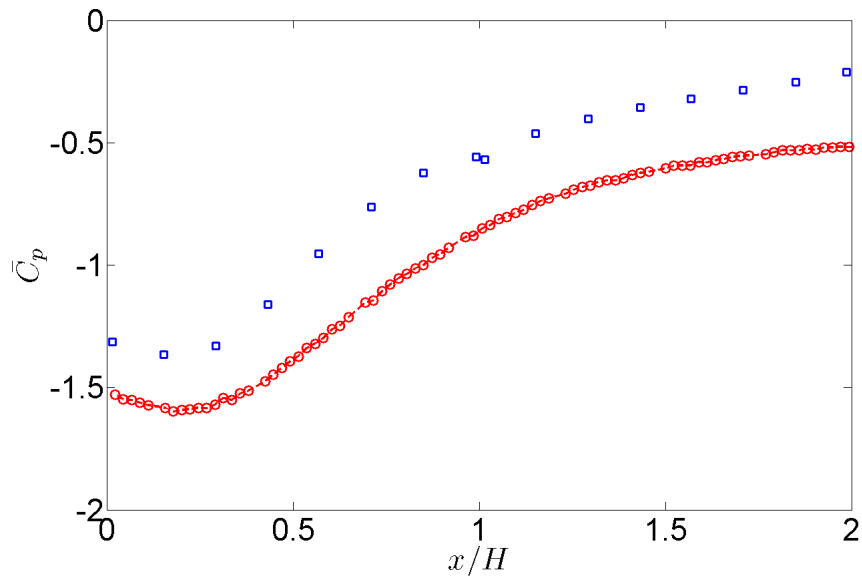


Figure A.1: Roof centreline mean pressure coefficients for a north/south wind. Symbols: \circ , present results; \square , 1:12 roof slope, 12.12m (full-scale) building, from Ho *et al.* [24].

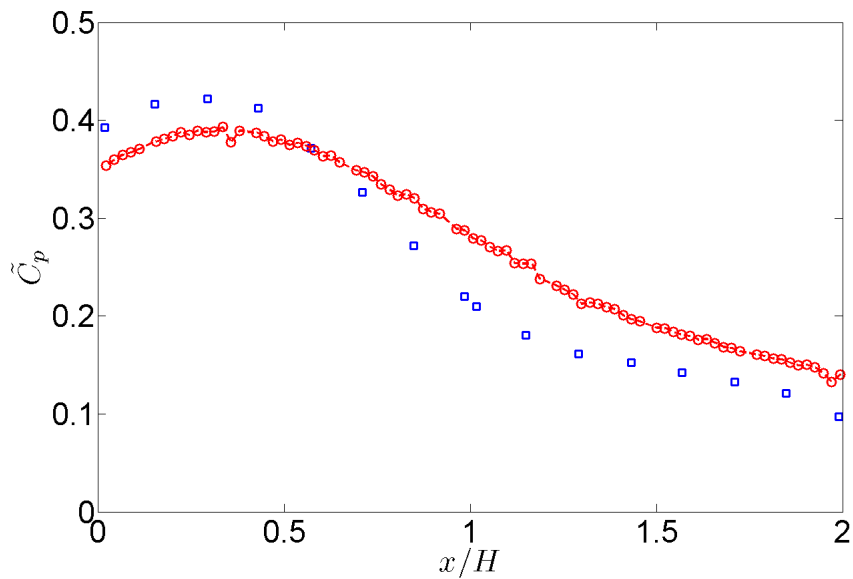


Figure A.2: Roof centreline RMS pressure coefficients for a north/south wind. Symbols: \circ , present results; \square , 1:12 roof slope, 12.12m (full-scale) building, from Ho *et al.* [24].

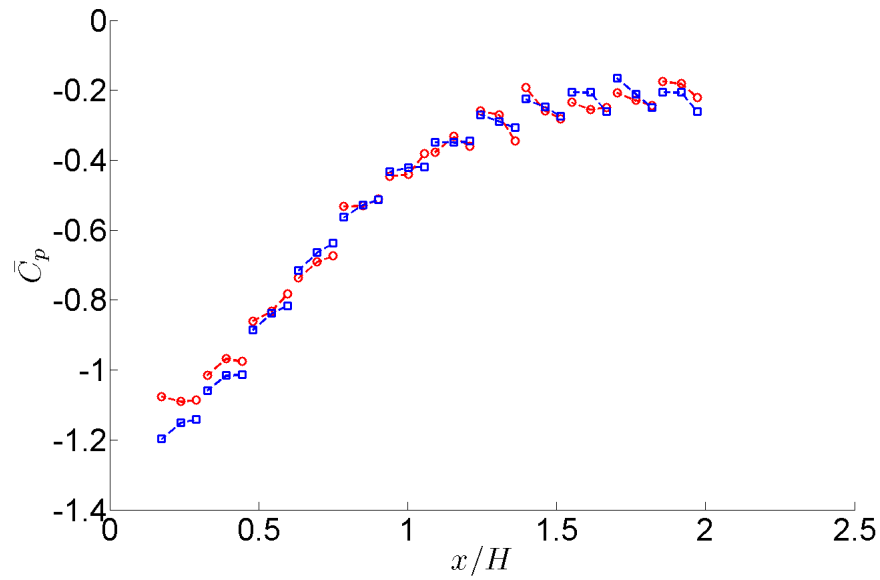


Figure A.3: Mean centreline pressure coefficients on the upper surfaces of the panels with a 2° tilt angle for a south wind. Symbols: \circ , present results; \square , Kopp *et al.* [16].

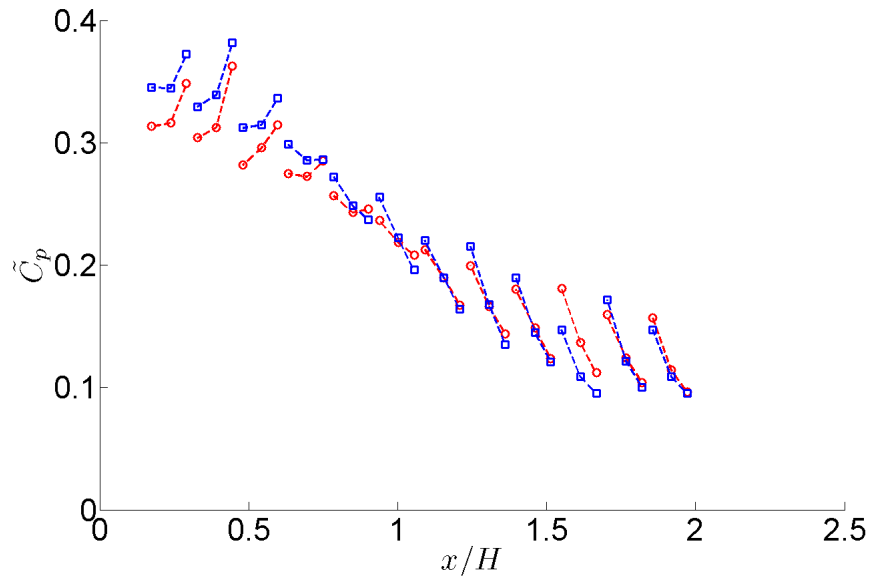


Figure A.4: RMS centreline pressure coefficients on the upper surfaces of the panels with a 2° tilt angle for a south wind. Symbols: \circ , present results; \square , Kopp *et al.* [16].

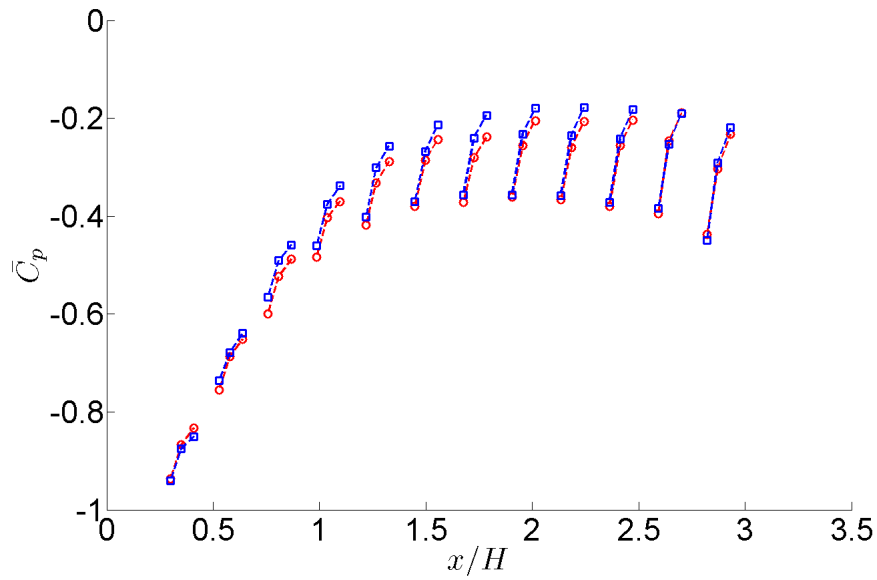


Figure A.5: Mean centreline pressure coefficients on the upper surfaces of the panels with a 20° tilt angle for a north wind. Symbols: \circ , present results; \square , Kopp *et al.* [16].

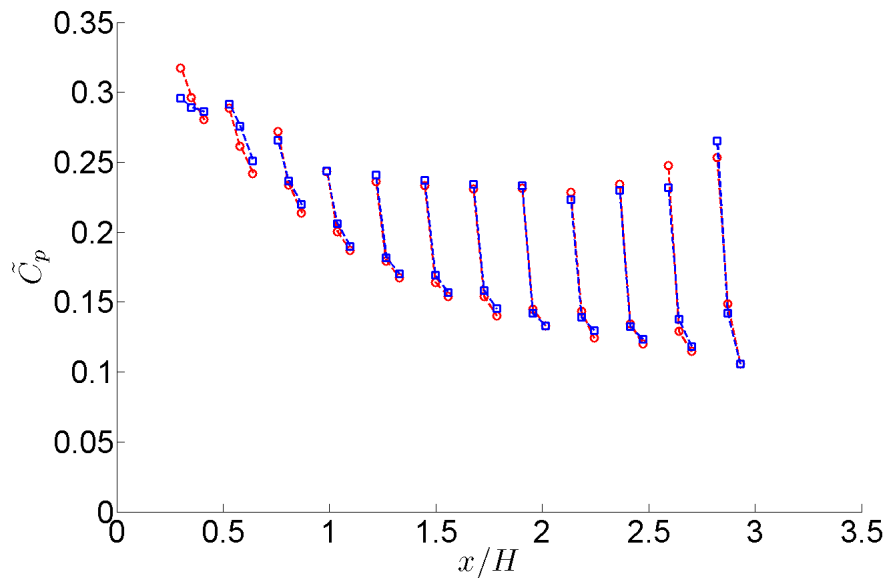


Figure A.6: RMS centreline pressure coefficients on the upper surfaces of the panels with a 20° tilt angle for a north wind. Symbols: \circ , present results; \square , Kopp *et al.* [16].

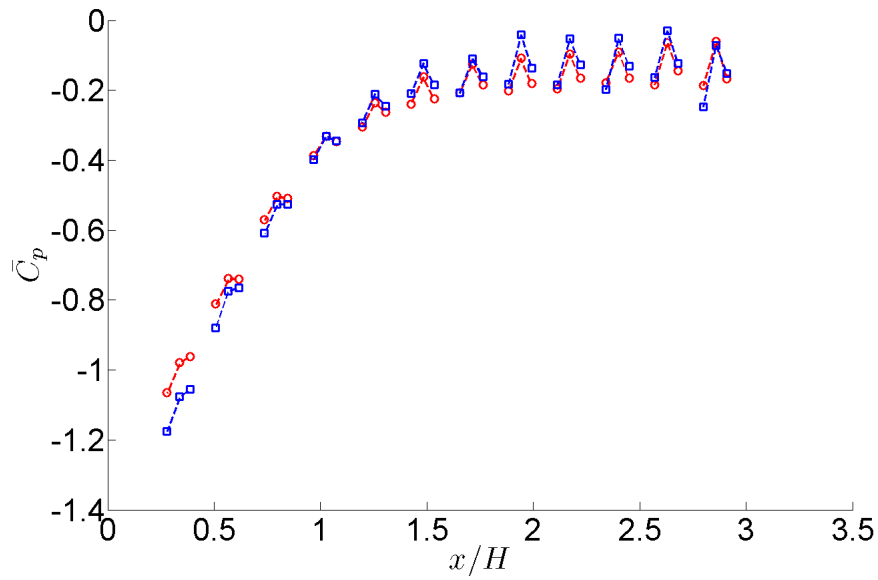


Figure A.7: Mean centreline pressure coefficients on the upper surfaces of the panels with a 20° tilt angle for a south wind. Symbols: \circ , present results; \square , Kopp *et al.* [16].

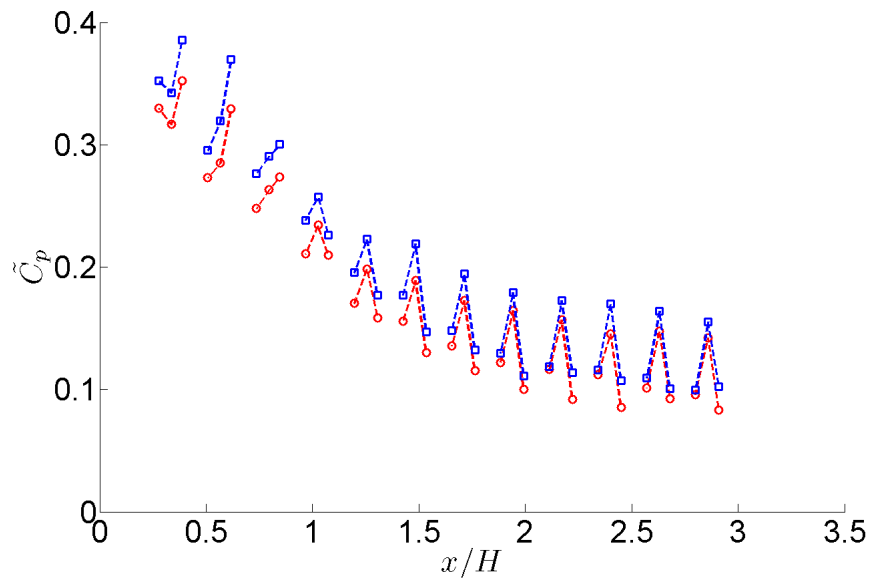


Figure A.8: RMS centreline pressure coefficients on the upper surfaces of the panels with a 20° tilt angle for a south wind. Symbols: \circ , present results; \square , Kopp *et al.* [16].

Appendix B

Combination pressure plots

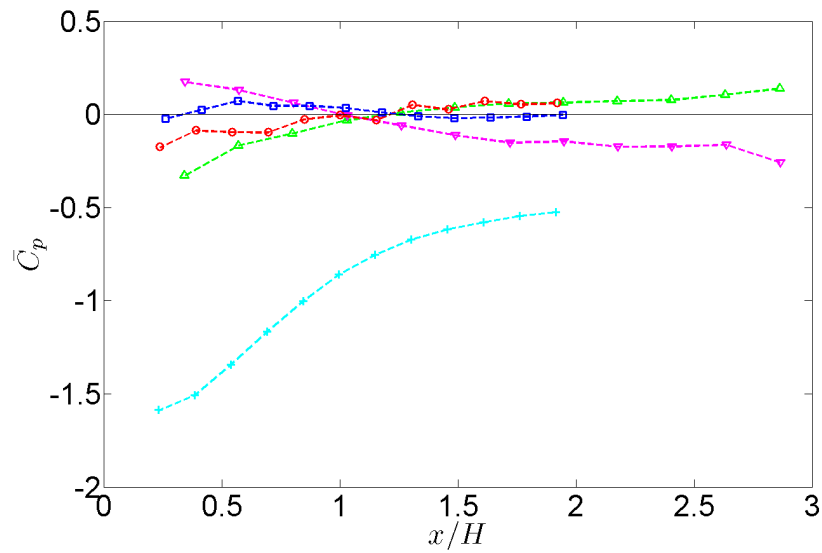


Figure B.1: Combination plot of mean net pressure coefficients. Symbols: +, bare roof; \square , 2° north; \circ , 2° south; ∇ , 20° north; \triangle , 20° south.

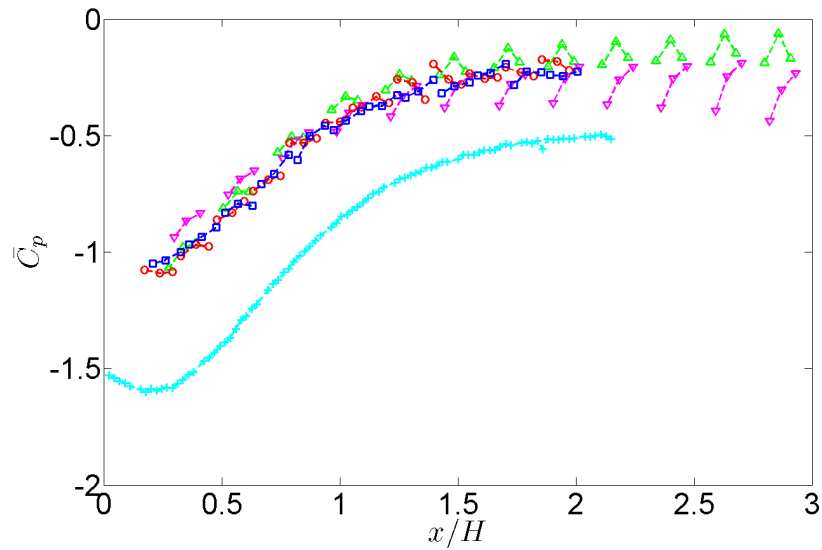


Figure B.2: Combination plot of mean point pressure coefficients. Note for PV array data are upper surface point pressures only. Symbols: +, bare roof; \square , 2° north; \circ , 2° south; ∇ , 20° north; \triangle , 20° south.

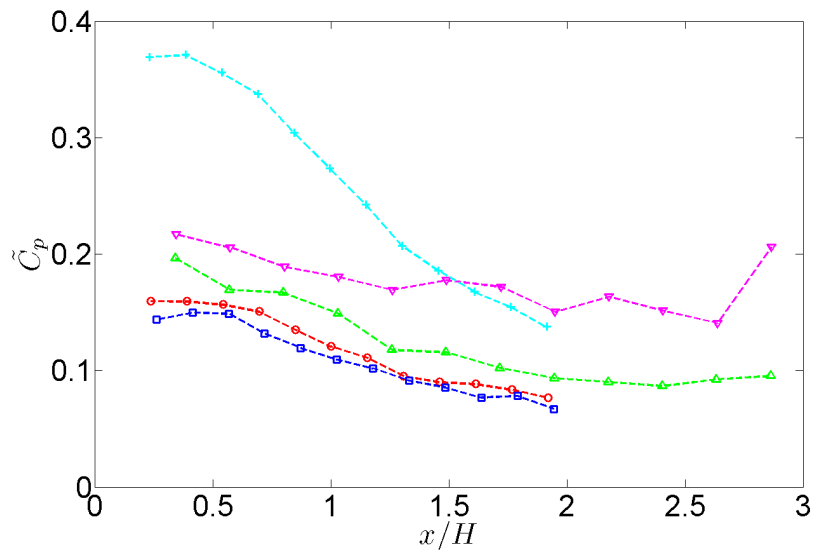


Figure B.3: Combination plot of RMS net pressure coefficients. Symbols: +, bare roof; □, 2° north; ○, 2° south; ▽, 20° north; △, 20° south.

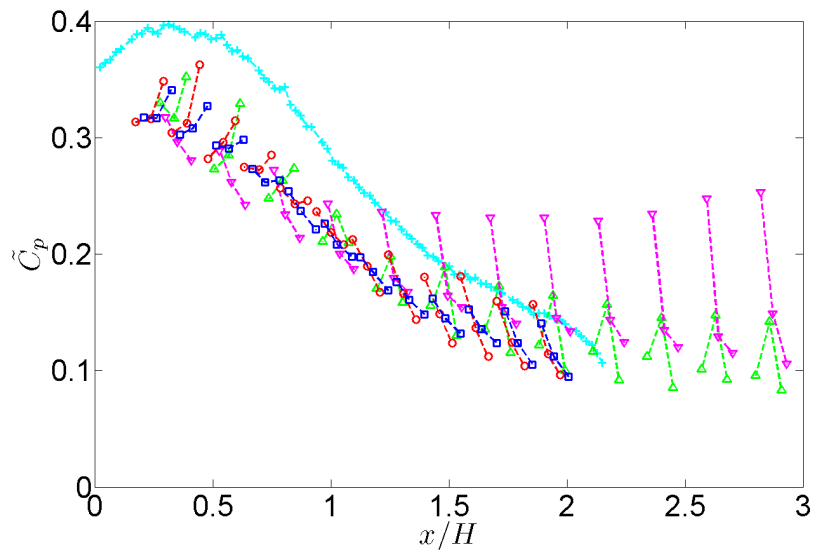


Figure B.4: Combination plot of RMS point pressure coefficients. Note for PV array data are upper surface point pressures only. Symbols: +, bare roof; □, 2° north; ○, 2° south; ▽, 20° north; △, 20° south.

Appendix C

Fraction of local maximum velocity contour plots for peak ensemble averaged velocity fields

The following are contour plots of the ensemble average velocity conditioned on the peak uplift divided by the local maximum velocity, referred to as the fraction of local maximum velocity. The contours have been overlaid with fluctuating velocity vectors, again of the ensemble average velocity fields. These plots provide an indication of how significant and large streamwise and vertical gusts are during the peak uplift event. It should be noted that as these plots represent averaged quantities the extent and magnitude of flow structures are washed by the averaging process.

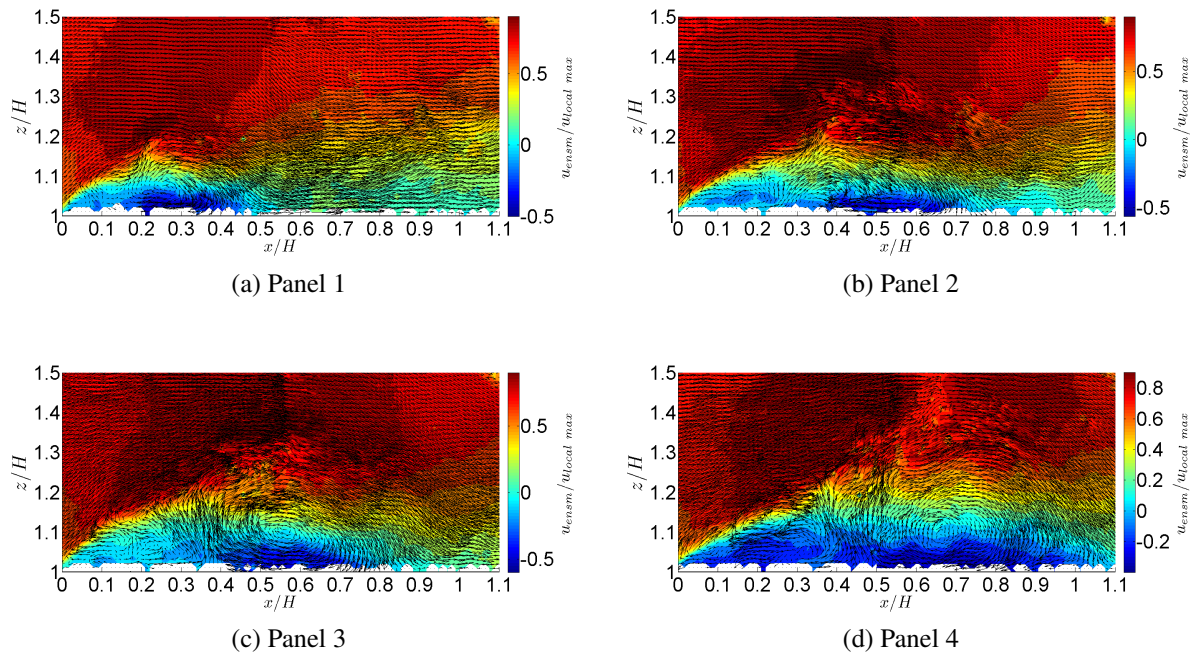


Figure C.1: Fraction of local maximum streamwise velocity contour plots of peak ensemble averaged velocity fields for uplifts on imaginary panels on bare roof under a north/south wind.

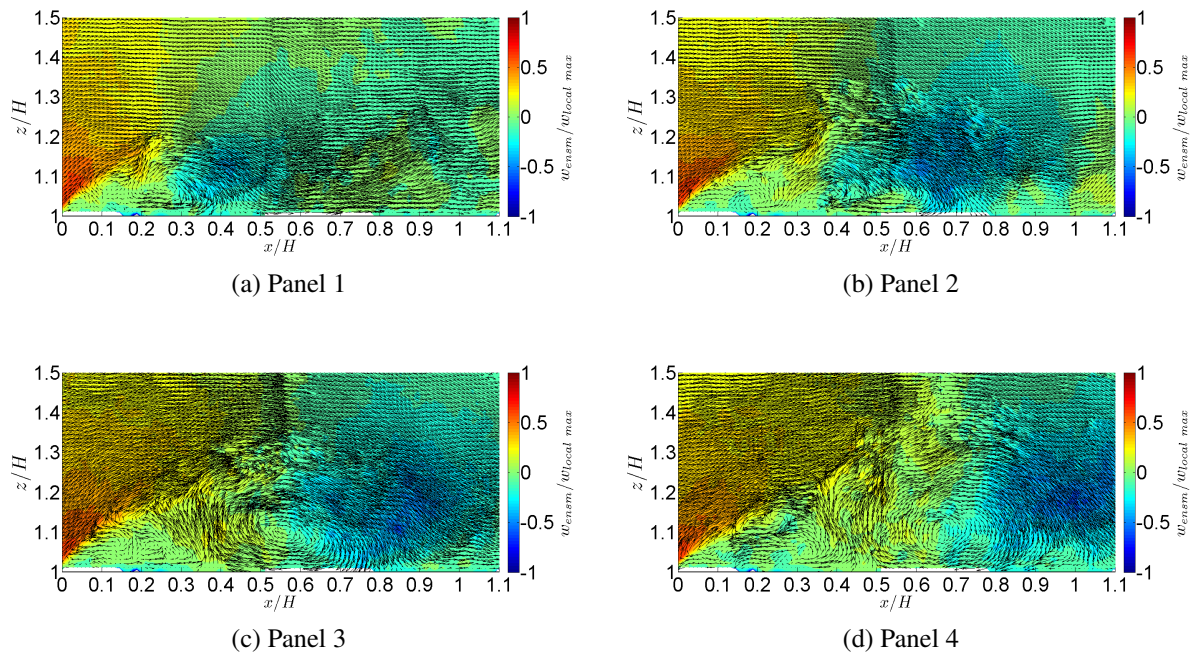
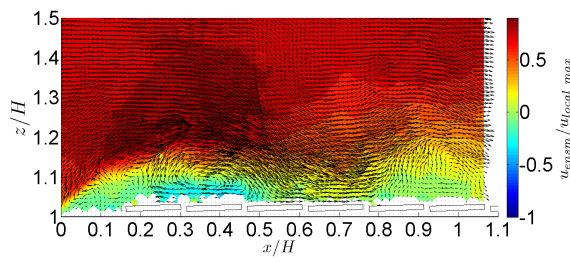
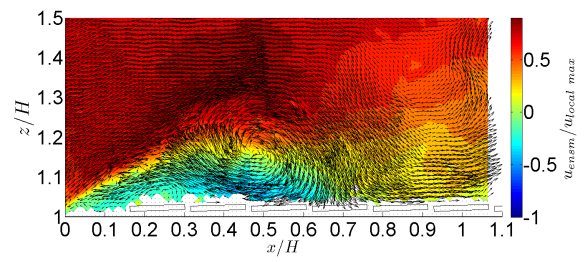


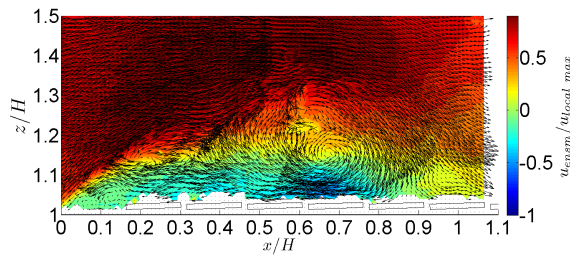
Figure C.2: Fraction of local maximum vertical velocity contour plots of peak ensemble averaged velocity fields for uplifts on imaginary panels on bare roof under a north/south wind.



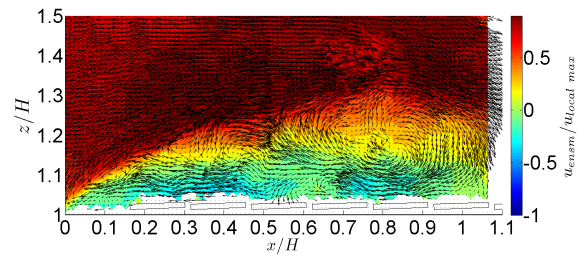
(a) Panel 1



(b) Panel 2

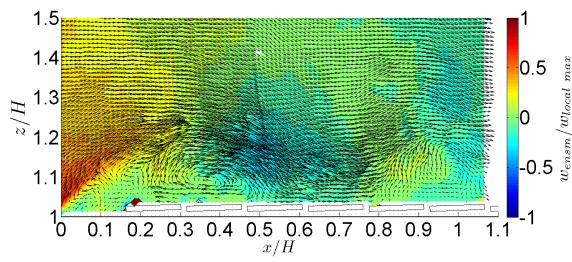


(c) Panel 3

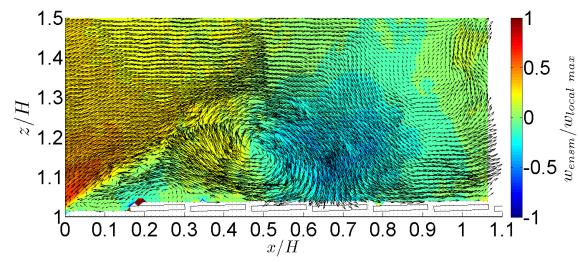


(d) Panel 4

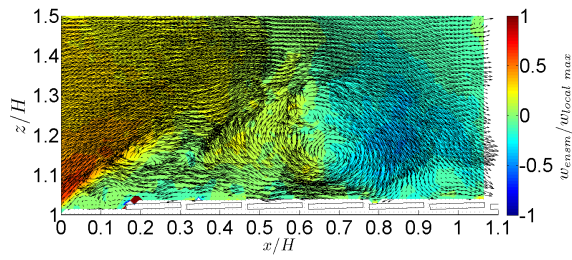
Figure C.3: Fraction of local maximum streamwise velocity contour plots of peak ensemble averaged velocity fields for uplifts on panels of 2° tilt angle array under a south wind.



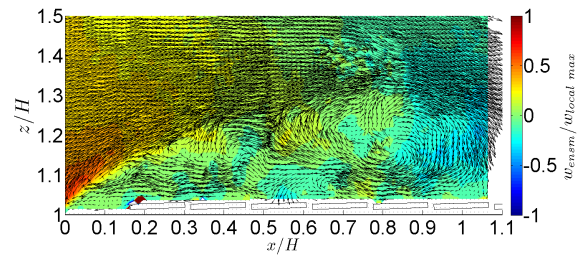
(a) Panel 1



(b) Panel 2

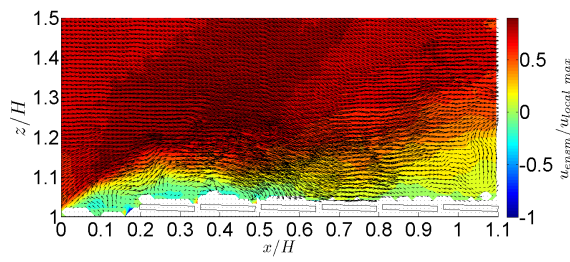


(c) Panel 3

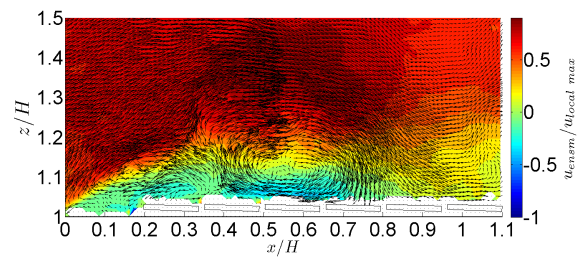


(d) Panel 4

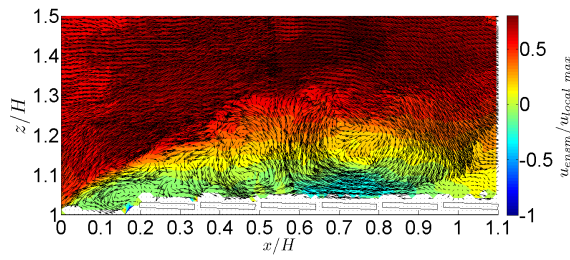
Figure C.4: Fraction of local maximum vertical velocity contour plots of peak ensemble averaged velocity fields for uplifts on panels of 2° tilt angle array under a south wind.



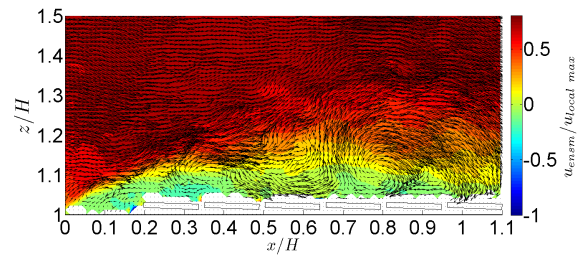
(a) Panel 1



(b) Panel 2

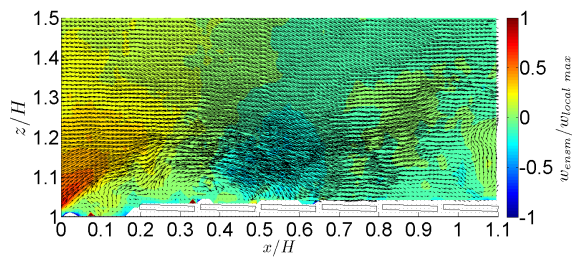


(c) Panel 3

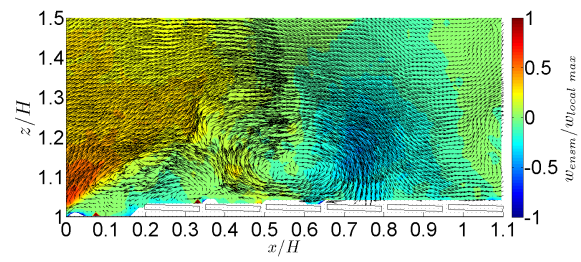


(d) Panel 4

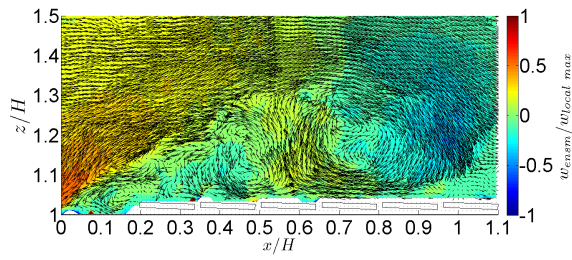
Figure C.5: Fraction of local maximum streamwise velocity contour plots of peak ensemble averaged velocity fields for uplifts on panels of 2° tilt angle array under a north wind.



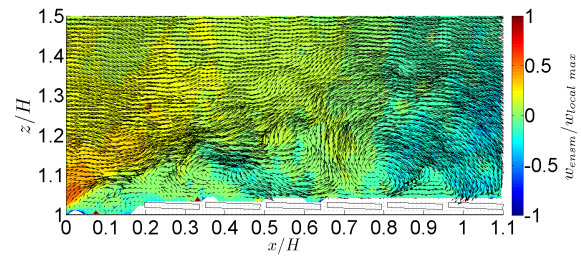
(a) Panel 1



(b) Panel 2

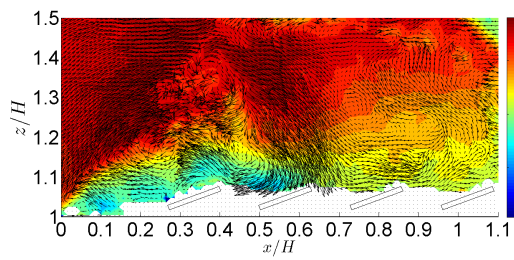


(c) Panel 3

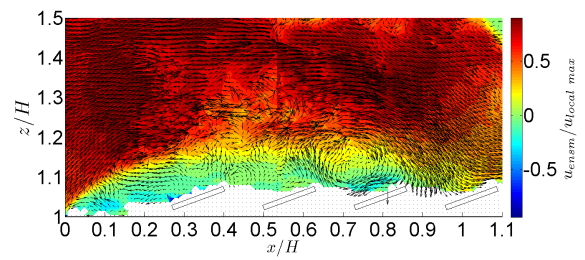


(d) Panel 4

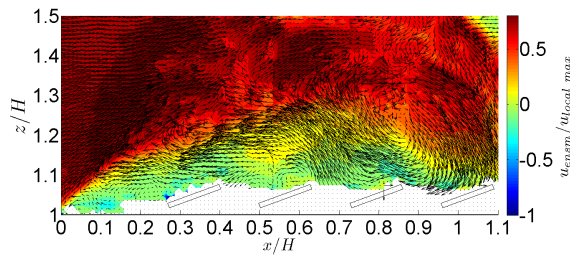
Figure C.6: Fraction of local maximum vertical velocity contour plots of peak ensemble averaged velocity fields for uplifts on panels of 2° tilt angle array under a north wind.



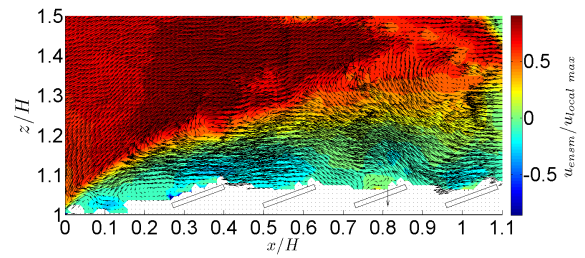
(a) Panel 1



(b) Panel 2

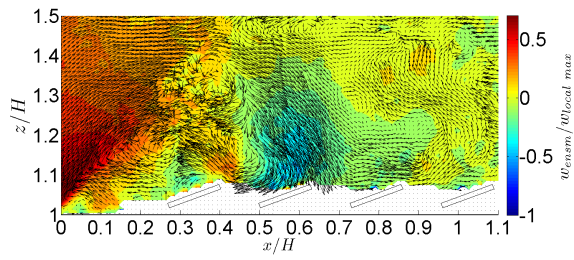


(c) Panel 3

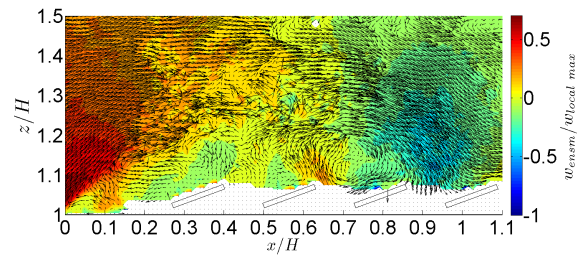


(d) Panel 4

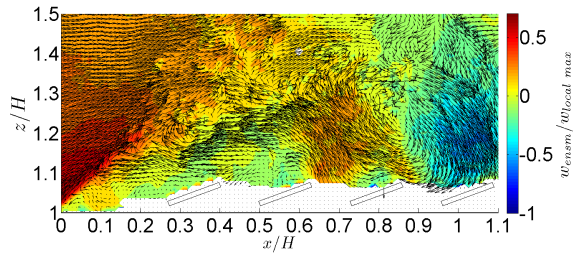
Figure C.7: Fraction of local maximum streamwise velocity contour plots of peak ensemble averaged velocity fields for uplifts on panels of 20° tilt angle array under a south wind.



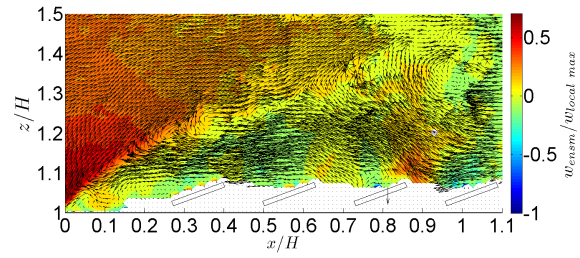
(a) Panel 1



(b) Panel 2

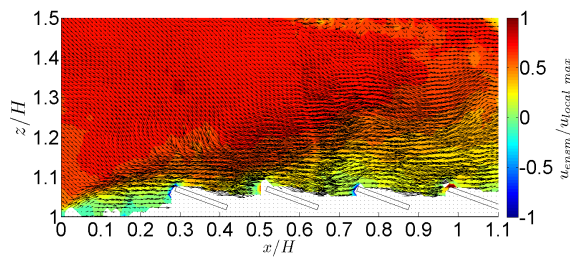


(c) Panel 3

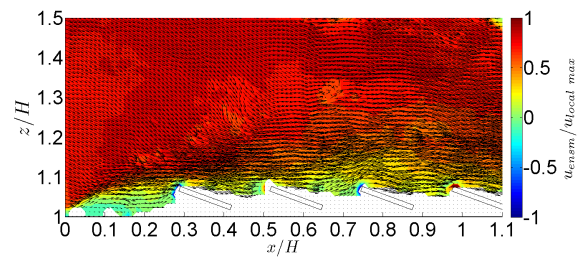


(d) Panel 4

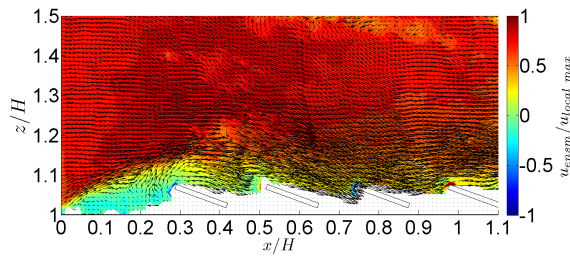
Figure C.8: Fraction of local maximum vertical velocity contour plots of peak ensemble averaged velocity fields for uplifts on panels of 20° tilt angle array under a south wind.



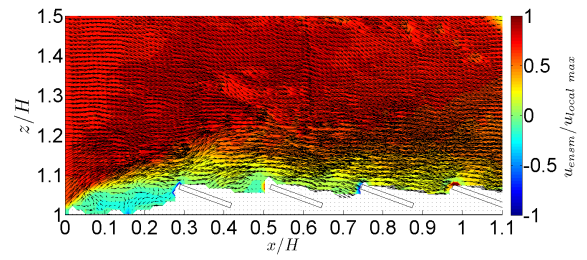
(a) Panel 1



(b) Panel 2

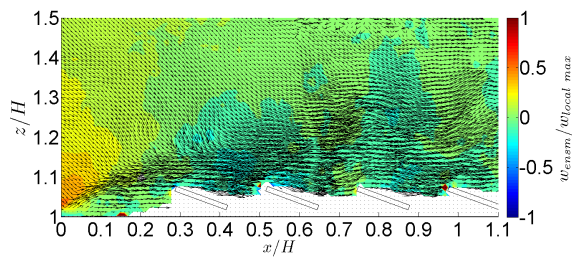


(c) Panel 3

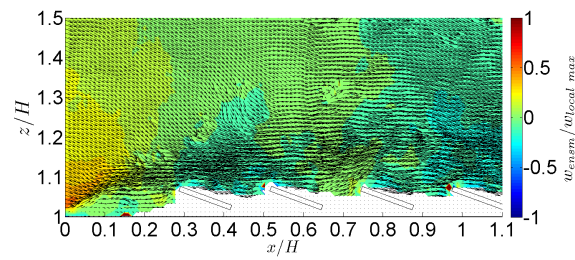


(d) Panel 4

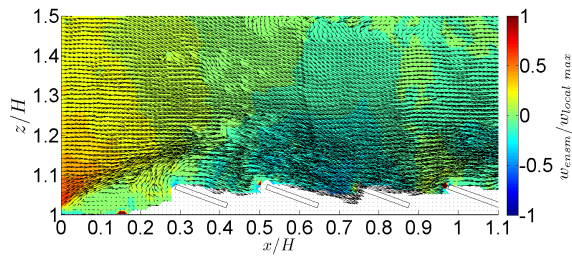
Figure C.9: Fraction of local maximum streamwise velocity contour plots of peak ensemble averaged velocity fields for uplifts on panels of 20° tilt angle array under a north wind.



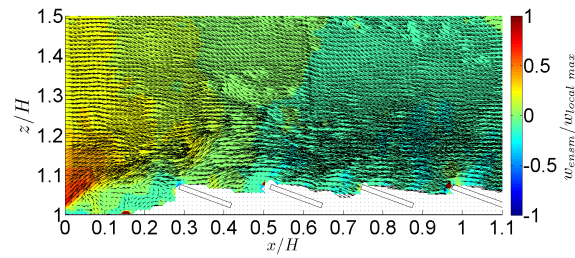
(a) Panel 1



(b) Panel 2



(c) Panel 3



(d) Panel 4

Figure C.10: Fraction of local maximum vertical velocity contour plots of peak ensemble averaged velocity fields for uplifts on panels of 20° tilt angle array under a north wind.

Curriculum Vitae

Name: Robert Nicolas Pratt

**Post-Secondary
Education and
Degrees:** Queen's University
Kingston, Ontario, Canada
2005 - 2009 B.Sc.E.

University of Western Ontario
London, Ontario, Canada
2011 - 2012 M.E.Sc.

**Related Work
Experience:** Sustainability Consultant
Jain Sustainability Consultants Inc.
2010-2011

Teaching Assistant
The University of Western Ontario
2011 - 2012

Publications:

Pratt, R.N. & Kopp, G.A. (2012) An initial study of the aerodynamics of photovoltaic panel arrays mounted on large flat-roofs, *7th International Colloquium on Bluff Body Aerodynamics and Applications*, Shanghai, China, Sept 2-6.